

High pressure Raman spectroscopic studies on anomalous thermal expansion materials

By

K. KAMALI

Enrolment no: CHEM02201004007

**Indira Gandhi Centre for Atomic Research,
Kalpakkam, Tamil Nadu, India, 603 102.**

*A thesis submitted to the
Board of studies in Chemical Sciences
In partial fulfilment of requirements
For the degree of*

DOCTOR OF PHILOSOPHY

of

HOMI BHABHA NATIONAL INSTITUTE



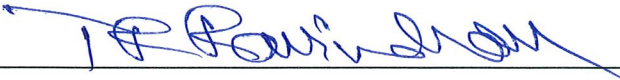
June 2015

Homi Bhabha National Institute

Recommendations of the Viva Voce Board

As members of the Viva Voce Board, we certify that we have read the dissertation prepared by **K. Kamali** entitled “**High pressure Raman spectroscopic studies on anomalous thermal expansion materials**” and recommend that it may be accepted as fulfilling the dissertation for the Degree of Doctor of Philosophy.


Chairman: Dr. B. V. R. Tata Date: 18/2/2016


Guide: Dr. T. R. Ravindran Date: 18.2.2016


Examiner: CHANDRABHAS NARAYANA Date: 18/02/2016


Member: Dr. H. N. Jena Date: 18/02/2016


Member: Dr. K. Sundararajan Date: 18/02/2016


Technology Adviser: V. Sivasubramanian Date: 18/02/2016

Final approval and acceptance of this dissertation is contingent upon the candidates' submission of the final copies of the dissertation to HBNI.

I hereby certify that I have read this dissertation prepared under my direction and recommend that it may be accepted as fulfilling the dissertation requirement.

Date: 18.2.2016

Place: Kalyakkam


Dr. T. R. Ravindran

(Guide)

Certificate

I hereby certify that I have read this dissertation prepared under my direction and recommend that it may be accepted as fulfilling the dissertation requirement.

Date:

Dr. T. R. Ravindran

(Guide)

Place:

Statement by Author

This dissertation has been submitted in the partial fulfilment of requirements for an advanced degree at Homi Bhabha National Institute (HBNI) and is deposited in the Library to be made available for borrowers under rules of the HBNI.

Brief quotations from this dissertation are allowable without special permission, provided that accurate acknowledgement of source is made. Requests for permission for extended quotation from or reproduction of this manuscript in whole or in part may be granted by the Competent Authority of HBNI when in his or her judgement the proposed use of the material is in the interests of the scholarship. In all other instances, however, must be obtained from the author.

K.Kamali

Declaration

I, hereby declare that the investigation presented in the thesis has been carried out by me.
The work is original and has not been submitted earlier as a whole or in part for a degree/diploma at this or any other Institution/University.

K. Kamali

Dedicated

To My beloved parents

G. Kesavan

&

K.Santhakumary

Acknowledgements

I sincerely thank and express my deepest gratitude to my supervisor, Dr. T. R. Ravindran, for his thoughtful guidance, encouragement and patience throughout the course of present work. I would not have been able to complete my work without his motivation, inspiring advice and constant support.

I would like to express my gratitude to Dr. Vasudeva Rao, Director, IGCAR for permitting me to pursue Ph. D at IGCAR and highly thankful to Dr. C. S. Sundar, Dr. M. P. Janawadkar and Dr. G. Amarendra, past and present Group Director, MSG for providing the conducive atmosphere for my smooth research. I thank Dr. Saibaba for the wonderful hospitality during my stay at JRF Enclave.

I am also very grateful to all the professors of my doctoral committee; Dr. B. V. R. Tata, Dr. H. N. Jena, Dr. K. Sundararajan and Dr. V. Sivasubramanian; for sharing their valuable time and for providing me with helpful feedback and evaluating my work at each stage. I extend my sincere thanks to my past doctoral chairman Dr. A. K. Arora and member Dr. K. V. G. Kutty for his provoking scientific suggestions and valuable comments.

I would like to thank Dr. R. Nithya and Dr. V. Sivasubramanian, who had helped me in synthesis of samples and their useful discussions. I am thankful to Dr. V. Srihari, Dr. V. Sriharan, Dr. R. M. Sarguna and Dr. S. Kalavathi for their timely help in X-ray diffraction measurements. I thank Dr. T. N. Sairam, Dr. R. Ramanathan and Dr. K. Sivasubramanian for Infrared measurements. I am extremely thankful to Dr. N. Subramanian, Dr. N. V. ChandraShekar and Dr. Y. A. Sorb who have guided me in

analysing high pressure XRD measurements. High pressure synchrotron x-ray diffraction work discussed in this thesis was carried out at the Raja Ramana Centre for Advanced Technology (RRCAT), Indore. I am thankful to Dr. K. K. Pandey and Dr. S. M. Sharma for sharing their invaluable expertise with us.

I am highly grateful to Dr. Ravi Chinnappan who had immensely helped in learning DFT calculations and much useful discussion during entire tenure of Ph. D.

I would like to thank all my teachers, who had taught me at various stages of educational career. It is my great pleasure to thank Dr. K. S. Vishwanathan, Dr. Lakshmi Narasiman and Dr. M. C. Valsakamar and more for their teaching and encouragement during the course work period.

I always cherish the time I spent working with my lab mates Dr. Karuna Kara. Mishra, Mrs. Soumee Chakraborty, Mr. Deepak Kumar Gupta, Dr. R. K. Joshi, Mr. D. Karthickeyan and Ms. Shradhanjali Sahoo.

It is my pleasure to thank my friends and batchmates L. K. Preethi, B. V. Ramana, A. V. Meera, K. R. Rashmi, A. Amutha, P. Yashoda, T. R. Devidas, Benadict Rakesh, Avinash Patsha, N. Salke and V. Mahendran for support and encouragement. The affection of senior and love of junior scholars in Enclave are highly acknowledged. I would like to express sincere thanks to my senior roommate Ms. Ruth Nithila and dear neighbour Dr. Rajini P Antony.

Above all, I would like to express my deepest gratitude to my beloved parents, brothers, late grandmother and my whole family, who has given me the freedom to pursue my career and love, immense patience and support to make it possible.

List of Publications/Preprints

Publications in Journals/Preprints

1. Anharmonic phonons of $\text{NaZr}_2(\text{PO}_4)_3$ studied by Raman spectroscopy, first principles calculations and x-ray diffraction

K. Kamali, T. R. Ravindran, C. Ravi, Y. Sorb, N. Subramanian and A. K. Arora,

Phys. Rev. B, **86** (2012) 144301.

2. Pressure induced phase transformations in $\text{NaZr}_2(\text{PO}_4)_3$ studied by X-Ray diffraction and Raman spectroscopy

K. Kamali, T. R. Ravindran and N. V. Chandra Shekar, K. K. Pandey and S. M. Sharma

J. Solid State Chem. **221** (2015) 285.

3. High pressure Raman spectroscopic study of TaO_2F

K. Kamali, T. R. Ravindran and T. N. Sairam

Vibrational Spectroscopy, **71** (2014) 12.

4. Linear compressibility and thermal expansion of $\text{KMn}[\text{Ag}(\text{CN})_2]_3$ studied by Raman spectroscopy and first-principles calculations

K. Kamali, T. R. Ravindran, C. Ravi, R. M. Sarguna, T. N. Sairam and G. Kaur,

J. Phys. Chem. C, 117 (2013) 25704.

5. Comparative Raman spectroscopic study of phase stability and anharmonic effects in $\text{AZr}_2(\text{PO}_4)_3$ (A= K, Rb and Cs)

K. Kamali, T. R. Ravindran and C. Ravi

Spectrochim. Acta, Part A **155**, (2016) 38.

Publication not included in thesis

6. Temperature and Pressure Dependent Phase Transitions of β' -LiZr₂(PO₄)₃ Studied by Raman Spectroscopy

K. Kamali and T. R. Ravindran (Under Review)

7. Raman spectroscopic studies of CuFeO₂ at high pressures

Nilesh. P. Salke, **K. Kamali**, T. R. Ravindran, G. Balakrishnan and Rekha Rao

Vibrational Spectroscopy, **81** (2015) 112.

Published conference Proceedings

1. Synthesis and Raman spectroscopic studies of NaZr₂(PO₄)₃

K. Kamali, T. R. Ravindran, V. Sridharan and R. Nithya, AIP conf. proc. 1447 (2012) 823.

2. Pressure induced local disorder to order phase transition in TaO₂F

K. Kamali and T. R. Ravindran, AIP conf. proc. 1591 (2014) 38.

Conference papers unpublished (Abstract only)

4. *High Pressure Raman spectroscopic studies of Ca_{0.5}Sr_{0.5}Zr₄(PO₄)₆*

K.Kamali, T. R. Ravindran, V. Sridharan and R. Nithya

International Conference on Raman Spectroscopy (ICORS), Bangalore (2012).

5. Lattice dynamics of negative compressible KMn[Ag(CN)₂]₃

K.Kamali, C. Ravi and T. R. Ravindran

Asia Sweden Meeting on understanding Functional materials from Lattice Dynamics Guwahati (2014).

Contents

Synopsis	i
List of Figures	iv
List of Tables	xi
1 Introduction	1
1.1 Thermal expansion	1
1.1.1 Low thermal expansion	5
1.1.2 Colossal anisotropic thermal expansion	8
1.2 Materials of interest	11
1.2.1 NZP family of compounds	11
1.2.2 TaO ₂ F	14
1.2.3 KMn[Ag ₃ (CN) ₆]	16
1.3 High Pressure Behavior of NTE Materials and Other Framework Material	17
1.4 References	20
2 Experimental and computational details	25
2.1 Synthesis	25
2.1.1 NZP compounds by sol-gel method	26
2.1.2 TaO ₂ F by slow evaporation method	27
2.1.3 KMn[Ag ₃ (CN) ₆] by slow diffusion method	27
2.2 Experimental techniques	28
2.2.1 Raman scattering	28
2.2.2 High pressure technique	31
2.2.3 X-ray diffraction	37
2.3 Computational details	38

2.4	References	44
3	Low thermal materials: Anharmonic phonons of sodium zirconium phosphate studied by high pressure XRD, Raman and first principle calculations	46
3.1	Introduction	46
3.2	Experimental and computational details	47
3.3	Results and discussion	50
3.3.1	Raman spectroscopic and computational studies	52
3.3.2	High pressure XRD	65
3.4	Summary and conclusion	72
3.5	References	74
4	Low thermal materials: Comparative Raman spectroscopic study of phase stability and anharmonic effects in $AZr_2(PO_4)_3$ (A= K, Rb and Cs)	77
4.1	Introduction	77
4.2	Experimental and computational details	79
4.3	Results and discussion	80
4.3.1	Raman spectroscopic studies	81
4.3.2	Computation of phonon dispersion curves and bulk moduli	93
4.3.3	Temperature dependent Raman studies	96
4.4	Summary and conclusion	102
4.5	References	102
5	Zero thermal expansion material: High pressure Raman spectroscopic studies of phase transformations in TaO_2F	105
5.1	Introduction	105
5.2	Experimental details	107

SYNOPSIS

Thermal expansion is an important property of solids for many industrial and practical applications. Most materials expand on heating, but some materials exhibit opposite behaviour, i.e., they contract upon heating, which is termed as negative thermal expansion (NTE). Thermal expansion (or contraction) can be isotropic or anisotropic. Isotropic materials expand equally in all directions in the unit cell (e.g. cubic solids). Whereas anisotropic materials have different magnitudes of thermal expansion along the different unit cell axes which leads to net low or nearly zero thermal expansion. The magnitude of anisotropic thermal expansion varies with structural geometry and substitution of different size of cations within the same family. The magnitude of thermal expansion in a material is quantified by its coefficient of thermal expansion (TEC). Anomalous thermal expansion materials include those with net low thermal expansion, nearly zero thermal expansion and colossal anisotropic thermal expansion.

Thermal expansion coefficients (TEC) are measured experimentally by Dilatometry and high temperature X-ray diffraction. The former measures the average TEC for bulk solids (macroscopic) whereas the latter gives intrinsic TEC along different directions in the crystallographic unit cell.

In the quasi harmonic approximation, the coefficient of thermal expansion of a material can be expressed as,

$$\alpha = \frac{\gamma_{av} C_V}{3BV}$$

where γ_{av} is the average Gruneisen parameter, C_v is specific heat at constant volume, V is the molar volume and B is the bulk modulus of the material.

This thesis is a compilation of results of studies on a number of anomalous thermal expansion materials primarily using Raman spectroscopy as a function of pressure at ambient temperature, and as a function of temperature at ambient pressure. In some cases first principles computational and high pressure x-ray diffraction studies were carried out. Different compounds exhibiting a range of anomalous thermal expansion coefficient are studied: (a) low thermal expansion: $AZr_2(PO_4)_3$, $A=Na, K, Rb, Cs$. (b) zero thermal expansion: TaO_2F and (c) colossal thermal expansion: $KMnAg_3(CN)_6$.

This thesis also reports Raman spectroscopic investigations of phase transitions for all above compounds. Pressure is used as a primary thermodynamic parameter to take the system across phase transition(s). In the prototypic NZP, pressure induced phase transition is analyzed using high pressure X-ray diffraction. Wherever possible, supporting first-principles calculations are carried out.

This thesis is organized into seven chapters and the contents of each chapter are as follows:

In a nutshell: **Chapter 1** gives an introduction to the subject and **chapter 2** presents the details of synthesis, characterization and experimental techniques. **Chapter 3, 4, 5 and 6** discuss the results on prototypic NZP, alkali cation substituted NZP, TaO_2F and $KMn[Ag(CN)_2]_3$ respectively. **Chapter 7** summarizes the work reported in this thesis and the conclusions drawn from the present studies. In addition, directions for possible future studies are indicated.

More elaborately: **Chapter 1** gives a brief introduction to anomalous thermal expansion materials, their properties and applications. Various compounds with different structural arrangement exhibiting anomalous thermal expansion are discussed in detail. **Chapter 2**

contains the details of synthesis procedures for polycrystalline materials and single crystals; experimental techniques, i.e. Raman spectroscopy and X-ray diffraction, and first-principles calculations used for investigation are described. **Chapter 3** presents results of high pressure investigation on prototypic sodium zirconium phosphate for phase stability and contribution of various phonon modes to overall thermal expansion. In addition, first-principles studies are presented for calculation of thermal expansion coefficient. In **chapter 4**, high pressure Raman studies on alkali substituted NZP family are presented; the different phonon modes are analyzed to explain tunable low thermal expansion property of these materials. In **chapter 5** high pressure Raman studies on TaO₂F are discussed to clear the ambiguity in phase transition pressures; thermal expansion coefficient of TaO₂F is calculated using the mode Gruneisen parameters. In **chapter 6**, negative thermal expansion, negative linear compressibility and phase transformations in KMn[Ag(CN)₂]₃ are discussed using results obtained from Raman spectroscopy and first principles calculations. In **chapter 7**, a summary of the results obtained, and conclusions arrived at are presented along with a brief discussion on possible directions on future studies.

A brief discussion of the work on the various systems is presented after the section on Experimental and computational details. The organization of the thesis, significant results from the present studies, and the list of publications arising out of the work are presented towards the end of this Thesis.

List of Figures

Figure No.	Figure Caption	Page No.
1.1	Potential energy diagram for an anharmonic oscillator where mean distance between atoms R_1 and R_2 increase with rise in temperature T_1 and T_2 .	2
1.2	Representation of the transverse vibrational motion of an oxygen atom in a M-O-M linkage resulting in negative thermal expansion. A cooperative rotation of the polyhedra causes a decrease in the average metal-metal distances	6
1.3	A representation of local vibrational modes responsible for NTE behavior in structures containing diatomic linkages. The filled circles represent heavy (usually metal) atoms, and the open circles represent light bridging atoms, of CN species. With increase in temperature, population of these vibrational modes leads to a decrease in the overall metal-metal distance.(Goodwin <i>et al</i>)	6
1.4	Compression mechanism in $Ag_3[Co(CN)_6]$, exaggerated for illustrative purposes: In order for the framework to reduce its volume (either in response to a decrease in temperature or an increase in pressure), it must expand along the trigonal axis (c). (Goodwin <i>et al</i>)	10
1.5	A view of the $NaZr_2(PO_4)_3$ structure parallel to the <i>c</i> -axis. Corner-shared ZrO_6 -octahedra and PO_4 -tetrahedra with Na(1) and Na(2) interstitial sites are clearly seen.	13
1.6	Schematic representation of crystal structure of TaO_2F adopting cubic ReO_3 structure with corner sharing $Ta(O/F)_6$ octahedra.	14
1.7	Single-Ta-O-Ta-O-Ta-F-Ta-chain from the TaO_2F supercell	15

model. (Morelock *et al*)

- 1.8** (a) Crystal structure of $\text{KMn}[\text{Ag}(\text{CN})_2]_3$: $[\text{MnN}_6]$ octahedra are connected via almost linear NC-Ag-CN units, with K^+ ions positioned above and below alternating Ag_3 Kagome triangles. (b) Re-arrangement of the Ag Kagome sublattice couples to framework shear in $\text{Ag}_3[\text{Co}(\text{CN})_6]$ is shown in arrows which is viewed along c-axis. (c) These displacements would give unphysical $\text{Ag}^+\dots\text{K}^+$ distances in $\text{KMn}[\text{Ag}(\text{CN})_2]_3$; the soft mode responsible for phase transition is stiffened.(Cairns *et al*) 17
- 2.1** Steps of single crystal growth using layering technique (i) Aqueous $\text{Mn}(\text{NO}_3)_2$ solution to be crystallized. (ii) Drop by drop addition of precipitant (a+b) (iv) Left overnight without disturbance (v) Single crystals form at the interface. 28
- 2.2** Schematic representation of (a) creation (Stokes) and (b) annihilation (anti-Stokes) of phonon (q, ω_p) 29
- 2.3** Schematic diagram of Symmetric diamond anvil cell. 33
- 2.4** Cr^{3+} luminescence in ruby at ambient pressure (black) and at 11 GPa (red). 34
- 2.5** Schematic diagram of Renishaw micro-Raman spectrometer 35
- 3.1** Rietveld refinement of ambient pressure X-ray diffraction data for NZP. Red points are experimental data, continuous line represents the fitted data and the bottom curve is the difference plot. 51
- 3.2** Raman spectra of NZP for selected pressures up to 30 GPa which clearly indicates phase transitions around 5 and 5.8 GPa. On decompression, it regains original phase showing reversible transition. 53

- 3.3** Phonon dispersion curves from simulations using VASP code on a 36 atom rhombohedral primitive unit cell of $\text{NaZr}_2(\text{PO}_4)_3$. The E_g zone centre phonon frequencies exhibit good matching with experimental Raman values. 55
- 3.4** Atomic displacements of (a) the 113 cm^{-1} mode showing a combination of the PO_4 librations and Zr translations; (b) the 127 cm^{-1} mode exhibiting coupled rotation of PO_4 tetrahedra and ZrO_6 octahedra; (c) the asymmetric stretch mode of PO_4 at 927 cm^{-1} corresponding to the most intense Raman band at 1026 cm^{-1} and (d) symmetric stretch mode of PO_4 at 991 cm^{-1} corresponding to the Raman band at 1061 cm^{-1} . 57
- 3.5** ω vs. P of NZP. Changes in the spectral frequencies are clearly seen at 5.5 GPa, signifying a phase transformation that is confirmed from XRD measurements. 60
- 3.6** Raman spectra of NZP at different temperatures. The compound is stable in the entire temperature range from 80 K to 860 K. 62
- 3.7** ω vs. T of NZP showing monotonic decrease in the mode frequencies of all modes except the two lowest at 72 and 110 cm^{-1} that exhibit opposite behaviour. 63
- 3.8** XRD patterns at different pressures. * denotes gasket peak, Au – pressure marker. Disappearance of several reflections is noticeable above 6 GPa. Patterns recorded in the pressure reducing cycle are indicated by the prefix ‘R’. 66
- 3.9** X-ray diffraction patterns of NZP at different pressures. ‘g’ indicates peaks arising due to tungsten gasket. Note that the upward arrows indicate the reflections arising in the new phases around 5 and 6.7 GPa. 67

- 3.10** Variation of lattice parameters with pressure. Dotted lines partition different phases such as $R-3c$, $R3$ with a and c lattice parameter and orthorhombic structure with a , b and c lattice parameter. 68
- 3.11** Pressure dependence of volume per NZP formula unit (Z). The solid lines show the fitting with the third order Birch Murnaghan equation of state for the three different phases. 69
- 3.12** X-ray diffraction peaks are indexed with $R-3c$, $R3$ and orthorhombic phases at 0.4, 5.4, 8.2 GPa. Inset shows the Rietveld fitted pattern at 0.4 GPa 70
- 3.13** Intensity of the peak corresponding to the (009) plane (a) and the (3015) plane (b) on compression suggests a transition to $R3$ phase. To take into account differences in exposure time between diffraction images, the intensity was scaled to that of the strongest peak in the diffraction pattern. The resultant values were normalized to that of 8.2 GPa measurements. 70
- 4.1** Raman spectra of (a) $\text{KZr}_2(\text{PO}_4)_3$ (b) $\text{RbZr}_2(\text{PO}_4)_3$ and (c) $\text{CsZr}_2(\text{PO}_4)_3$ at different temperatures. Low frequency region covers lattice modes and bending modes of PO_4 ion from 70-450 cm^{-1} and high frequency region corresponds to stretching modes of phosphate ion. 81
- 4.2** Mode frequencies of various Raman modes as a function of temperature for (a) $\text{KZr}_2(\text{PO}_4)_3$ (b) $\text{RbZr}_2(\text{PO}_4)_3$ and $\text{CsZr}_2(\text{PO}_4)_3$. Modes at 74, 124, 403, 419 and 435 cm^{-1} for KZP and modes at 85, 126, 159, 401, 421 and 441 cm^{-1} for RbZP and 105, 134, 168, 423 and 449 cm^{-1} in CsZP increase with increase in temperature which marked as red lines. 83
- 4.3** Raman spectra of (a) $\text{KZr}_2(\text{PO}_4)_3$ (b) $\text{RbZr}_2(\text{PO}_4)_3$ and (c) $\text{CsZr}_2(\text{PO}_4)_3$ at different pressures. KZP and RbZP show phase 89

transition around 3.5 and 2.2 GPa and CsZP shows two transitions around 3.5 and 8.4 GPa. Pressure induced amorphisation for KZP, RbZP and CsZP occurs at higher pressures.

- 4.4** Variation of Raman mode frequencies as a function of pressure for (a) $\text{KZr}_2(\text{PO}_4)_3$ (b) $\text{RbZr}_2(\text{PO}_4)_3$ and (c) $\text{CsZr}_2(\text{PO}_4)_3$. Modes at 74 and 124 cm^{-1} for KZP and modes at 85, 126 155 and 170 cm^{-1} for RbZP and 105, 134 and 168 cm^{-1} decrease with increase in pressure which marked as red lines. These modes are considered as soft modes. 91
- 4.5** Atomic displacements of (a) the 72 cm^{-1} mode of NZP and 73 cm^{-1} of KZP showing Zr translation and PO_4 librations (b) the 134 cm^{-1} mode of CsZP and 170 cm^{-1} of RbZP showing coupled rotation of PO_4 tetrahedra and ZrO_6 octahedra (c) the 159 cm^{-1} mode of RbZP exhibit maximum amplitude of displacement in coupled rotation of PO_4 tetrahedra and ZrO_6 octahedra than 155 cm^{-1} in KZP (c) the 76 cm^{-1} IR mode of NZP with Na translation shows large magnitude of displacement than 67 cm^{-1} mode of CsZP with Cs translation. 95
- 4.6** Temperature variation of (a) Raman shift of modes corresponding to 72 (NZP), 73 (KZP), 85 (RbZP) and 105 cm^{-1} (CsZP) shows abnormal hardening behaviour 100
- 5.1** Raman spectrum of TaO_2F at ambient conditions with peaks fitted using Peakfit software. 108
- 5.2** Raman spectra at various pressures both in increasing and decreasing pressure cycles. Dotted line indicates the softening of 200 cm^{-1} band with increasing pressure. 110
- 5.3** Frequency vs Pressure plot showing clear phase transition at 0.8 GPa. 111

5.4	Raman spectra of TaO ₂ F in the temperature range 80 K to 873 K. Appearance of the mode at 106 cm ⁻¹ indicates onset of decomposition to Ta ₂ O ₅ .	114
5.5	Temperature dependence of mode frequencies from 80 K to 873 K.	115
5.6	IR absorption spectrum of TaO ₂ F at ambient conditions covering the range from 100-1100 cm ⁻¹ .	116
6.1	Powder XRD pattern of KMn[Ag(CN) ₂] ₃ showing single phase.	124
6.2	A few hexagonal shaped crystals (a); under cross-polarized condition (b).	125
6.3	Polarized Raman spectra of KMn[Ag(CN) ₂] ₃ in Z(XX)Z' (VV) and Z(XY)Z' (VH) scattering geometries at 80 K. Both A ₁ and E modes appear in VV geometry. The labeled Raman modes that disappeared in the VH geometry are assigned as A ₁ .	129
6.4	IR spectrum of KMn[Ag(CN) ₂] ₃ at ambient conditions.	131
6.5	Raman spectra of KMn[Ag(CN) ₂] ₃ at different temperatures. Distinct change in the spectrum due to the decomposition of the compound is clearly seen at 503 K.	132
6.6	Temperature variation of phonon frequencies of KMn[Ag(CN) ₂] ₃ showing monotonic decrease of all mode frequencies with increase in temperature.	133
6.7	Raman spectra of KMn[Ag(CN) ₂] ₃ at different pressures under hydrostatic conditions. Dramatic change at 2.8 GPa and amorphization around 13.5 GPa are evident.	134
6.8	Pressure variation of phonon frequencies of KMn[Ag(CN) ₂] ₃ under hydrostatic conditions. All modes, except the CN stretch band,	135

disappear above 13 GPa.

- 6.9** Linear compressibilities of $\text{KMn}[\text{Ag}(\text{CN})_2]_3$ calculated by fitting lattice parameters and their corresponding pressures using PASCAL. Pressures are obtained from equation of state calculation. 139
- 6.10** Computed pressure dependent elastic constants of $\text{KMn}[\text{Ag}(\text{CN})_2]_3$. C_{44} shows negative pressure derivatives indicating pressure induced structural instability. 144
- 6.11** Pressure variation of mean partial phonon frequencies of the various atoms in $\text{KMn}[\text{Ag}(\text{CN})_2]_3$ and $\text{Ag}_3[\text{Co}(\text{CN})_6]$. K, Mn, Ag, C and N partial frequencies from $\text{KMn}[\text{Ag}(\text{CN})_2]_3$ are shown by \circ , Δ , \diamond , \triangleleft , \triangleright respectively. Partial frequencies of Co, Ag, C and N from $\text{Ag}_3[\text{Co}(\text{CN})_6]$ are shown by symbols ∇ , \square , \times , $+$ respectively. Ag frequencies shows lower slope relative to other atoms. 146
- 6.12** Computed atomic displacements of the low frequency optic modes, (a) the A_2 mode at 38cm^{-1} , (b) the E mode at 49cm^{-1} . 147

List of Tables

Table No.	Table Captions	Page No.
3.1	Structural parameters of NZP at ambient conditions showing fractional coordinates and the isotropic atomic displacement from Reitveld refinement of powder diffraction data. The lattice parameters are $a=b=8.799(1)\text{\AA}$ and $c=22.7408(6)\text{\AA}$ (hexagonal notation). The R factor $R_p=16.5\%$ and the reduced $\chi^2=3.42$.	51
3.2	Frequencies and mode Gruneisen parameters (γ_i) of Raman modes of NZP from experiments and simulations. Mode assignments were obtained from the VASP computed eigen vectors using the Phonopy program.	54
3.3	Total anharmonicities, quasiharmonic and true-anharmonic contributions of different phonons in NZP. The numbers in the parentheses are standard errors in the least significant digit.	64
4.1	Total anharmonicities, quasiharmonic and true-anharmonic contributions of different phonons in NZP using computed bulk modulus. The numbers in the parentheses are standard errors in the least significant digit.	85
4.2	Total anharmonicities, quasiharmonic and true-anharmonic contributions of different phonons in KZP. The numbers in the parentheses are standard errors in the least significant digit.	86
4.3	Total anharmonicities, quasiharmonic and true-anharmonic contributions of different phonons in RbZP. The numbers in the parentheses are standard errors in the least significant digit.	87
4.4	Total anharmonicities, quasiharmonic and true-anharmonic contributions of different phonons in CsZP. The numbers in the	88

parentheses are standard errors in the least significant digit.

- 4.5** Coefficients of cubic and quartic anharmonicities obtained from the analysis of the line width and phonon frequency shift with variation of temperature using eq.4.6. Γ_o and ω_o represent line width and phonon frequency at 0K (extrapolated from 80 K in Figure 4.6), and their corresponding fitting parameters using eq. (4.6). 101
- 5.1** Gruneisen parameters for both disordered cubic phase and rhombohedral phase are obtained using the expression $:(B/\omega_i)(d\omega/dP)$, $B=36$ GPa for cubic phase. 112
- 5.2** Total anharmonicities, quasiharmonic and true anharmonic contributions of different phonons in TaO₂F. The numbers in the parentheses are standard errors to the least significant digit. $\alpha=+1$ ppm K⁻¹ 116
- 5.3** Comparison of Raman and IR mode frequencies in TaO₂F. Raman modes are active due to loss of center of symmetry. IR mode at 990 cm⁻¹ is found to be overtone of 495 cm⁻¹. 118
- 6.1** Comparison of Raman and IR frequencies of KMn[Ag(CN)₂]₃ and their mode assignments obtained using Polarised Raman measurements with the computed zone center phonon frequencies and mode assignments. Mode Gruneisen parameters (γ_i) are also listed. 130
- 6.2** Total anharmonicities, quasiharmonic (implicit) and true anharmonic (explicit) contribution of different phonons of KMn[Ag(CN)₂]₃ The numbers in the parentheses are standard errors in the least significant digit. 136
- 6.3** Comparison of computed lattice parameters, unit cell volume and bulk modulus of KMn[Ag(CN)₂]₃ with experimental values. Bulk 137

modulus (B) and its pressure derivative (B') were obtained by fitting volume-energy data to the universal equation of state

- 6.4** DFT computed elastic constants, bulk modulus and mean linear compressibilities of $\text{KMn}[\text{Ag}(\text{CN})_2]_3$. Linear compressibilities are obtained from zero pressure elastic constants. 141

Chapter 1

Introduction

1.1. Thermal expansion: a microscopic picture

Thermal expansion of solids is a physical property that depends on the nature of the interatomic potentials. Thermal expansion of a diatomic molecule can be explained based on the asymmetric shape of a typical interatomic potential well, as shown in Figure 1.1. As two atoms are brought together, columbic attractive forces dominate the overall potential energy of the system until they experience short-range repulsions followed by increase in potential energy. The attractive interactions lead to a decrease in the potential energy as the two atoms come close together and bond formation begins. The repulsive interaction of the electrons is reflected on the left side of the curve (Figure 1.1) from the minimum and increases with decreasing interatomic distance. Due to the asymmetry of the potential well, average bond distance increases with increase in energy or temperature. If the interatomic potential was perfectly harmonic, the average distance would be the same for all vibrational energies and no expansion would be observed. A stronger bond results in a more symmetric potential well which means the bond expansion is smaller on thermal excitation.¹ Open framework compounds with strongly bonded polyhedra expand little or contract through coupled rotation of corner linked polyhedral atoms.

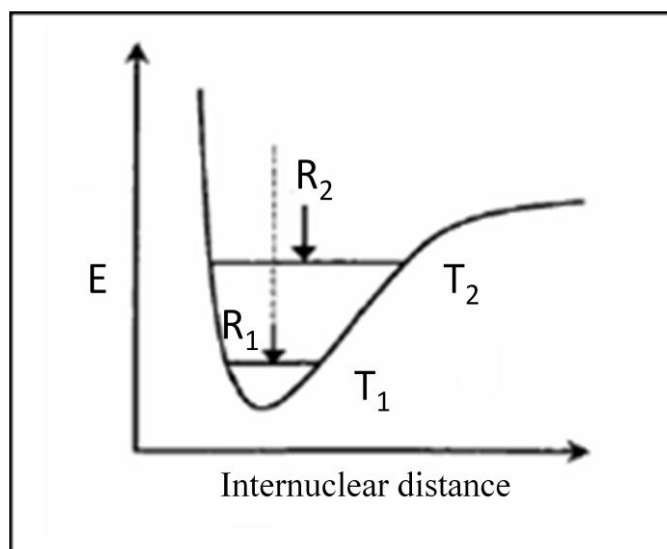


Figure 1.1 Potential energy diagram for an anharmonic oscillator where mean distance R_1 and R_2 between atoms increases with rise in temperature T_1 and T_2 .

The magnitude of thermal expansion in a material is quantified by its coefficient of thermal expansion (CTE); the volumetric coefficient of thermal expansion α is defined as,

$$\alpha = \left(\frac{\partial \ln V}{\partial T} \right)_P = \left(\frac{1}{V} \frac{\partial V}{\partial T} \right)_P \quad (1.1)$$

Where V is volume, T is temperature and P is the pressure. The average linear thermal expansion coefficient (α_{av}) is defined as,

$$\alpha_{av} = \frac{(l_2 - l_1)}{l_1(T_2 - T_1)} \quad (1.2)$$

where l_1 and l_2 are lattice parameters of the unit cell or linear dimensions of the material at temperatures T_1 and T_2 respectively. The former can be determined from x-ray diffraction techniques, and the latter using dilatometry. A cubic material, where lattice constants $a = b = c$, will have a unit cell that contracts or expands isotropically. For anisotropic solids, different values of linear thermal expansion coefficients are observed along different directions depending on crystal structure. On a macroscopic

scale, normally all dimensions of a solid should increase with rise in temperature and on a microscopic scale we expect the energy of vibrational modes to increase with temperature giving rise to an increase in amplitude of vibrations. The mode Gruneisen parameter (γ_i), relates the fractional change in vibrational frequency to the fractional change in volume.²

$$\gamma_i(q) = -\left(\frac{\partial \ln \omega_i(q)}{\partial \ln V}\right) \quad (1.3)$$

where $\omega_i(q)$ is the frequency of the i^{th} mode vibration of wavevector q in first Brillouin zone and V is the volume. $\omega_i(q)$ is evaluated either using lattice dynamical calculation or high pressure neutron inelastic scattering measurements. The change in phonon mode frequencies of a solid as a function of temperature at constant pressure occurs due to two effects: 1. A true anharmonic contribution due to the changes in the vibrational amplitude at constant volume also called explicit contribution and 2. A quasiharmonic contribution due to the changes in interatomic interactions brought out by volume change alone known as implicit contribution.

$$\left.\frac{d\omega_i}{dT}\right|_P = \left.\frac{\partial\omega_i}{\partial T}\right|_V + \left.\frac{\partial\omega_i}{\partial V}\right|_T \left.\frac{\partial V}{\partial T}\right|_P \quad (1.4)$$

where V is the volume and P the pressure. By dividing the above equation by ω_i and using the standard definitions of mode Gruneisen parameter $\gamma_i(q) = -\left(\frac{\partial \ln \omega_i}{\partial \ln V}\right)$ and thermal expansion coefficient $\alpha = \frac{1}{V}\left(\frac{\partial V}{\partial T}\right)$, we obtain

$$\frac{1}{\omega_i} \left.\frac{d\omega_i}{dT}\right|_P = \frac{1}{\omega_i} \left.\frac{\partial\omega_i}{\partial T}\right|_V - \gamma_i \alpha \quad (1.5)$$

The first term on the right hand side is the true anharmonic contribution and the second term is quasiharmonic.³

In the quasiharmonic model, phonon modes behave harmonically with infinite lifetimes, but their frequencies are changed by the effects of volume on the interatomic potential.⁴ Explicit anharmonicity originates with phonon-phonon interactions, which increase with temperature. These explicit temperature dependent anharmonic effects have significant effect at temperatures much higher than the Debye temperature.⁴ The thermal expansion coefficient α is related to Gruneisen parameter γ through the relation:

$$\alpha = \frac{\gamma_{av}\chi_T C_V(T)}{V_0} \quad (1.6)$$

where χ_T , C_V , γ_{av} and V_0 are respectively the isothermal volume compressibility, specific heat capacity, average Gruneisen parameter and molar volume at $T= 0$ K. Since the values of B_0 , C_V and V_0 are always positive, the value of α is determined by the sign of γ_{av} . A negative value of γ_{av} implies negative value of α and the solid contracts with increasing temperature. For many materials, α and heat capacity C_V have similar temperature dependence, as predicted by models for vibrations in solids.⁵ The average Gruneisen parameter is given by,

$$\gamma_{av} = \frac{\sum c_i \gamma_i}{\sum c_i} \quad (1.7)$$

where c_i is the contribution of the i^{th} phonon mode to the overall specific heat, C_V at constant volume.

Materials can be divided into three groups on the basis of their coefficient of thermal expansion⁶:

High Expansion Group: $\alpha > 8 \times 10^{-6} \text{ K}^{-1}$

Intermediate Group: $2 < \alpha < 8 \times 10^{-6} \text{ K}^{-1}$

Low Expansion Group: $\alpha < 2 \times 10^{-6} \text{ K}^{-1}$

1.1.1 Low thermal expansion

Low thermal expansion group include materials with low positive, nearly zero and negative thermal expansion (NTE) coefficient. These materials are interesting due to their high thermal shock resistance and enhanced dimensional stability.⁶⁻⁸ Several excellent reviews⁹⁻¹¹ have been published on NTE materials and the possible mechanisms for their behaviour. There are some general structural features that can be associated with compounds exhibiting low thermal expansion,⁶ which include 1) strongly bonded polyhedra linked in three dimensions, 2) open, flexible structures, 3) rigid polyhedra that can freely tilt back and forth with little or no change in shape and 4) ferromagnetic or ferroelectric micro domains.

The following mechanism is relevant to basically all open framework oxide materials, where the oxygen (O) is coordinated to just two metal (M) atoms^{13,14} where the M-O-M links are linear or close to linear. Provided that the M-O bonds in the structure are sufficiently strong and therefore show insignificant expansion (the polyhedra are rigid), the average metal-metal distance will decrease as the bridging oxygen in an M-O-M unit vibrates with increasing amplitude (see Figure 1.2). In a three dimensional solid, each vibration will result in a rocking motion of the polyhedra that are connected by the respective oxygen. For NTE to occur, all polyhedra must tilt back and forth in a cooperative fashion with a net displacement of the equilibrium position with temperature resulting in a reduction in overall volume or at least one of the dimensions. Figure 1.2 depicts an example of how such a cooperative motion can result in a reduction in the average metal-metal distances.

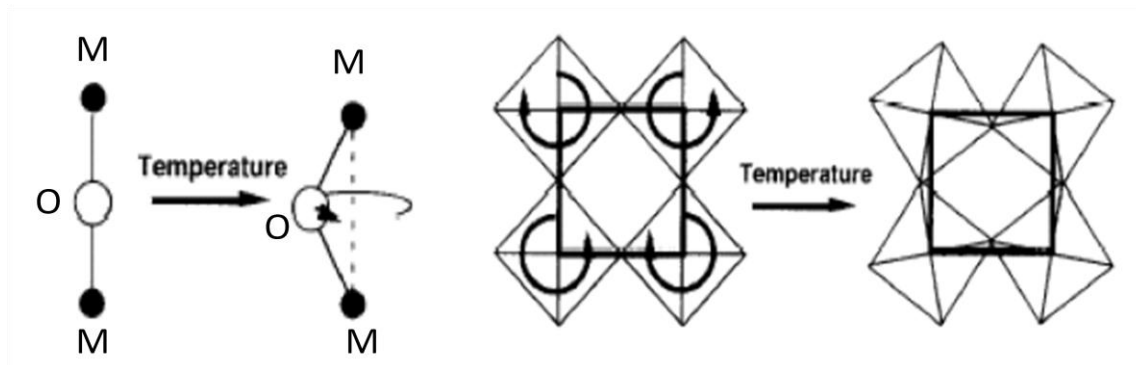


Figure 1.2 Representation of the transverse vibrational motion of an oxygen atom in a M-O-M linkage resulting in negative thermal expansion. A cooperative rotation of the polyhedra causes a decrease in the average metal-metal distances.¹⁵

Materials like $\text{Zn}(\text{CN})_2$,¹⁶ Prussian blue analog $\text{Fe}[\text{Co}(\text{CN})_6]^{17}$ with metal–cyanide–metal (M–CN–M′) linkage are fundamentally different from NTE materials with oxygen bridging framework M–O–M′ linkages. M–CN–M′ linkages might give rise to a local NTE effect: The moiety possesses two transverse vibrational modes similar to the bending mode of M–O–M′ bridges. The first of these involves displacement of the C and N atoms away from the M⋯M′ axis in the same direction; in the second, the displacement occurs in opposite directions (Figure 1.3). Both modes have the effect of drawing the anchoring metal atoms closer together with increasing temperature. This intrinsic flexibility of CN linkages favours the existence of a large number of low frequency NTE vibrational modes.¹⁸

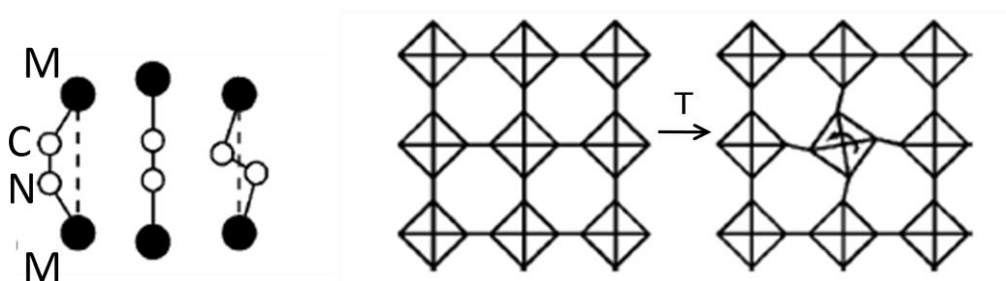


Figure 1.3 A representation of local vibrational modes responsible for NTE behavior in structures containing diatomic linkages. The filled circles represent heavy (usually metal)

atoms, and the open circles represent light bridging atoms, of CN species. With increase in temperature, population of these vibrational modes leads to a decrease in the overall metal-metal distance. (Goodwin *et al*)¹⁸

For a more sophisticated understanding of this mechanism, one has to consider lattice vibrational modes in the solid. Quantised lattice vibrational modes, also called phonon modes, are cooperative vibrational modes of all atoms in a solid. Low frequency modes due to large amplitude transverse vibrations of O or CN linkages which occur through coupled oscillations of polyhedra with no change in intra-unit bond angle or without distortions or interference with other polyhedra can be excited even at low temperatures.¹⁹ These modes are also called “Rigid unit modes” or RUMs, as the polyhedra remain mostly undistorted (rigid). If the polyhedra in the material are essentially rigid and they can rock back and forth without significant distortions or interference with other polyhedra, then low-energy vibrational modes may be present that can result in NTE.²⁰⁻²²

It has been shown for several NTE materials including cubic ZrW_2O_8 , HfW_2O_8 and $ZrMo_2O_8$ that the NTE behavior is driven by low-frequency vibrational modes that are associated with large negative Grüneisen parameters.²³⁻²⁴ Recent research on oxide NTE compounds has focused on materials that fall into the following five network types: the AM_2O_7 family,²⁵⁻²⁶ the AM_2O_8 family,²⁷⁻²⁹ the $A_2M_3O_{12}$ family,^{30, 31} AO_2 networks or framework silicates and aluminophosphates (zeolites)³² and AMO_5 ^{33,34} networks. The expansion coefficient of compounds of $Na_{1+x}Zr_2P_{3-x}Si_xO_{12}$ (NASICON)³⁵ family changes from strongly positive to slightly negative with decreasing x . This observation led to the discovery of the family of low expansion materials with $NaZr_2P_3O_{12}$ (NZP) and $CaTi_4P_6O_{24}$ (CTP) as the parent compounds. In these systems, Na, Zr and P can be substituted by a variety of ions, which offers the possibility of tailoring the thermal expansion coefficients.

$\text{CaZr}_4\text{P}_6\text{O}_{24}$ (CZP) and $\text{SrZr}_4\text{P}_6\text{O}_{24}$ (SZP) show anisotropy that is opposite to each other.³⁶ While CZP contracts along a and b and expands along c axis, SZP shows the opposite behavior with contraction along c and expansion along a and b . The combination of these two materials with composition $\text{Ca}_{0.75}\text{Sr}_{0.25}\text{Zr}_4\text{P}_6\text{O}_{24}$ could be synthesized that showed CTE close to zero thermal expansion both along the a/b and c -axes.³⁶

In addition, some MX_3 network structures which also consist of rigid, corner-sharing metal-anion octahedra show very low thermal expansion especially relative to typical metal oxides. These materials have the cubic ReO_3 structure^{37,38} and include NbO_2F and TaO_2F .³⁹ While NbO_2F shows low positive thermal expansion, the value of CTE for TaO_2F exhibits nearly zero thermal expansion.⁴⁰ Metal-organic compounds such as $\text{Sr}(\text{C}_2(\text{COO})_2)$ with open framework structures formed by metal ions coordinated to polydentate organic ligands show low thermal expansion below room temperature.⁴¹ Isotropic polyacrylamide film containing *s*-dibenzocyclooctadiene (DBCOD) polymer exhibits reversible giant thermal contraction of approximately -1200 ppm K^{-1} ranging from 290-350 K due to submolecular conformational change.⁴²

1.1.2 Colossal anisotropic thermal expansion

Framework structured inorganic compounds represent an important class of materials that exhibit unusual properties such as colossal uniaxial negative thermal expansion (NTE) and negative linear compressibility (NLC). Compounds like α' - NaV_2O_5 ,⁴³ $\text{Pb}_{0.7}\text{Ca}_{0.3}\text{TiO}_3$,⁴⁴ NbOPO_4 ,⁴⁵ $\text{Ag}_3[\text{Co}(\text{CN})_6]$ ⁴⁶ exhibit anisotropic NLC property. A three dimensional hybrid (inorganic-organic) framework $[\text{NH}_4][\text{Zn}(\text{HCOO})_3]$ was reported to exhibit NLC (-1.8 TPa^{-1}) up to 1 GPa. A

combination of contraction of Zn-O bonds and tilting of formate ligands with increasing pressure is considered to be the primary cause for NLC effect in this material.⁴⁷ Cyanide containing frameworks are more flexible than their oxide bridged analogues.⁴⁸ Cyanides such as $\text{Zn}(\text{CN})_2$,⁴⁹ $\text{Cd}(\text{CN})_2$,⁵⁰ $\text{H}_3[\text{Co}(\text{CN})_6]$,⁵¹ $\text{M}(\text{CN})_2$ ⁵² and the family of $\text{MPt}(\text{CN})_6$ ⁵³ (where M is a metal) are known to exhibit NTE property. NTE in these compounds is known to be due to low frequency transverse bending modes of the rigid $\text{C}\equiv\text{N}$ groups. Trigonal $\text{Ag}_3[\text{Co}(\text{CN})_6]$ exhibits colossal anisotropic TE ($\alpha_c = -130 \text{ MK}^{-1}$ and $\alpha_a = +140 \text{ MK}^{-1}$)⁵⁴ from 16 K to its decomposition temperature (500 K) and linear compressibility ($K_c = -76 \text{ TPa}^{-1}$ and $K_a = +115 \text{ TPa}^{-1}$) from 0-0.19 GPa.⁴⁶ Above 0.19 GPa, the NLC coefficient reduces to -5 TPa^{-1} due to phase transformation to a monoclinic structure.⁴⁶ The NLC/NTE effect arises as the rapid compression/contraction of layers of silver atoms—weakly bound via argentophilic interactions—are translated via flexing of the covalent network lattice into an expansion along a perpendicular direction. (Figure 1.4). Density functional theory calculations quantify both the low energy associated with this flexibility and the role of argentophilic ($\text{Ag}^+ \dots \text{Ag}^+$) interactions. High pressure Raman spectroscopic studies on $\text{Ag}_3[\text{Co}(\text{CN})_6]$ have revealed negative Gruneisen parameters for the Co-CN bending modes and amorphization of the structure above 12 GPa.⁵⁵

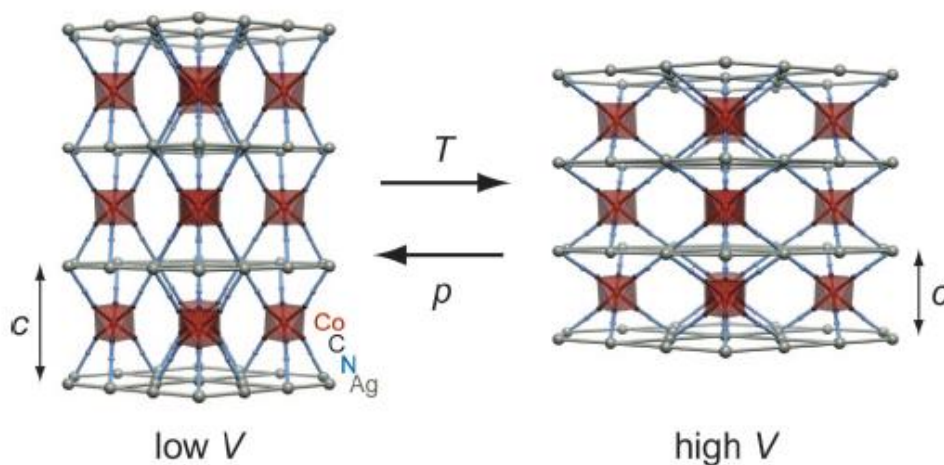


Figure 1.4 Compression mechanism in $\text{Ag}_3[\text{Co}(\text{CN})_6]$, exaggerated for illustrative purposes: In order for the framework to reduce its volume (either in response to a decrease in temperature or an increase in pressure), it must expand along the trigonal axis (c). (Goodwin et al)⁴⁶

$\text{KMn}[\text{Ag}(\text{CN})_2]_3$ is similar to $\text{Ag}_3[\text{Co}(\text{CN})_6]$ in structure with additional K^+ ions in cavities of dicyanometallate framework and exhibits strong NLC ($K_c = -12 \text{ TPa}^{-1}$; $0 < P < 2.2 \text{ GPa}$) and anisotropic NTE ($\alpha_c = -60 \text{ MK}^{-1}$, $\alpha_a = +61 \text{ MK}^{-1}$) from 100 to 300 K. NTE/NLC effect is explained by ‘wine-rack’ type connectivity in the framework structure.⁵⁶ It has also been demonstrated that deuterated methanol monohydrate, a simple molecular orthorhombic crystal exhibits both NLC ($K_a = -3.1 \text{ TPa}^{-1}$; $0-0.6 \text{ GPa}$ at 160 K) and NTE.⁵⁷ Here, NLC is caused by a ‘triangular shortening’ mechanism.⁵⁸ Although it is not possible to say that NTE and NLC are thermodynamically required to coexist, it does seem likely that a general correspondence is observed for above framework materials.

Though trigonal $\text{Ag}_3[\text{Co}(\text{CN})_6]$ shows a large anisotropic NLC coefficient, this structure is not stable above 0.19 GPa. Deuterated methanol monohydrate is found to be stable only below 160 K. Interestingly, trigonal $\text{KMn}[\text{Ag}(\text{CN})_2]_3$ shows high NLC coefficient up to 2 GPa because the K^+ counter ions frustrate the soft phonon modes

responsible for pressure induced phase transition leaving low energy modes responsible for NLC and NTE undamped.⁵⁶ But there were no studies on the role of the various phonon modes to negative linear compressibility (NLC), anisotropic thermal expansion and stability of the structure at higher pressures (> 2 GPa) and temperatures (>300 K).

1.2. Materials investigated and reported in this dissertation

1.2.1. Alkali substituted NZP compounds

Compounds with the general formula $AZr_2(XO_4)_3$ (A= Na, K, Rb and Cs) are known to adopt rhombohedral crystal structure. The whole family of compounds sharing the same topology in their skeleton is generally represented by [NZP] and the term NASICON is used in the area of solid electrolytes and ionic conductivity.⁵⁹ $NaZr_2P_3O_{12}$ is the parent prototype of NZP family. Materials of this family have now attracted wide attention for their variety of useful properties and behavior such as ultralow-thermal expansion,⁶⁰ superionic conductivity,⁶¹ ability to accommodate radioactive waste,⁶² and flexibility toward ionic substitutions at various lattice sites in the structure.⁶³ Due to the mobility of Na ions tunneling through polyhedral chains, prototypic $NaZr_2(PO_4)_3$ was recently identified as anode material for sodium ion batteries.⁶¹ These NZP materials crystallize in a rhombohedral structure with $R\bar{3}c$ space group and consist of a three-dimensional skeletal framework of PO_4 tetrahedra sharing corners with ZrO_6 octahedra. Each ZrO_6 octahedron is connected to six PO_4 tetrahedra, while each PO_4 tetrahedron is connected to four ZrO_6 octahedra. The basic unit of the network consists of two octahedra and three tetrahedra corresponding to $[Zr_2P_3O_{12}]^-$, and these units are connected to form ribbons or chains along the c axis. The ribbons are joined together by PO_4 tetrahedra perpendicular to the c axis to

develop a three-dimensional network.⁶⁴ A schematic diagram of NZP is shown in Figure 1.5. These ribbons and chains create structural holes in the structure. These structural holes are completely or partially occupied by *A* ions depending upon the composition. There are one Na(1), three Na(2) and six mid-Na sites per unit formula ($\text{NaZr}_2(\text{PO}_4)_3$) and one unit cell consists of six formula units. These sites are interconnected in three dimensions giving rise to a network of the conduction channel. An Na(1) is six-coordinated with Na(2) sites which are two coordinated with Na(1) sites. The mid-Na site is located mid-way in the conduction channel connecting an Na(1) and an Na(2). In $\text{NaZr}_2(\text{PO}_4)_3$ the Na^+ occupies only the Na(1) sites at room temperature.⁶⁷ The corner sharing, rather than edge sharing, of the ZrO_6 and PO_4 polyhedra gives rise to a fairly open framework structure with structural holes. The presence of the structural holes provides the polyhedra with some freedom for rotational motion.⁶⁷ Many interesting properties of NASICONs, like the low and anisotropic thermal expansion, high shock resistance, flexibility to incorporate ions of varying sizes etc., are often attributed to the presence of structural holes.

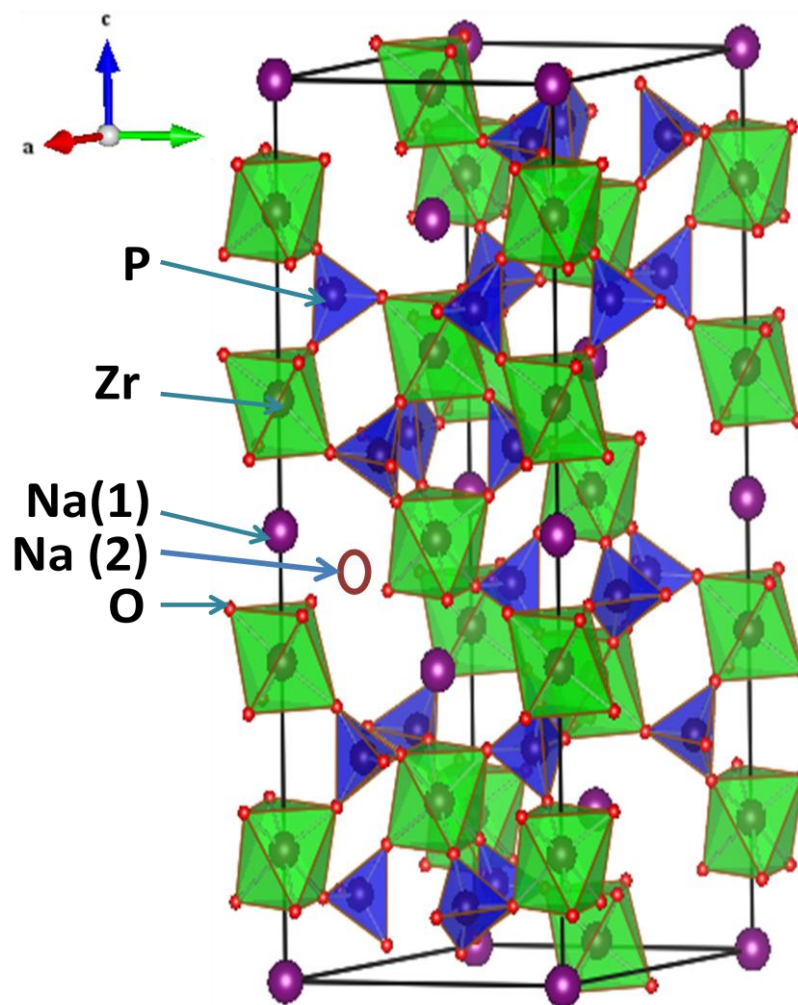


Figure 1.5 A view of the $\text{NaZr}_2(\text{PO}_4)_3$ structure parallel to the c -axis. Corner-shared ZrO_6 -octahedra and PO_4 -tetrahedra with Na(1) and Na(2) interstitial sites are clearly seen.

Thermal expansion of c -axis causes the expansion of the columns in the structure which in turn strains the PO_4 tetrahedral bridge linking the $\text{O}_3\text{ZrO}_3\text{A}^1\text{O}_3\text{ZrO}_3$ groups in the direction of the c -axis, so that the O-P-O bond angles spread in the direction of the c -axis. Consequently, the PO_4 tetrahedra contract in the direction normal to this expansion and hence the thermal expansion coefficient along a -axis is negative.⁶⁴

Some compounds of NZP family like $\text{NaSn}_2(\text{PO}_4)_3$,⁶⁵ $\text{Na}_5\text{Zr}(\text{PO}_4)_3$,⁶⁶ $\text{Na}_5\text{Hf}(\text{PO}_4)_3$ ⁶⁶ show high temperature reversible phase transition in the temperature range 673-723 K, 389-424 K and 476-572 K respectively and remain stable up to 1273 K but very

few or no studies have been reported as a function of pressure. Hence it is interesting to study this family of ceramics at high pressures. In this thesis, we will discuss high pressure studies on alkali substituted NZP compounds.

1.2.2. TaO₂F

TaO₂F and NbO₂F were structurally characterized by Frevel and Rinn in 1956.³⁹ At ambient conditions they adopt the cubic ReO₃ structure, space group *Pm-3m*, which can be thought of as an undistorted *ABX₃* perovskite with empty *A* sites (Figure 1.6). For both TaO₂F and NbO₂F, the O and F atoms occupy the same crystallographic site. Thus, their long range average structures are very similar. The ReO₃ structure is relatively low in density and there is potentially considerable flexibility associated with tilting of the ReO₆ octahedra. While both ReO₃ and NbO₂F show low positive thermal expansion,⁶⁸ TaO₂F exhibits nearly zero thermal expansion from 20 to 400 K.⁴⁰

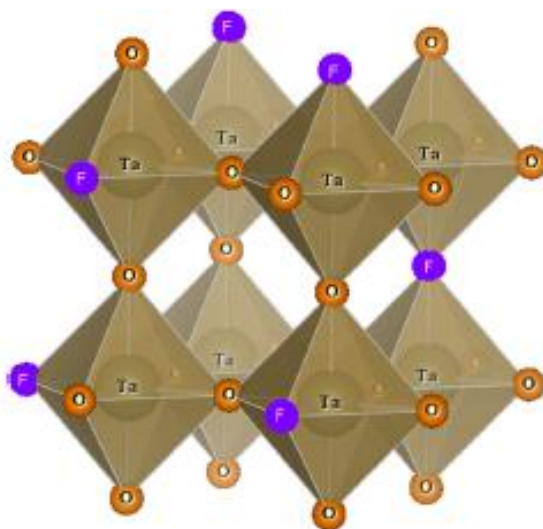


Figure 1.6. Schematic representation of crystal structure of TaO₂F adopting cubic ReO₃ structure with corner sharing Ta(O/F)₆ octahedra.

These same characteristics also predispose ReO_3 type materials to interesting behavior on modest compression. While the framework octahedra are quite rigid, the void spaces between them readily allow for volume reduction by tilting of the octahedra. Structural changes resulting from octahedral rotations in perovskite related materials have been carefully explored by several workers.⁶⁹

The local structure of TaO_2F is poorly described by an ideal cubic ReO_3 -type model with O and F randomly distributed over the available anion sites. A supercell model featuring $-\text{Ta}-\text{O}-\text{Ta}-\text{O}-\text{Ta}-\text{F}-$ chains along $\langle 1\ 0\ 0 \rangle$, with different Ta–O and Ta–F distances and O/F off-axis displacements, gives good agreement with pair distribution functions (PDFs) derived from total X-ray scattering studies for small distances ($r < 8\ \text{\AA}$). Experimental PDF data provides an excellent fit for larger r ($> 8\ \text{\AA}$) with ideal cubic ReO_3 model. Analysis of PDFs derived from variable temperature measurements (80 to 487 K) at larger r exhibit nearly an average zero expansion coefficients with weighted average of Ta–O–Ta and Ta–F–Ta separations.⁷⁰ A single representative $-\text{Ta}-\text{O}-\text{Ta}-\text{O}-\text{Ta}-\text{F}-$ chain in the TaO_2F supercell model is shown in Figure 1.7.

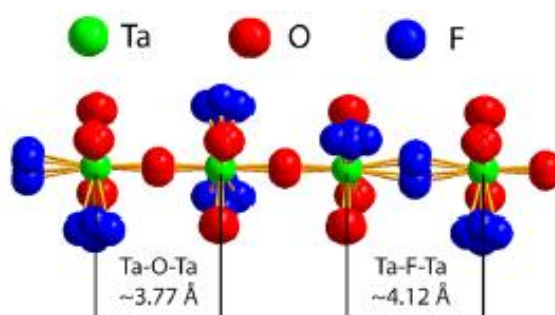


Figure 1.7 Single $-\text{Ta}-\text{O}-\text{Ta}-\text{O}-\text{Ta}-\text{F}-$ chain from the TaO_2F supercell model. (Morelock *et al*)⁷⁰

1.2.3. $\text{KMn}[\text{Ag}_3(\text{CN})_6]$

The structure of $\text{KMnAg}_3(\text{CN})_6$ consists of three interpenetrating trigonally distorted cubic lattices of composition $\text{MnAg}_3(\text{CN})_6^-$ and intercalated K^+ ions. The six-coordinated Mn atoms occupy the corners of the cubes, whereas the two-coordinate Ag atoms are found in the middle of the cube edges. The cyanide groups bridge the Mn and Ag atoms. Alternatively, the structure can be thought of as being composed of close-packed double layers of cyanide ions, with one third of the octahedral holes filled by Mn, and another third by K atoms. The C atoms of the cyanide groups protrude out of the double layer in a tilted direction (along the $a+c$ diagonal), and Ag^+ ions then bridge the double layers via C–Ag–C bonds.⁷⁰ The structure of $\text{KMn}[\text{Ag}(\text{CN})_2]_3$, which has been reported previously,⁵⁶ is closely related to that of $\text{Ag}_3[\text{Co}(\text{CN})_6]$. Both share the motifs responsible for extreme NTE/NLC: an ultraflexible cyanide lattice whose dimensions are determined by low-energy $\text{Ag}^+ \cdots \text{Ag}^+$ argentophilic interactions [Figure 1.8(a)].⁵⁴ Inclusion of K^+ ions within cavities of the dicyanometallate framework is found to be the key modification in lowering the crystal symmetry from $P31m$ in $\text{Ag}_3[\text{Co}(\text{CN})_6]$ to $P312$ in $\text{KMn}[\text{Ag}(\text{CN})_2]_3$. It has been reported that since K^+ is not covalently bound to the framework, NTE/NLC behavior and structural flexibility would largely be retained.⁵⁶

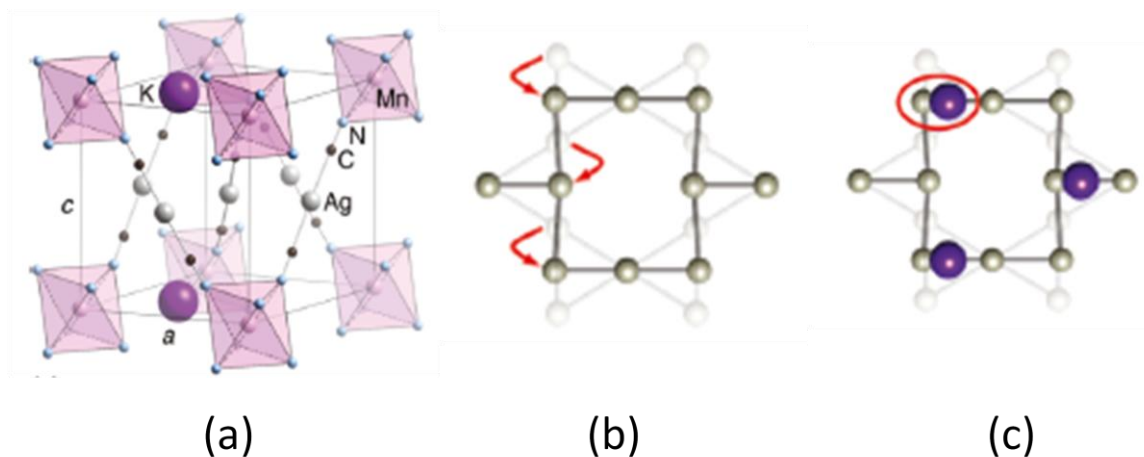


Figure 1.8 (a) Crystal structure of $\text{KMn}[\text{Ag}(\text{CN})_2]_3$: $[\text{MnN}_6]$ octahedra are connected via almost linear NC-Ag-CN units, with K^+ ions positioned above and below alternating Ag_3 Kagome triangles. (b) Re-arrangement of the Ag Kagome sublattice coupled to framework shear in $\text{Ag}_3[\text{Co}(\text{CN})_6]$ is shown in arrows which is viewed along c -axis. (c) These displacements would give unphysical $\text{Ag}^+ \cdots \text{K}^+$ distances in $\text{KMn}[\text{Ag}(\text{CN})_2]_3$; the soft mode responsible for phase transition is stiffened. (Cairns *et al*)⁵⁶

It is expected that by virtue of its interaction with the Kagome sublattice of Ag^+ ions, K^+ ions would influence strongly the existence of a high-pressure phase transition. Cairns *et al* observed that that the shear instability responsible for volume collapse in $\text{Ag}_3[\text{Co}(\text{CN})_6]$ is coupled to a translation of two-thirds of the Ag^+ ions to a site that in $\text{KMn}[\text{Ag}(\text{CN})_2]_3$ would result in a very short $\text{K}^+ \cdots \text{Ag}^+$ contact [Figure 1.8 (b,c)]. Hence, the presence of K^+ ions was found to selectively stiffen the soft-mode responsible for a pressure-induced phase transition, while leaving the low-energy modes that drive NTE and NLC essentially undamped.⁵⁶

1.3. High pressure behavior of anomalous thermal expansion materials

Low thermal expansion compounds may find application as pure phases and as components in composite materials with tailored thermal expansion coefficients.⁷²⁻

⁷³ During the manufacture of these materials, pressures above ambient may be encountered leading to phase transitions and a loss of low thermal expansion behavior.⁷⁴⁻⁷⁵ Many NTE materials have open frameworks and, owing to their flexibility and relatively low densities, commonly display crystalline-to-crystalline phase transitions,⁷⁶ and pressure induced amorphization^{77,78} under moderate compression. Phase transitions at pressures above ambient have been reported for many NTE materials (cubic ZrMo_2O_8 ,^{79, 80} and $\text{Sc}_2\text{W}_3\text{O}_{12}$ ⁸¹). In general, these pressure-induced phase transitions involve tilting of rigid polyhedral units with an associated decrease in unit cell volume and lowering of the symmetry. From applications perspective, the most important aspect is that the linear thermal expansion coefficient exhibited by the ambient pressure structure is changed drastically after phase transitions. The cubic-to-orthorhombic phase transformation in ZrW_2O_8 occurring around 0.2 GPa results in an almost ten-fold reduction of the negative coefficient of thermal expansion. The variation or loss of the low thermal expansion property on compression adversely affects their applicability in structural materials, as they may be subjected to high pressures during processing of composites with tailored thermal expansion.⁸²

Very thin aligned coatings of a material such as $\text{Ag}_3[\text{Co}(\text{CN})_6]$ or $\text{KMnAg}_3(\text{CN})_6$ could provide an intrinsic protection against temperature gradients in optical devices of satellites, avoiding the present reliance on mechanical adjustment.⁵⁴ Strong NTE of these compounds may yet be found to exhibit equally strong NLC behavior. NLC materials will facilitate technological exploitation of their unusual compressibilities. Such materials could be used in high-pressure environments, such as in optical telecommunications devices and ultrasensitive pressure detectors, such as interferometric optical sensors for sonar and aircraft altitude measurements. The

effect is also often coupled to so-called “auxetic” behavior, which is itself being used to improve shock resistance in, e.g., body armor.⁴⁶ Optically transparent NTE/NLC framework materials—such as $\text{Ag}_3[\text{Co}(\text{CN})_6]$ and $\text{KMnAg}_3(\text{CN})_6$ would present the first realistic candidates for such applications.

1.4. References

- ¹ C. Y. Ho and R. E. Taylor et al, *Thermal expansion of solids* (CINDAS data series on material properties: v. I-4), 1998.
- ² N. L. Vocadlo and G. D. Price, *Phys. Earth Planet. Inter.* **82**, 261 (1994).
- ³ R. Zallen and E. M. Conwell, *Solid State Commun.* **31**, 557 (1979).
- ⁴ B. Yates, *Thermal expansion*, New York, 1972.
- ⁵ P.Bruesch, *Phonons: Theory and Experiments*, Berlin, Germany: Springer Verlag, 1982.
- ⁶ R. Roy, D. K. Agrawal and H. A. McKinstry, *Annu. Rev. Mater. Sci.* **19**, 59 (1989).
- ⁷ M. A. White, *Properties of Material*, Oxford University Press, New York, 1999.
- ⁸ M. B. Jakubinek, C. A. Whitman, and M. A. White, *Therm. Anal. Calorimetry* **99**, 165 (2010).
- ⁹ A. W. Sleight, *Endeavour* **19**, 64 (1995).
- ¹⁰ A. W. Sleight, *Inorg. Chem.* **37**, 2854 (1998).
- ¹¹ J. S. O. Evans, *J. Chem. Soc. Dalton Trans.* **33**, 17 (1999).
- ¹² G. D. Barrera, J. A. O. Bruno, T. H. K. Barron and N. L. Allan, *J. Phys. Condens. Matter* **17**, R217 (2005).
- ¹³ A. W. Sleight, *Curr. Opin. Solid State Mater. Sci.* **3**, 128 (1998).
- ¹⁴ A. W. Sleight, *Annu. Rev. Mater. Sci.* **28**, 29 (1998).
- ¹⁵ J. S. O. Evans, T. A. Mary and A. W. Sleight, *Physica B* **311**, 241 (1998).
- ¹⁶ D. Williams, D. E. Partin, F. J. Lincoln, J. Kouvetakis, and M.O’Keeffe, *J. Solid State Chem.* **134**, 164 (1997).
- ¹⁷ S. Margadonna, K. Prassides, and A. N. Fitch, *J. Am. Chem. Soc.* **126**, 15390 (2004).
- ¹⁸ A. L. Goodwin and C. J. Kepert, *Phys. Rev. B*, **71**, 140301 (2005).
- ¹⁹ T. A. Mary, J. S. O. Evans, T. Vogt and A. W. Sleight, *Science* **272**, 90 (1996).

- ²⁰A. K. A. Pryde, K. D. Hammonds, M. T. Dove, V. Heine, J. D. Gale and M. C. Warren, *J. Phys. Condens. Matter* **8**, 10973 (1996).
- ²¹A. K. A. Pryde, K. D. Hammonds, M. T. Dove, V. Heine V, J. D. Gale and M. C. Warren, *Phase Transitions* **61**,141 (1997).
- ²²R. Mittal, S. L.Chaplot, H. Schober and T. A. Mary, *Phys. Rev. Lett.* **86**, 4692 (2001).
- ²³Y. Yamamura, N. Nakajima, T. Tsuji, Y. Iwasa, K. Saito and M. Sorai, *Solid State Commun.* **121**, 213 (2002).
- ²⁴K. Wang and R. R. Reeber, *Appl. Phys. Lett.* **76**, 2203 (2000).
- ²⁵J. S. O. Evans, J. C. Hanson and A. W. Sleight, *Acta Crystallogr. B* **54**, 705 (1998).
- ²⁶R. L. Withers, J. S. O. Evans, J. Hanson and A. W. Sleight, *J. Solid State Chem.* **137**, 161 (1998).
- ²⁷J. S. O. Evans, T. A. Mary, T. Vogt, M. A. Subramanian and A. W. Sleight, *Chem. Matter* **8**, 2809 (1996).
- ²⁸T. A. Mary, J. S. O. Evans, T. Vogt and A. W. Sleight, *Science* **272**, 90 (1996).
- ²⁹C. Lind, A. P. Wilkinson, Z. Hu, S. Short and J. D. Jorgensen, *Chem. Mater.* **10**, 2335 (1998).
- ³⁰J. S. O. Evans, T. A. Mary and A. W. Sleight, *J. Solid State Chem.***137**, 148 (1998).
- ³¹T. A. Mary and A. W. Sleight, *J. Mater. Res.***14**, 912 (1999).
- ³²P. Tschaufeser and S. C. Parker, *J. Phys. Chem.* **99**, 10609 (1995).
- ³³M. P. Attfield and A. W. Sleight, *Chem. Mater.* **10**, 2013 (1998).
- ³⁴D. A. Woodcock, P. Lightfoot, P. A. Wright, L. A. Villaescusa, M-J Díaz-Cabañas and M. A. Cambor, *J. Mater. Chem.* **9**,349 (1999).
- ³⁵J. P. Boilot, J. P. Salanie, and G. Desplanches, *Mat. Res. Bull.* **14**, 1469 (1979).
- ³⁶S. Limaye, D. K. Agarwal, R. Roy and P. Mehrotra, *J. Mater. Sci.* **26**, 93 (1991).

- ³⁷T. G. Amos and A. W. Sleight, *J. Solid State Chem.***160**, 230 (2001).
- ³⁸T. G. Amos, A. Yokochi and A. W. Sleight, *J. Solid State Chem.***141**, 303 (1998).
- ³⁹L. K. Frevel and H. W. Rinn, *Acta Crystallogr.* **9**, 626 (1956).
- ⁴⁰J. Z. Tao and A. W. Sleight, *J. Solid State Chem.***173**, 45 (2003).
- ⁴¹F. Hohn, I. Pantenburg and U. Ruschewitz, *Chem. Eur. J.* **8**, 4536 (2002).
- ⁴²X. Shen, C. Viney, E. R. Johnson, C. Wang and J. Q. Lu, *Nature Chem.* **5**, 1035 (2013).
- ⁴³M. Koppen, D. Pankert, and R. Hauptmann, M. Lang, M. Weiden, C. Geibel, and F. Steglich, *Phys. Rev. B* **57**, 8466 (1998).
- ⁴⁴A. Chandra, D. Pandey, A. K. Tyagi and G. D. Mukerjee, *Appl. Phys. Lett.* **90**, 142903 (2007).
- ⁴⁵G. D. Mukherjee et al, *J Solid State Chem.* **160**, 230 (2005).
- ⁴⁶A. L. Goodwin, D. A. Keen and M. G. Tucker, *Proc. Natl. Acad. Sci.* **105**, 18708 (2008).
- ⁴⁷W. Li et al, *J. Am. Chem. Soc.***134**, 11940 (2012).
- ⁴⁸A. L. Goodwin, *Z. Kristallogr. Suppl.* **30**, 1 (2009).
- ⁴⁹T. R. Ravindran, A. K. Arora, Sharat Chandra, M. C. Valsakumar and N. V. Chandrashekar, *Phys. Rev. B* **76**, 054302 (2007).
- ⁵⁰P. Ding, E. J. Liang, Y. Jia and Z. Y. Du, *J. Phys.: Matter* **20**, 275224 (2008).
- ⁵¹D. A. Keen, M.T. Dove, J. S.O. Evans, A. L. Goodwin, L. Peters and M. G. Tucker, *J. Phys.: Matter* **22**,404202 (2010).
- ⁵²K.W. Chapman, P. J Chupas and C. J. Kepert, *J. Am. Chem. Soc.* **127**, 15630 (2005).
- ⁵³K.W. Chapman, P. J. Chupas and C. J. Kepert, *J. Am. Chem. Soc.* **128**, 7009 (2006).
- ⁵⁴A. L. Goodwin, M. Calleja, M. J. Conterio, M. T. Dove, J. S. O. Evans, D. A. Keens, L. Peters and M. G. Tucker, *Science* **319**, 794 (2008).

- ⁵⁵R. Rao, S. N. Achary, A. K. Tyagi and T. Sakuntala, *Phys. Rev. B* **84**, 054107 (2011).
- ⁵⁶A. B. Cairns, A. L. Thompson, M. G. Tucker, J. Haines and A. L. Goodwin, *J. Am. Chem. Soc.* **134**, 4454 (2012).
- ⁵⁷A. D Fortes, E. Suard and K. S Knight, *Science* **331**, 742 (2011).
- ⁵⁸J. N. Grima, D. Attard and R. Gatt, *Physica Stat. Solidi. B* **245**, 2405 (2008).
- ⁵⁹J. Alamo, *Solid State Ionics* **63**, 547 (1993).
- ⁶⁰V. I. Petkov, A. I. Orlavo, G. N. Kasantsev, S. G. Samoilov, and M. L. Spiridonova, *J. Therm. Anal. Cal.* **66**, 623 (2001).
- ⁶¹W. Wang, B. Jiang, L. Hu and S. Jiao, *J. Mater. Chem. A* **2**, 1341 (2014).
- ⁶²B. E. Scheetz, D. K. Agarwal, E. Breval and R. Roy, *Waste Management* **14**, 489 (1994).
- ⁶³G. E. Lenain, H. A. McKinstry, S. Limaye and A. Woodward, *Mater. Res. Bull.* **19**, 1451 (1984).
- ⁶⁴T. Oota and I. Yamai, *J. Am. Ceram. Soc.* **69**, 1 (1986).
- ⁶⁵J. L. Rodrigo and J. Alamo, *Mat. Res. Bull.* **26**, 475 (1991).
- ⁶⁶V.I. Petkov and E. A. Asabina, *Indian J. Chem.* **52A**, 350 (2013).
- ⁶⁷P. Padma Kumar and S. Yashonath, *J. Chem. Sci.* **118**, 135 (2006).
- ⁶⁸D. Taylor *Br. Ceram. Trans. J.* **84**, 9 (1985).
- ⁶⁹A. M. Glazer *Acta Crystallogr. Section B* **28**, 3384 (1972).
- ⁷⁰C. R. Morelock, B. K. Greve, M. Cetinkol, K. W. Chapman, P. J. Chupas and A. P. Wilkinson, *Chem. Mater.* **25**, 1900 (2013).
- ⁷¹U. Geisers and J. A. Schlueter, *Acta. Cryst. C* **59**, i21 (2003).
- ⁷²R. C. Wetherfold and J. Wang, *Compos. Sci. Technol.* **53**, 1 (1995).
- ⁷³D. K. Balch and D. C. Dunand, *Metall. Mater. Trans. A* **35A**, 1159 (2004).

- ⁷⁴H. Holzer and D. C. Dunand, *J. Mater. Res.* **14**, 780 (1999).
- ⁷⁵S. Yilmaz, *J. Phys. Condens. Matter* **14**, 365 (2002).
- ⁷⁶A. Grzechnik and W. A. Crichton, *Solid State Sci.* **4**, 1137 (2002).
- ⁷⁷D. V. S. Muthu, B. Chen, J. M. Wrobel, A. M. Krogh, Andersen, S. Carlson and M. B. Kruger, *Phys. Rev. B* **65**, 064101 (2002).
- ⁷⁸B. Chen, D. V. S. Muthu, Z. X. Liu, A. W. Sleight and M. B. Kruger, *Phys. Rev. B* **64**, 214111 (2001).
- ⁷⁹C. A. Perottoni and J. A. H. de Jornada, *Science* **280**, 886 (1998).
- ⁸⁰C. Lind, D. G. VanDerveer, A. P. Wilkinson, J. Chen, M. T. Vaughan and D. J. Weidner, *Chem. Mater.* **13**, 487 (2001).
- ⁸¹T. Varga, A. P. Wilkinson, C. Lind, W. A. Bassett and C.-S. Zha, *Phys. Rev. B* **71**, 214106 (2005).
- ⁸²C. Verdon and D. C. Dunand, *Scr. Mater.* **36**, 1075 (1997).

Chapter 2

Experimental and computational details

2.1 Synthesis

In this section, we discuss methods of synthesis of various compounds such as alkali cation substituted NZP family, TaO_2F and $\text{KMn}[\text{Ag}_3(\text{CN})_6]$. The first two compounds are synthesised in ceramic form and the last one is grown as single crystals.

Ceramics, in contrast to metals, are often more resistant to oxidation, corrosion and wear; they are also better thermal insulators and a major role in materials engineering. Therefore, synthesis of ceramic powders is of importance in the progress of material science. There are several methods of synthesis of powder samples such as solid state reaction, chemical methods which include wet-dry, sol-gel, polymer sol-gel etc. Each method has its own advantages and drawbacks in achieving a quality product with respect to purity, homogeneity, particle size etc. These are important from the point of view of performance, reliability, reproducibility and economy. Sol gel method is a low-temperature technique that allows for fine control of the product's chemical composition and homogeneity. A discussion on synthesis of compounds of NZP family with various alkali ionic substitution and TaO_2F are outlined in Section 2.1.1 and 2.1.2.

$\text{KMn}[\text{Ag}_3(\text{CN})_6]$ belongs to the broad family of coordination polymers composed of metal cations and bridging ligands linked through coordinate bonds. Cyanometallates $[\text{M}(\text{CN})_x]^{y-}$ have been utilised as inorganic bridging ligands in coordination polymers,¹⁻³ widely used for magnetic applications. Recently, the

intricacies of thermal expansion in molecular compounds including flexible frameworks like coordination polymers ($\text{Ag}_3[\text{Co}(\text{CN})_6]$ and $\text{Ag}_3[\text{Fe}(\text{CN})_6]$) have been recognized.^{4,5} While the synthesis of the powder sample may be straight forward, the characterisation of a single crystal is more challenging; but single crystals enable us to carry out experiments like Polarised Raman measurements for mode assignments. Single crystals on such cyanometallate coordination polymeric compounds are obtained by variation of concentration, solvent or counter ions. Solvothermal methods are used for insoluble starting materials, slow evaporation of solvent and most commonly slow diffusion of solvent either layered through an H-shaped tube or through agar-gel. Synthesis of $\text{KMn}[\text{Ag}(\text{CN})_2]_3$ single crystals by a layering technique is discussed in Section 2.1.3.

2.1.1 Synthesis of compounds of NZP by sol gel method

Compounds of NZP with different alkali cations (Na, K, Rb and Cs) are synthesized by sol gel method. Sol-gel process is a wet-chemical technique widely used in the fields of material science and ceramic engineering to synthesize ceramic materials starting from a chemical solution (sol) which acts as a precursor to an integrated network (gel) of either discrete particles or network polymers. $\text{NaZr}_2(\text{PO}_4)_3$ (NZP) was synthesized by mixing stoichiometric quantities of precursor solutions of 1 M NaCl, 1.5 M ZrOCl_2 and 6 M H_3PO_4 .⁶ The order of mixing is important for homogeneity of the mixture. First, the NaCl and ZrOCl_2 solutions were mixed and H_3PO_4 was added slowly with constant stirring. The resultant mixture in the form of highly viscous slurry was heated at 70 °C for 24 hrs. The resulting gel was dried at 150 °C for 4 hrs and ground, calcined at 700 °C for 16 hrs, then finally heat treated at 1100 °C for 24 hrs to obtain NZP. Other compounds of NZP family with

different alkali cations like K, Rb and Cs were synthesized with their corresponding alkali halides and their sintering time increases with increasing size of alkali cation. Since the mobility of cation is lowered as the size increases, longer holding times and higher temperatures are required. XRD pattern of the resultant fine crystalline white powder matches with their corresponding JCPDS pattern without any impurity peaks.

2.1.2 Synthesis of TaO₂F by slow evaporation method

TaO₂F was prepared by dissolving Ta metal powder (Strem Chemicals, 99.8%) in a Pt crucible with concentrated HF (Mallinckrodt, 48%) followed by slow evaporation of HF to dryness. The remaining off-white powder was heated in an oven at 300 °C for 6 hrs. X-ray powder diffraction of the resulting white powder showed good match with JCPDS pattern [PDF No: 762370] with no impurity phases.

2.1.3 Synthesis of KMn[Ag(CN)₂]₃ by liquid diffusion method (layering technique)

Liquid diffusion technique is a convenient route to obtain small quantities of single crystals.⁷ An aqueous solution of manganese (II) nitrate hydrate is placed in a test tube and a mixture of (a) tetrapropylammonium bromide dissolved in absolute ethanol and (b) potassium dicyano-argentate (I) dissolved in water is layered carefully down the side of the tube on to the solution. This second liquid is less dense than, and miscible with, the solvent. The tube is then corked and left to stand undisturbed for 24 hours. As the precipitant diffuses into the solution, crystals form at the interface. Colorless hexagonal plates of KMnAg₃(CN)₆ formed within 1 day. We obtained crystals with typical dimensions of 0.6 mm×0.2 mm×0.03 mm. The steps involved in the growth of these single crystals are shown in Figure 2. 1. Powder X-ray diffraction

pattern on thoroughly ground single crystals matched well with corresponding JCPDS data [PDF No. 04-011-0797].

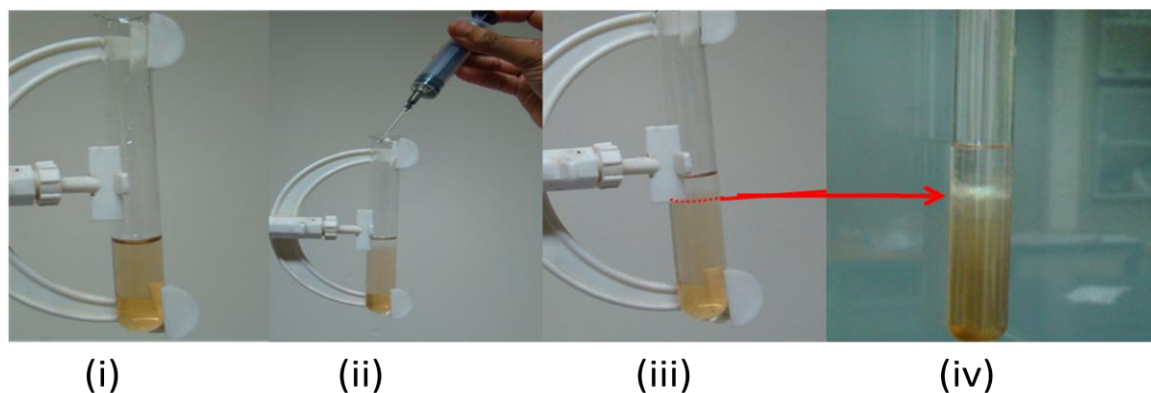


Figure 2.1 Steps of single crystal growth using layering technique (i) Aqueous $\text{Mn}(\text{NO}_3)_2$ solution to be crystallized. (ii) Drop by drop addition of precipitant (a+b) (iii) Left overnight without disturbance (iv) Single crystals form at the interface.

2.2. Experimental techniques

Techniques such as Raman spectroscopy and X-ray diffraction have been employed for characterization and investigations of phase transitions in these systems. Raman measurements on these compounds were performed to explain phonon anharmonicity and interpreted with computational methods.

2.2.1. Raman scattering

Inelastic scattering of light by elementary excitations is termed as Raman scattering. When a beam of light (UV-Visible and IR region) of frequency ω_0 is incident on a solid, most of the light gets scattered elastically, i.e., without change in energy. A small fraction of light is scattered inelastically with frequencies $\omega_0 \pm \omega_v$, where ω_v are the characteristic vibrational frequencies of the solid. The spectral bands with frequencies $\omega_0 - \omega_v$ are called Stokes Raman bands whereas those of $\omega_0 + \omega_v$ are called anti-Stokes. Thus the energy differences between the incident and the Raman scattered photons are equal to the frequencies of lattice vibrations or phonons.

At ambient conditions, the population of phonons in a solid in the ground state is much larger than the first excited vibrational state and hence the Stokes bands are more intense than the anti-Stokes bands.

Quantum theory of Raman scattering

Quantized lattice vibrations are called phonons. There exist several discrete excited states above the ground state corresponding to the different vibrational modes of a solid. When a photon of incident energy $\hbar\omega_0$ and momentum $\hbar k_0$ undergoes inelastic scattering, a phonon of energy $\hbar\omega_p$ and momentum $\hbar q$ is either created or annihilated (Figure 2.2). However, the total energy and momentum before and after scattering is conserved.

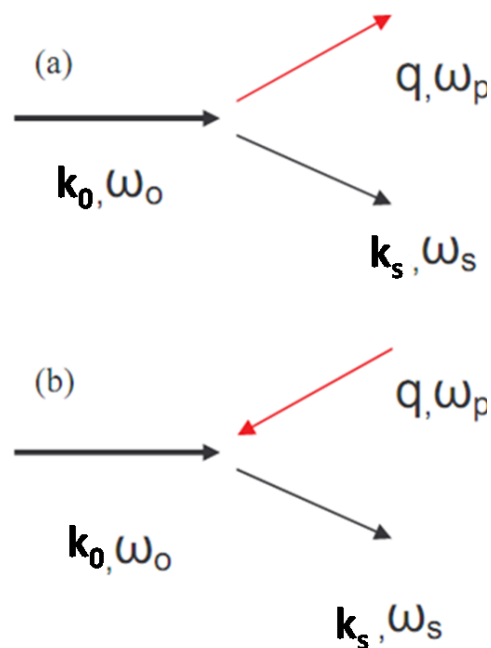


Figure 2.2 Schematic representation of (a) creation (Stokes) and (b) annihilation (anti-Stokes) of phonon (q, ω_p)

During the creation of phonon the lattice goes to a higher excited vibrational state from the ground state by absorbing energy from the incident photon. On the other hand, in phonon annihilation process, lattice returns to the ground state from the vibrationally excited state by releasing energy. The energy and momentum conservation process can be expressed as follows,⁸

$$\hbar\omega_s = \hbar\omega_0 \mp \hbar\omega_p \quad (2.1)$$

$$\hbar k_s = \hbar k_0 \mp \hbar q \quad (2.2)$$

Where + sign indicates a phonon is annihilated (anti-Stokes), and – sign indicates a phonon is created (Stokes). $\hbar\omega_s$ and $\hbar k_s$ are the scattered photon energy and momentum respectively. Anti Stokes scattering depends on the phonon population in the excited state of the material before the light is incident. The probability for anti-Stokes scattering therefore decreases exponentially on lowering the temperature, because of a decrease in the phonon population, whereas Stokes scattering does not require a phonon to be present in the excited state and can therefore occur at any temperature. From a quantum mechanical theory the ratio of Stokes to anti-Stokes scattering events are given by:⁸

$$\frac{I_s}{I_{as}} = \exp\left(\frac{\hbar\omega_p}{k_B T}\right) \quad (2.3)$$

The magnitude of the scattering vector q depends on the scattering angle:^{8,9}

$$|\vec{q}| = |\vec{k}_0 - \vec{k}_s| \quad (2.4)$$

From the vector diagram (Figure 2.2), the expression for the phonon momentum can be given by,^{8,9}

$$|\vec{q}| = 2|\vec{k}_0| \sin \frac{\theta}{2}. \quad (2.5)$$

where θ is the scattering angle. In the backscattering geometry, $|\vec{q}| = 2|\vec{k}_0|$. Hence, the maximum value of q that can be accessed in Raman scattering is of the order 10^5 cm^{-1} . This is very small compared to Brillouin zone boundary in a typical crystal ($\sim 10^8 \text{ cm}^{-1}$) and hence Raman scattering is able to probe phonons only near the zone center.

2.2.2. High pressure Technique

Raman scattering is a powerful probe of solid state excitations in the energy range up to $\sim 400 \text{ meV}$ (wavenumber range $\sim 3\text{-}3200 \text{ cm}^{-1}$). Pressure can cause large changes in the energies and interactions of these excitations within a given solid phase or it can cause transitions to new phases having quite different excitation spectra.

High pressure Raman spectroscopic measurements have been concerned with change in the frequencies of lattice vibrations. These changes show up as spectral shifts of the peak of the Raman bands. If the lifetime of the phonons is affected by pressure (through anharmonic interactions) then in addition to spectral shifts, the observed line shape will also be modified. Compression can also cause a structural phase transition involving a change in the point group symmetry and hence the Raman selection rules will also change. This manifests through the appearance of new features in the observed spectra as forbidden excitations become Raman active and as degeneracies are lifted. The magnitude of allowed Raman tensor components can also be affected by pressure without a phase transition.¹⁰

Phonon frequency shifts are related to pressure by Gruneisen parameter. The Gruneisen parameter γ_i for a quasi-harmonic mode i of frequency of ω_i is defined by

$$\gamma_i = -\frac{\partial \ln \omega_i}{\partial \ln V} = \frac{1}{\chi_T} \frac{\partial \ln \omega_i}{\partial P} \quad (2.6)$$

where χ_T is the isothermal volume compressibility.

There exist numerous ways to compress materials, depending on the magnitude of pressure and the sample size. There are several kinds of large volume presses which can be used for large samples and pressures up to 25 GPa (where 1GPa=10000 bar and 1bar=1 atm. Pressure). The most common pressure apparatus for microscopic samples is the diamond anvil cell (DAC) developed in the 1960s by W. Bassett et al. which uses the simple principle $P = F/A$ (i.e. pressure equals force per unit area) to create high pressure by decreasing the sample area while applying moderate forces.¹¹ The area of the applied force is usually only a few hundred μm^2 , and new developments in diamond cutting techniques have made it possible to reach pressures up to 550 GPa.¹¹ A sketch of the symmetric DAC used in the present experiments is shown in Figure 2.3. At the heart of the DAC are two brilliant-cut diamonds. Diamond is the hardest material known and therefore well suited to apply very high pressures. The table face of the diamond sits on a seat made of tungsten carbide. The size of the culet face (small front of the diamond) defines the pressures that can be reached at a given force, defined by the mechanical setup. The culet faces of both diamonds have to be aligned and oppose each other perfectly without tilting inside DAC.

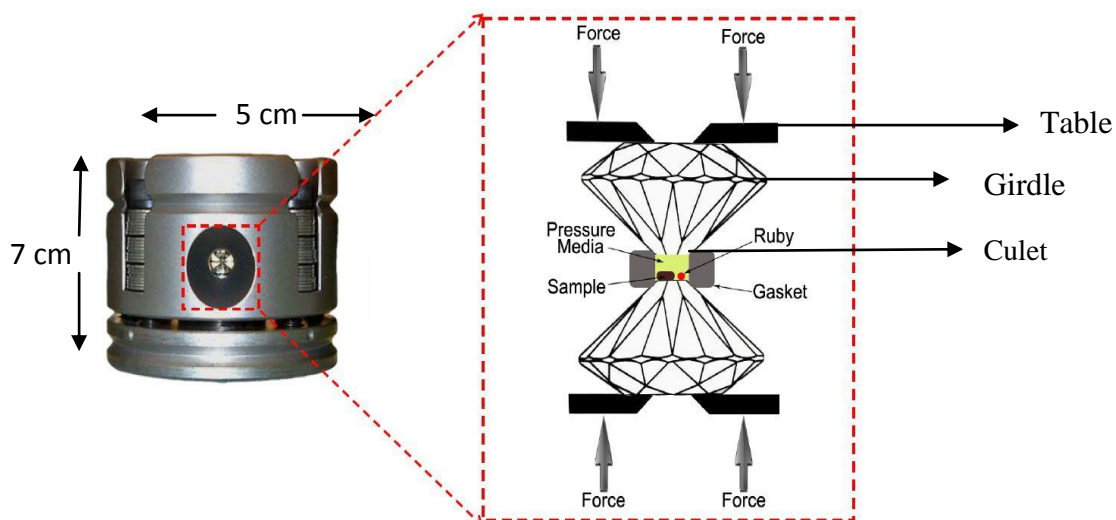


Figure 2.3 Schematic diagram of Symmetric diamond anvil cell.

A thin metal gasket (e.g. hardened stainless steel) with an initial thickness of $250\ \mu\text{m}$ is placed between the two culet faces. Then the diamonds are driven to squeeze the gasket, creating an indented area with thickness of $40\text{-}80\ \mu\text{m}$ at the centre of which a hole is drilled for samples of interest. In this work, the drilled sample chambers ranged between $200\text{-}250\ \mu\text{m}$ in diameter. Then, the sample is placed inside the chamber together with a small speck of ruby pressure calibrant and a mixture of methanol and ethanol (in 4:1 ratio by volume) pressure transmitting medium). The diamond culets are brought close together squeezing the sample chamber by tightening the Belleville screws. The liquid pressure medium then transfers the increased pressure hydrostatically to the sample. The use of natural colourless, low fluorescence diamonds as anvils not only opens the possibility to optically observe the sample with a light microscope but enables also the in-situ application of various analytical techniques, especially Raman spectroscopy and X-ray diffraction. The addition of a small ruby chip, as first suggested by Forman *et al.*,¹² makes it possible to measure the pressure by fluorescence spectroscopy. The transparent diamond allows to focus of a laser onto the ruby chip and to collect the fluorescence signal. For

pressure calibration, the high intensity R_1 -line of ruby is used which is at 694.3 nm at ambient pressure and shifts towards the red side of the visible spectrum with increasing pressure (Figure 2.4).

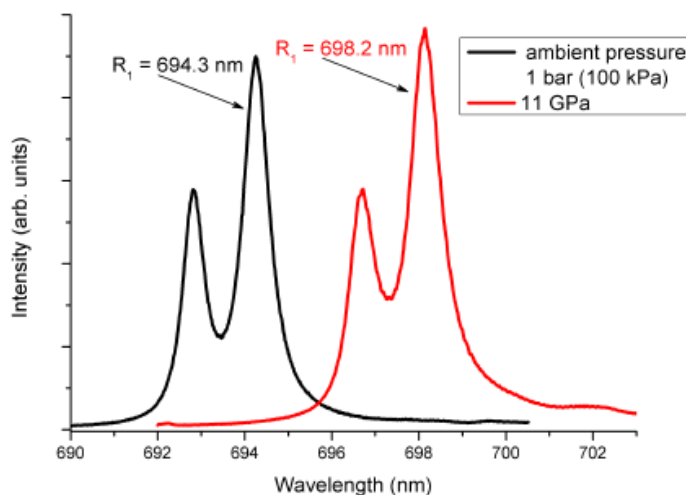


Figure 2.4 Cr^{3+} luminescence in ruby at ambient pressure (black) and at 11 GPa (red).

Furthermore, because ruby is chemically inert, it can be present in the sample chamber without interfering with the experimental specimen.¹³ The fluorescence line shift has been calibrated against the compression of NaCl (measured by x-ray diffraction) to be able to relate the measured shift in wavelength to a certain pressure. The shift of the fluorescence lines is almost linear up to 30 GPa.¹⁴ Mao and Bell¹⁵ calibrated this shift first up to 80 GPa and later to 100 GPa under quasi-hydrostatic conditions and developed the following simple formula with empirical constants $A = 1904$ and $B = 7.665$:

$$P(\text{GPa}) = \frac{A}{B} \left[\left(\frac{\lambda}{\lambda_0} \right)^B - 1 \right] \quad (2.7)$$

Renishaw micro-Raman spectrometer

Figure 2.5 shows a schematic block diagram of the Renishaw Invia micro-Raman spectrometer used in the present studies. It consists of a laser, a system unit, a microscope, a monochromator and a detector that is a charge-coupled device (CCD). The working principle of this spectrometer is described below.

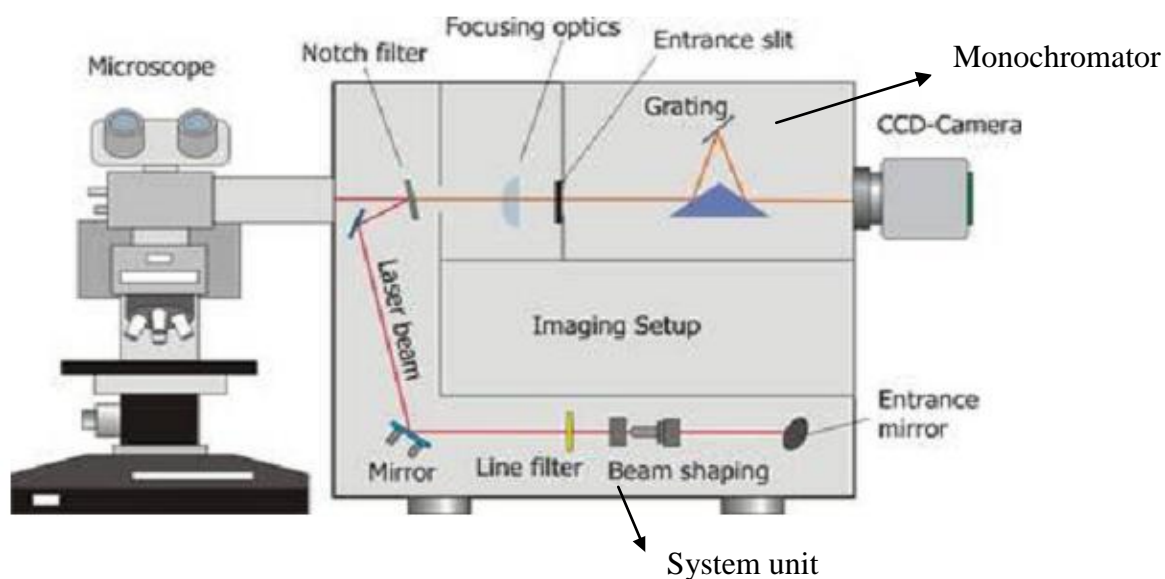


Figure 2.5 Schematic diagram of Renishaw micro-Raman spectrometer

(a) Light source: An Ar^+ laser light of wavelength 514.5 nm has been used as excitation source. The laser unit is mounted behind the system unit. It contains a delivery optics tube consisting of laser attenuation filter wheel and alignment mirror. The filter wheel contains four neutral density filters, which are used to attenuate the power of laser beam. The alignment mirror is used to align and send the laser beam into system unit through delivery optics tube.

(b) System unit: As shown in Figure 2.5, the laser light entering the system unit is focused by beam shaper which converge the beam into a $10\mu\text{m}$ pinhole. A second

movable objective lens is used to make a well collimated beam. Two subsequent mirrors are used to reflect the light onto a mirror contained in holographic filter unit.

(c) Microscope unit: The microscope focuses the laser light into a tight spot and illuminates the sample placed on a mechanical stage. In our Raman setup, an edge filter is used to absorb all wavelengths up to a certain point, and then transmits with high efficiency all wavelengths above this point. As an example, a 514 nm edge filter will absorb all light up to 516 nm (e.g., 70 cm^{-1}) including the laser emission. Above 534 nm it will transmit light, allowing detection of the Raman spectrum (from 70 cm^{-1} to 3200 cm^{-1}). It has a very small transition width below 1% of the laser wavelength, allowing measurements very close to the incident wavelength, gaining information at low Raman shifts.

(d) Monochromator: The scattered light that filters through the Rayleigh filter is passed through a slit and gets dispersed in a single monochromator using a holographic grating with 1800 grooves/mm.

(e) Charge Coupled Device: The CCD detector is a cooled (-70°C), sectoral piece of silicon with a two dimensional array of pixels. The spatially dispersed signal is focussed on CCD where the spectrum is stored as charges. The charge is proportional to the intensity at any given wavenumber and it is read out by electronics. Data acquisition is carried out by a computer using WiRE™ (Windows-based Raman Environment) software. The software allows the user to set the spectral range, accumulation time and laser power. The spectra from 70 cm^{-1} could be measured without losing the signal. The spectrometer resolution for 1800 grooves/mm grating is 1.5 cm^{-1} per CCD pixel. The Raman shift in wave numbers is calibrated using the 520.5 cm^{-1} Raman line from a Si single crystal.

2.2.3. X-ray diffraction

Rotating anode X-ray diffractometer

High pressure X-ray diffraction studies have been carried out using a X-ray diffractometer that employs a RIGAKU rotating anode X-ray generator (UltraX 18) as the source and also using the Indian synchrotron source (described later). The laboratory based XRD machine has a high frequency type 18 kW X-ray generator with Mo as target material. The X-ray beam generated from the Mo target is monochromatized with the help of a graphite monochromator. The wavelength of the X - rays used for the experiments is 0.7107 Å. The overall resolution of the diffractometer is $\delta d/d \sim 0.001$. An image plate based mar345dtb detector is used to detect diffracted X-rays. The sample to detector distance was calibrated using LaB₆. High Pressure measurements were carried out at ambient temperature using a Mao-Bell type DAC with diamonds of 600 µm culet diameter in an angle dispersive mode at several pressures up to ~19 GPa. The powdered sample was loaded along with methanol-ethanol medium and gold powder for pressure calibration into a 200 µm diameter hole drilled in a pre-indented stainless steel gasket. Two dimensional image data from the mar345dtb detector was converted to intensity versus 2θ using *FIT2D*¹⁷ program. The high pressure XRD patterns were indexed with *POWD* program¹⁸ and the lattice parameters refined by least square fitting using AIDS 83 software.

Synchrotron X-ray diffraction

High pressure X-ray diffraction measurements of sodium zirconium phosphate were performed at the angle dispersive adaptation of beam line-11 at the INDUS-2 synchrotron source in the Raja Ramana Centre for Advance Technology (RRCAT) at Indore, India with a beam energy of (26.632±0.005) keV ($\lambda = 0.46575$

Å) and beam dimensions of $200 \times 200 \mu\text{m}$. Energy selection was accomplished by using a monochromator with a Si (1 1 1) single crystal. The beam line comprises water-cooled Be window, 6 mm Cu beam stopper, water-cooled motorized primary slit system, evacuation port, ionization chamber, collection slits mounted over various motorized stages, HPGe detector and a 8-axis motorized goniometric stage with the provision of alignment of the entire experimental station with respect to the synchrotron beam and sample maneuverability in x, y, z, θ and χ directions.¹⁶ Debye-Scherrer rings were recorded with a high purity Germanium (HPGe) detector with an image size of 3450×3450 pixels. The sample to detector distance was 235.2 mm. The diffraction image was integrated into two-dimensional patterns with Fit2D software,¹⁷ and the configuration parameters of the experimental setup were calibrated with a cerium dioxide (CeO_2) standard. XRD patterns were refined by Reitveld method using Fullprof¹⁹ software.

2.3. Computational details

The quantum theory of materials begins with the Hamiltonian of many body systems consisting of interacting electrons and nuclei:

$$\hat{H} = - \sum_i \frac{\hbar^2}{2m_e} \nabla_i^2 - \sum_{I,i} \frac{Z_I e^2}{|r_i - R_I|} + \frac{1}{2} \sum_{i \neq j} \frac{e^2}{|r_i - r_j|} - \sum_I \frac{\hbar^2}{2M_I} \nabla_I^2 + \frac{1}{2} \sum_{I \neq J} \frac{Z_I Z_J e^2}{|R_I - R_J|} \quad (2.8)$$

where the uppercase and lowercase subscripts label the nuclei and electrons respectively, M_I is the nuclear mass, m_e the electronic mass, Z_I the atomic number of ion I and R_I and r_i are the nuclear and electronic positions, respectively.

$$\hat{T}_n = - \sum_I \frac{\hbar^2}{2M_I} \nabla_I^2$$

$$\hat{T}_e = - \sum_i \frac{\hbar^2}{2m_e} \nabla_i^2$$

$$\hat{V}_{n-n} = \frac{1}{2} \sum_{I \neq J} \frac{Z_I Z_J e^2}{|R_I - R_J|}$$

$$\hat{V}_{e-n} = - \frac{1}{2} \sum_{I,i} \frac{Z_I e^2}{|r_{R_i} - R_I|}$$

$$\hat{V}_{e-e} = \frac{1}{2} \sum_{i \neq j} \frac{e^2}{|r_i - r_j|}$$

where T_n and T_e are kinetic energy of nuclei and electrons respectively, V_{n-n} is the Coulombic repulsion energy of the nuclei, V_{e-n} is the Coulombic attraction between electrons and nuclei and V_{e-e} is the electron-electron interaction.

The complexity of above equation is reduced by adiabatic or Born-Oppenheimer approximation according to which the lighter electrons are assumed to be always in their ground state irrespective of the instantaneous configuration of the ions. Hence, the Hamiltonian of the many-electron system (eq. (2.9)) includes the kinetic energy of n electrons, their interaction with the external potential of N ions located at the sites R_I and the interaction of electrons with each other.

$$\hat{H}_e = \hat{T}_e + \hat{V}_{e-e} + \hat{V}_{ext} \quad (2.9)$$

For applications in the field of materials, Density Functional Theory (DFT) is widely used by reducing the many-electron problem to an effective one-electron form.

Density-functional theory (DFT)

Density-functional theory is based on the famous theorem by Hohenberg and Kohn²⁰ who demonstrated that the total energy of a many-electron system in an external potential is a unique functional of the electron density and that this functional has its minimum at the ground state density. Expressing the electron density $n(r)$ as a sum over one-electron densities $|\psi_i(r)|^2$ and using the one electron wave functions as the variational parameters leads to the Kohn-Sham one-electron equations²¹

$$\left[-\frac{\hbar^2}{2m} \frac{\partial^2}{\partial r^2} + V_{el-ion} + e^2 \int \frac{n(r')}{|r-r'|} dr + V_{xc}(r) \right] \psi_i(r) = E_i \psi_i(r) \quad (2.10)$$

$$n(r) = \sum_i^n |\psi_i(r)|^2, V_{xc} = \frac{\delta E_{xc}(r)[n(r)]}{\delta n(r)}$$

Here the first term represents the kinetic energy of non interacting electrons, second term is the external potential acting on the electrons and the third term represents the complex quantum mechanical $e-e$ Coulomb interaction energy. The last term is the exchange correlation potential which has been expressed as the functional derivative of the exchange-correlation energy. The form of E_{xc} is unknown. Numerous approximate schemes have been devised for E_{xc} and implemented to solve the Kohn-Sham equations. Different flavors of DFT typically arise from the approximation used in the representation of the exchange-correlation functional. The simplest of such expressions is Local Density Approximations (LDA)²² where the exchange-correlation energy of a single electron at the position r is equal to the exchange-correlation energy of an electron in a homogenous electron gas of density n_0 equal to the local electron density $n(r)$. The calculated lattice parameters are generally smaller and the approximation does not work well for strongly correlated systems, transition metals, van der Waals interactions, and hydrogen bonds. Generalised Gradient

Approximation (GGA)²³ which includes gradients in electron density is more accurate than LDA and is used widely. A limitation of some of the GGA functionals is that it incorrectly estimates the strength of weak interactions such as hydrogen bond and Van der waals interaction. Van der Waals interactions resulting from dynamical correlations between fluctuating charge distributions are not appropriately described in LDA and GGA functionals. Hence, DFT-D approach²⁴ is used which consists in adding a semi-empirical dispersion potential to the conventional Kohn-Sham DFT energy.

$$E_{DFT-D} = E_{KS-DFT} + E_{disp} \quad (2.11)$$

Basis functions

The wavefunctions $\psi_i(r)$ generally represented as a linear combination of a finite number of basis functions. One of the three basis sets namely, Linear combination of atomic orbital (LCAOs), linearized augmented plane waves (LAPWs) and plane waves (PWs) in combination with Pseudopotentials are employed for complex systems. Among them, plane-wave basis sets offer several advantages like convergence with respect to completeness checked by extending cut-off energy, fast Fourier transforms facilitating the solution of the Poisson equation and direct calculation of forces on atoms and stresses on the unit cell using Hellmann-Feynman theorem without applying Pulay corrections. The wavefunction of the electrons in terms of electrons is written as,

$$\psi_i(r) = \sum_k c_{ik} \exp(ik \cdot r) \quad (2.12)$$

Here, c_{ik} is the list of coefficients and k is the momentum of electron. The coefficients c_{ik} is the list of numbers to be varied. Thus, the ground state energy of a crystal is

calculated by solving eq. (2.10) using these wavefunctions through a self-consistent iterative scheme.

Detailed description of DFT methods based on plane waves and Pseudopotentials can be found in review article by Payne *et al.*²⁵

Hellmann-Feynman Forces

The variational property of the ground state energy has a very important consequence: for a configuration $\{R_I\}$, the force F_I acting on the atom at position R_I is given by the expected value of the derivative of the Hamiltonian H with respect to R_I in the electronic ground state. Hellmann-Feynman form of forces contains the term of energy functional $E(\{R\})$ with respect to atomic positions and the term with derivative of charge density:

$$F_I^{DFT} = - \int (n)r \frac{\partial V_{\{R\}}(r)}{\partial R_I} dr - \frac{\partial E_N(\{R\})}{\partial R_I} - \int \frac{\delta E(\{R\})}{\delta n(r)} \frac{\partial n(r)}{\partial R_I} \quad (2.13)$$

The last term in eq.2.13 vanishes exactly for ground state charge density. Thus the forces in DFT can be calculated from the knowledge of electron charge density.

Density Functional Perturbation Theory (DFPT) or linear response theory

The linear response approach allows calculation of dynamical matrix $D(q)$ and phonon frequencies at a selected set of q -points. It is based essentially on the computation of the derivative of the total energy with respect to perturbations, such as atomic displacements through Hellmann-Feynman theorem.

$$\frac{\partial^2 E(\{R\})}{\partial R_I \partial R_J} = \int \frac{\partial n(r)}{\partial R_J} \frac{\partial V_{\{R\}}(r)}{\partial R_I} dr + \delta_{IJ} \int n(r) \frac{\partial^2 V_{\{R\}}(r)}{\partial R_I \partial R_J} dr + \frac{\partial^2 E_N(\{R\})}{\partial R_I \partial R_J} \quad (2.14)$$

The calculation of the interatomic force constants (IFCs) thus requires the knowledge of the ground state charge density $n(r)$ as well as of its linear response to distortion of the nuclear geometry $\frac{\partial n(r)}{\partial R_J}$. The dynamical matrix is the Fourier transform of real-space IFCs. The eigen vectors and their associated phonon frequencies are calculated by diagonalizing the dynamical matrix. In this thesis, DFPT is used for lattice dynamics calculation.

DFT Codes

In this thesis, Vienna Ab initio Simulation Package (VASP),²⁶ is used for the calculation of equation of state, elastic constants, phonon spectra and thermal properties. To obtain phonon dispersion and mode assignments, PHONOPY²⁷ interfaced with VASP is used.

2.4. References

- ¹J. Cernak, M. Orendac, I. Potonak, J. Chomic, A. Orendacova, J. Skorsepa and A. Feher, *Coord. Chem. Rev.* **224**, 51 (2002).
- ²M. Obha and H. Okawa, *Coord. Chem. Rev.* **198**, 313 (2000).
- ³S. R. Batten and K. S. Murray, *Coord. Chem. Rev.* **206**, 103 (2003).
- ⁴R. S. Krishnan, R. Srinivasan and S. Devanarayanan, *Thermal Expansion of Crystals*, Pergamon Press, Oxford (1979).
- ⁵J. F. Shackelford, W. Alexander and J. S. Park, *C. R. C. Practical Handbook of Materials Selection*, CRC Press, Boca Raton (1975).
- ⁶D. K. Agarwal and J. H. Adair, *J. Am. Ceram. Soc.* **73**, 2153 (1990).
- ⁷J. Hope, *J. Appl. Cryst.* **4**, 333 (1971).
- ⁸M. Fox, *Optical properties of Solid*, Oxford University Press, New York, 2001.
- ⁹N. W. Ashcroft and N. D. Mermin, *Solid State Physics* (Holt, Rhinehart, Winston, New York, 1976).
- ¹⁰M. Cardona, *Light Scattering in Solids* (Springer-Verlag, Berlin, 1975).
- ¹¹W. A. Basset, *High Press. Research* **29**, 163 (2009).
- ¹²R.A. Forman, G.J. Piermarini, J.D. Barnett, and S. Block, *Science* **176**, 248 (1972).
- ¹³G.J. Piermarini, S. Block, J.D. Barnett, and R.A. Forman, *J. Appl. Phys.* **46**, 2774, (1975).
- ¹⁴H.K. Mao, J. Xu, and P.M. Bell, *J. Geophys. Res.* **91**, 4673 (1968).
- ¹⁵H.K. Mao, P.M. Bell, J.W. Shaner, and D. J. Steinberg. *J. Appl. Phys.* **49**, 3276, (1978).
- ¹⁶K. K. Pandey, H. K. Poswal, A. K. Mishra, A. Dwivedi, R. Vasanthi, N. Garg and S. M. Sharma, *Pramana J. Phys.* **80**, 4607 (2013).

- ¹⁷A. P. Hammersley, S. O. Svensson, M. Hanfland, A. N. Fitch and D. Hauserman, *High Pressure Res.* **14**, 235 (1996).
- ¹⁸E. Wu, *J. Appl. Cryst.* **22**, 506 (1989).
- ¹⁹J. Roisnel and J. Rodriguez-carvajal, *Material Science Forum* **378**, 118 (2001).
- ²⁰P. Hohenberg and W. Kohn, *Phys. Rev. B* **136**, 864 (1964).
- ²¹W. Kohn and L. J. Sham, *Phys. Rev. A* **140**, 1133 (1965).
- ²²J. P. Perdew and A. Zunger, *Phys. Rev. B* **23**, 5075 (1981).
- ²³J. P. Perdew, *Phys. Rev. B* **33**, 8822 (1986).
- ²⁴J. Klimes, D. R. Bowler and A. Michaelides, *Phys. Rev. B* **83**, 195131 (2011).
- ²⁵M.C. Payne, M. P. Teter, D. C. Allan, T. A. Arias, and J. D. Joannopoulos, *Rev. Mod. Phys.* **64**, 1045 (1992).
- ²⁶X. Gonze and C. Lee, *Phys. Rev. B* **55**, 10355 (1997).
- ²⁷A. Togo, F. Oba, and I. Tanaka, *Phys. Rev. B* **78**, 134106 (2008).

Chapter-3

Anharmonic phonons of sodium zirconium phosphate studied by high pressure Raman spectroscopy, X-ray diffraction and first principles calculations

3.1 Introduction

$\text{NaZr}_2(\text{PO}_4)_3$ (NZP) is the prototype of a broad family of compounds with three dimensional skeletal framework of the form $[\text{A}_{2n}(\text{XO}_4)_{3n}]^m$ that renders the structure highly stable and flexible.¹ NZP exhibits anisotropic thermal expansion, with $\alpha_c = 23.5 \times 10^{-6} \text{K}^{-1}$ and $\alpha_a = -5 \times 10^{-6} \text{K}^{-1}$, with an overall low positive thermal expansion coefficient of the order $\alpha_{av} = 4.5 \times 10^{-6} \text{K}^{-1}$ from 293-1273 K.² Dilatometric measurements on a ceramic bar however result in a negative bulk thermal expansion coefficient $\alpha_{av} = -0.4 \times 10^{-6} \text{K}^{-1}$ over the temperature range of 298-773 K.³ High temperature x-ray diffraction studies and differential thermal analysis on NZP showed the absence of phase transitions up to 1073 K and 898 K respectively.^{4,5} The apparent (bulk) values of the thermal expansion coefficient, in general, are lower than the intrinsic values determined from x-ray diffraction since part of the expansion could take place in micro cracks in the material.⁶

Thermal expansion in solids arises from anharmonic lattice vibrations. Change in phonon frequency as a function of temperature is due to two contributions that could be decoupled: a quasiharmonic contribution due to change in lattice volume – also known as the ‘implicit contribution’, and the other, purely anharmonic (explicit) contribution due to change in vibrational amplitude.⁷ A temperature

dependent Raman study at ambient pressure and a high pressure Raman study at ambient temperature help us separate these two contributions.

High pressure x-ray diffraction studies on an isostructural compound $\text{RbTi}_2(\text{PO}_4)_3$ has revealed a subtle phase transformation from $R-3c$ to $R3$ structure accompanied by a huge reduction in the bulk modulus from 104 to 60 GPa at a pressure of 1.7 GPa,⁸ and the structure remains intact up to 6.2 GPa. However, there are no reports of high pressure investigations of NZP in the literature.

The purpose of the current study is twofold: To investigate the contribution of the various phonon modes to the thermal expansion of NZP through experiments and *ab-initio* calculations, and to investigate the structural stability of NZP at high pressures. Raman spectroscopic studies as a function of pressure at ambient temperature and as a function of temperature at ambient pressure were performed to identify the anharmonic phonons. High-pressure x-ray diffraction measurements were carried out to determine the structural stability of NZP and its equation of state. To complement the Raman and XRD studies, the phonon dispersion and bulk modulus were computed via DFT calculations. The P - V equation of state, phonon dispersion and the characters of irreducible representation were computed using VASP and Phonopy. The thermal expansion coefficient was calculated from Gruneisen parameters of all phonons and compared with the reported value.

3.2. Experimental and computational details

$\text{NaZr}_2(\text{PO}_4)_3$ was synthesized by mixing stoichiometric amounts of precursor solutions of 1 M NaCl, 1.5 M ZrOCl_2 and 6 M H_3PO_4 following the procedure of Agarwal and Adair.⁹ This viscous slurry was heated at 70 °C for 24 hrs. The resulting gel was dried at 150 C for 4 hrs and ground, calcined at 700 °C for 16 hrs,

then finally heat treated at 1100 °C for 24 hrs. The final product is fine white polycrystalline powder whose XRD pattern matched with the JCPDS pattern [PDF NO: 33-1312] without any impurity peaks.

In situ high pressure Raman spectra were recorded up to ~20 GPa from a symmetric diamond anvil cell (DAC) with diamonds of culet diameter 500 μm , using a micro Raman spectrometer (Renishaw, UK, model Invia) with 514 nm laser excitation. The sample was loaded along with ruby pressure calibrant and a 4:1 mixture of methanol-ethanol medium into a 200 μm hole drilled into a pre-indented stainless steel gasket. The spectra were recorded in both increasing and decreasing pressure cycles. Temperature dependent Raman measurements from 80 to 860 K were carried out using a heating and cooling microscope stage (Linkam THMS 600).

High Pressure X Ray Diffraction experiments were carried out at ambient temperature using a Mao-Bell type DAC with diamonds of 600 μm culet diameter in an angle dispersive mode at several pressures up to ~19 GPa. The powdered sample was loaded along with methanol-ethanol medium and gold powder for pressure calibration into a 200 μm diameter hole drilled in a stainless steel gasket. Mo K_{α} x-ray beam was incident from a Rigaku ULTRAX (18 kW) rotating anode x-ray generator with a graphite monochromator. The overall resolution of the diffractometer is $\delta d/d \sim 0.001$. An image plate based mardtb345 diffractometer was used. The sample to detector distance was calibrated using a standard LaB_6 specimen. Two dimensional image data from the Mar345IP detector was converted to intensity versus 2θ using *FIT2D* program. The high pressure XRD patterns were indexed with *POWD* program¹⁰ and the lattice parameter refined by least square fitting using AIDS 83 software.

Angle dispersive x-ray diffraction experiments at high pressure were carried out at the angle dispersive adaptation of beamline -11 at the INDUS-2 synchrotron source (RRCAT, Indore)¹¹ with monochromatic X-rays of wavelength 0.46575 Å and beam dimensions of 200 × 200 μm. NZP was loaded in a 250 μm diameter hole in a tungsten gasket in the symmetric diamond anvil cell. Diffraction patterns were recorded using a mar345 imaging plate detector kept at a distance of ~235 mm from the sample which was calibrated using CeO₂ specimen. Pressure was determined from the equation of state of silver¹²⁻¹³ that was loaded along with the sample. 4:1 methanol/ethanol mixture was used as the pressure transmitting medium. The diffraction intensity was normalized to constant exposure time for the purpose of analysis of diffraction pattern. The two dimensional diffraction images were radially integrated using the FIT2D software¹⁴. High pressure phases were indexed with POWD¹⁰. Further refinement was performed using Fullprof software¹⁵ up to 6 GPa.

Theoretical calculation of phonon spectrum was carried out using VASP (Vienna *ab initio* simulation package).¹⁶⁻¹⁸ VASP performs an iterative solution of the Kohn-Sham equations in a plane wave basis. First, full structural relaxations of the 36 atom rhombohedral primitive unit cell of NaZr₂(PO₄)₃ (space group R-3c (167))¹⁹ were carried out. The interaction of valence electrons with ionic cores is represented by the ultrasoft pseudopotentials.²⁰ Electronic exchange and correlation are described by the gradient-corrected PW91 functional.²¹ Plane wave cut-off-energy of 500eV was used. Brillouin-zone integrations were performed on 7×7×7 gamma-centered Monkhorst-Pack²² grid, with Gaussian smearing width $\sigma = 0.05$. Ionic relaxation was stopped when all forces are smaller than 1×10^{-6} eV/Å. Next, with the equilibrium geometry obtained from the first step, VASP was restarted with DFPT (Density Functional Perturbation Theory)²³⁻²⁴ flag turned ON (IBRION=8) and

the response function calculations were carried out in order to obtain the first derivatives of the occupied wave functions with respect to the perturbations of atomic displacements. This is then used to compute the force-constant Hessian matrix, the elementary second derivative response-function tensors.²⁵⁻²⁶ Using DFPT, VASP determines the Hessian matrix for wave vector $q=0$ and computes zone centered phonon frequencies and eigenvectors. For computing the phonon spectrum over the entire Brillouin zone, Phonopy program²⁷ was used. Phonopy reads Hessian matrix of VASP calculation and interpolates over the first Brillouin zone for the specified q -grid. To verify the convergence of the DFPT calculations we have also computed the phonon spectrum of NZP with a 108 atom hexagonal close packed unit cell and found that the zone center phonon modes varied by only a few THz. Visual representations of the different phonon modes were obtained by plotting the eigen vectors of displacement of the various atoms in the unit cell using the VESTA visualization software.²⁸

3.3. Results and discussion

$\text{NaZr}_2(\text{PO}_4)_3$ crystallizes in a rhombohedral structure with space group $R-3c$. The hexagonal unit cell contains six formula units. The Na, Zr, P and O atoms occupy Wyckoff b, c, e and f sites respectively¹⁹. Rietveld refinement was carried out on the powder XRD data collected at ambient conditions using Fullprof software. $R-3c$ structure resulted in a good fit (Figure 3.1) with an R_p value of 16.5%, starting from a model proposed by Hagman *et al.*¹⁹. Refined atomic coordinates are listed in Table 3.1. Converged lattice parameters of hexagonal unit cell ($a = 8.7970(1) \text{ \AA}$, $c = 22.7367(7) \text{ \AA}$) compare well with the reported values¹⁹.

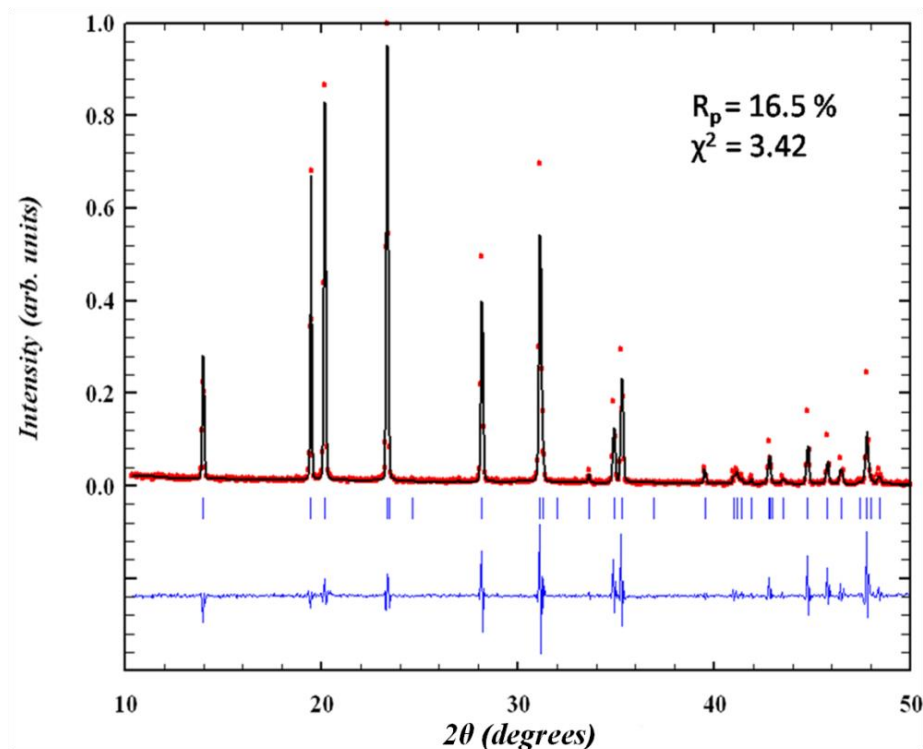


Figure 3.1 Rietveld refinement of ambient pressure X-ray diffraction data for NZP. Red points are experimental data, continuous line represents the fitted data and the bottom curve is the difference plot.

Table 3.1 Structural parameters of NZP at ambient conditions showing fractional coordinates and the isotropic atomic displacement from Reitveld refinement of powder diffraction data. The lattice parameters are $a=b=8.799(1)\text{\AA}$ and $c=22.7408(6)\text{\AA}$ (hexagonal notation). The R factor $R_p=16.5\%$ and the reduced $\chi^2=3.42$.

Name	Site	x	y	z	U_{iso}
Na	2b	0	0	0	2.25
Zr	4c	0	0	0.1455(7)	1.27
P	6e	0.2907(7)	0	0.25	2.15
O1	12f	0.190(6)	0.168(8)	0.088(3)	0.24
O2	12f	0.018(9)	0.2003(5)	0.195(5)	0.24

3.3.1. Raman spectroscopic and computational studies

$\text{NaZr}_2(\text{PO}_4)_3$ crystallizes in a rhombohedral structure with space group $R\bar{3}c$ (D_{3d}^6) with six formula units in the crystallographic unit cell.¹⁹ The two formula units in the primitive cell give rise to 108 degrees of freedom. We carried out Factor group analysis by ‘Correlation method’ of Halford and Hornig.³² resulting in the irreducible representation $\Gamma_{\text{Total}}=8A_{1g}+9A_{2g}+17E_g+9A_{1u}+10A_{2u}+19E_u$. This can be further classified into internal modes of phosphate ions and lattice modes:

$$\Gamma_{\text{Int}}=5A_{1g}+4A_{2g}+9E_g+5A_{1u}+4A_{2u}+9E_u \quad (\text{with} \quad \nu_1=A_{1g}+E_g+A_{1u}+E_u;$$

$$\nu_2=2A_{1g}+2E_g+2A_{1u}+2E_u; \quad \nu_3 \quad \text{and} \quad \nu_4=A_{1g}+2A_{2g}+3E_g+A_{1u}+2A_{2u}+3E_u);$$

$$\Gamma_{\text{Ext}}=3A_{1g}+5A_{2g}+8E_g+4A_{1u}+6A_{2u}+10E_u \quad (24 \text{ translational modes: } \Gamma(\text{Na})^{\text{Trans}} =$$

$$A_{1u}+A_{2u}+2E_u; \quad \Gamma(\text{Zr})^{\text{Trans}} = A_{1g}+A_{2g}+A_{1u}+A_{2u}+2E_g+2E_u; \quad \Gamma(\text{PO}_4)^{\text{Trans}} =$$

$$A_{1g}+A_{1u}+3E_g+3E_u+2A_{2g}+2A_{2u} \quad \text{and} \quad 12 \text{ librational modes } \Gamma(\text{PO}_4)^{\text{Libr}} =$$

$$A_{1g}+A_{1u}+3E_g+3E_u+2A_{2g}+2A_{2u}); \quad \Gamma_{\text{Acoustic}}=A_{2u}+E_u; \quad A_{2g} \text{ and } A_{1u} \text{ modes are optically}$$

inactive. So, there are totally 25 Raman active modes ($8A_{1g}$ and $17E_g$) and 27 IR active modes ($9A_{2u}$ and $18E_u$) expected.

The Raman spectrum of NZP at ambient conditions exhibits 17 distinct Raman bands (Figure 3.2 and Table 3.2), similar to that reported earlier.³³ Observation of less number of modes could be due to accidental degeneracies or insufficient intensities arising from small polarisabilities of some of the modes. Raman bands in the range $325\text{-}1084 \text{ cm}^{-1}$ arise from the internal vibrations of the phosphate ions, and one expects the most intense band at 1026 cm^{-1} to be the symmetric stretch mode. Lattice modes below 270 cm^{-1} arise from the translations of the Zr and the translations and librations of the PO_4 ions.^{33,34}

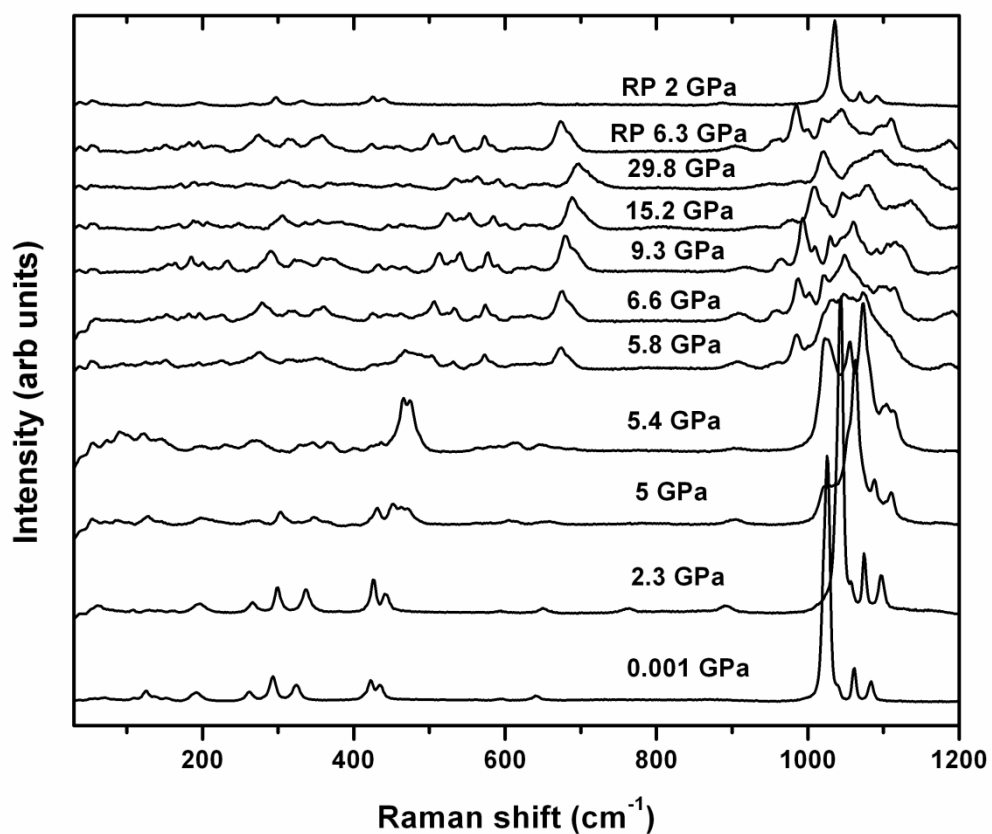


Figure 3.2 Raman spectra of NZP for selected pressures up to 30 GPa which clearly indicates phase transitions around 5 and 5.8 GPa. On decompression, it regains original phase showing reversible transition.

Table 3.2 Frequencies and mode Gruneisen parameters (γ_i) of Raman modes of NZP from experiments and simulations. Mode assignments were obtained from the VASP computed eigen vectors using the Phonopy program.

Experimental		DFPT		Mode
ω (cm ⁻¹)	γ_i	ω (cm ⁻¹)	γ_i	Assignments
72	-2.26	113	-2.61	E _g
112	-0.64	127	5.08	E _g
126	0.19	141	2.74	A _{1g}
139	0.59	157	1.08	E _g
154	0.85	166	2.23	E _g
192	0.43	185	4.31	A _{1g}
262	0.24	273	0.39	E _g
293	0.30	298	1.60	A _{1g}
325	0.66	337	0.50	E _g
422	0.12	425	0.37	E _g
435	0.32	431	0.62	A _{1g}
595	0.15	577	0.18	A _{1g}
642	0.24	623	0.20	E _g
1026	0.19	927	0.60	E _g
1040	0.29	947	0.62	A _{1g}
1061	0.22	991	0.43	E _g
1081	0.18	1018	0.25	A _{1g}

In the absence of polarized Raman measurements on single crystals, *ab-initio* calculations have emerged as an alternative to carry out mode assignments of NZP. Eigen frequencies for the various modes were obtained by diagonalizing the dynamical matrix. The computed phonon dispersion at equilibrium volume (528.66 \AA^3) is shown in Figure 3.3.

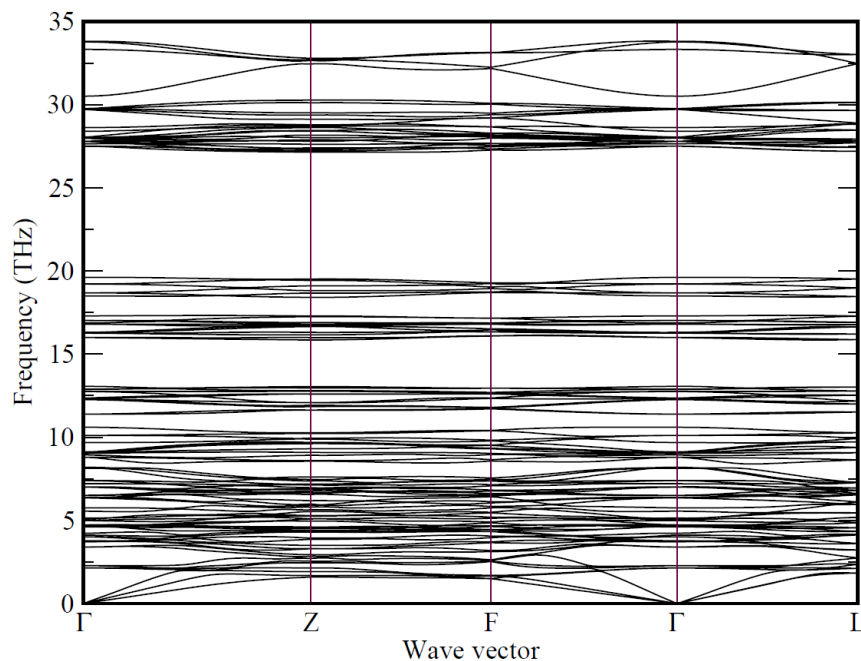


Figure 3.3 Phonon dispersion curves from simulations using VASP code on a 36 atom rhombohedral primitive unit cell of $\text{NaZr}_2(\text{PO}_4)_3$. The E_g zone centre phonon frequencies exhibit good matching with experimental Raman values.

The zone-centre phonon frequencies are compared with experimental values in Table 3.2. The total irreducible representation obtained from computations is consistent with the results of group theoretical analysis detailed above. Mode assignments were obtained from the VASP computed eigen vectors using the Phonopy program, and Raman mode frequencies closest to the computed values were assigned the corresponding symmetry species, excluding the Raman inactive mode A_{2g} . The two lowest energy optical modes are found to be E_u (infrared active) modes at 71 and 76 cm^{-1} , and the first E_g band is at 113 cm^{-1} , the corresponding experimental

value of Raman shift being 72 cm^{-1} (see later). We find closer matching of computed and experimental values for several other modes except the ν_1 and ν_3 internal modes of PO_4 above 1000 cm^{-1} . It turns out that the E_g band at 72 cm^{-1} (experimental) is highly anharmonic (see later). The difference between the experimental and computed mode frequencies for this mode could be due to the harmonic potentials inherent in our lattice dynamic calculations. In order to see if better matching with experimental frequencies could be obtained, we also carried out calculations using projector augmented-wave (PAW) pseudopotential; the corresponding zone center E_g mode frequency was obtained to be 81 cm^{-1} that is closer to the experimental value of 72 cm^{-1} , but when the PAW based dynamical matrix was employed to compute the phonon frequencies over the entire Brillouin zone, negative frequencies (that are unphysical) were obtained over the $F-\Gamma$ segment. Therefore we worked with ultrasoft pseudopotentials that eliminated unphysical frequencies, though it resulted in poorer matching with the $72 \text{ cm}^{-1} E_g$ band.

Atomic displacement plots of the lowest energy (IR active E_u) modes at 71 and 76 cm^{-1} using the VESTA program reveal them to be translational modes of Na atoms. Figure 3.4 shows the displacement vectors for the two lowest energy Raman modes and two of the internal modes of the PO_4 ion: The E_g mode at 113 cm^{-1} (Figure 3.4(a)) is seen to be a combination of the PO_4 librations and Zr translations that contribute negatively to thermal expansion – consistent with the present experimental and computational results (Table 3.2) and similar to the role played by WO_4 in $\text{Zr}(\text{WO}_4)_2$ and the $\text{C}\equiv\text{N}$ in $\text{Zn}(\text{CN})_2$.^{35, 36} The E_g mode at 127 cm^{-1} (Figure 3.4(b)) seems to exhibit coupled rotation of PO_4 tetrahedra and ZrO_6 octahedra. The mode Gruneisen parameter of this mode is experimentally determined to be negative (Table 3.2).

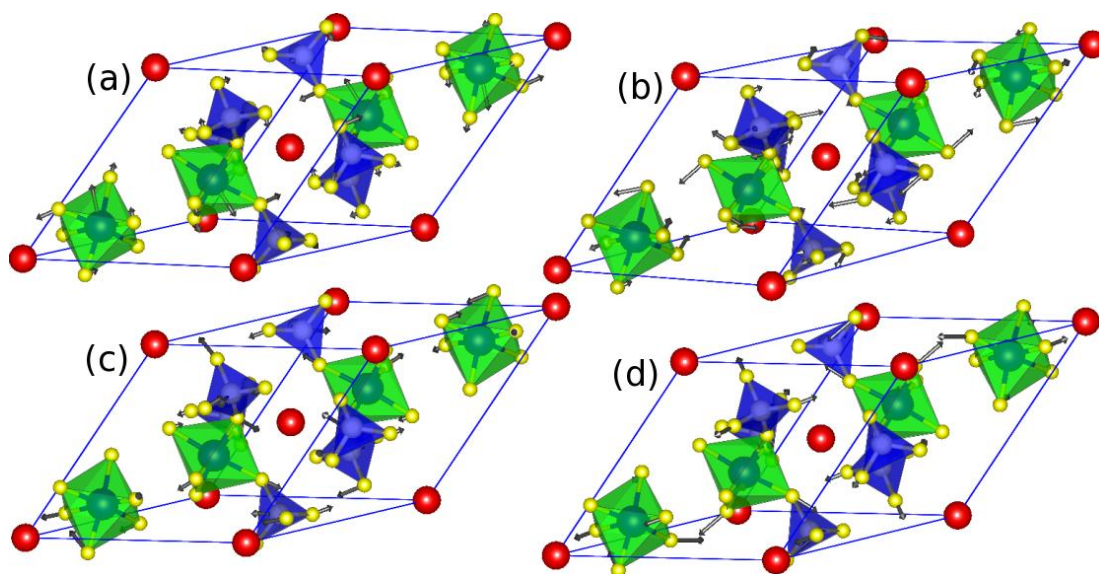


Figure 3.4 Atomic displacements of (a) the 113 cm^{-1} mode showing a combination of the PO_4 librations and Zr translations; (b) the 127 cm^{-1} mode exhibiting coupled rotation of PO_4 tetrahedra and ZrO_6 octahedra; (c) the asymmetric stretch mode of PO_4 at 927 cm^{-1} corresponding to the most intense Raman band at 1026 cm^{-1} and (d) symmetric stretch mode of PO_4 at 991 cm^{-1} corresponding to the Raman band at 1061 cm^{-1} .

The PO_4 ion's internal mode at 927 cm^{-1} corresponding to the most intense Raman band at 1026 cm^{-1} (Figure 3.4(c)) is found to be an asymmetric stretch mode, consistent with the assignment (ν_3) of Barj *et al.*³³. Another internal mode at 991 cm^{-1} corresponding to the Raman band at 1061 cm^{-1} (Figure 3.4(d)) exhibits symmetric stretch of two of the six PO_4 tetrahedra in the unit cell. This could be assigned as the ν_1 mode, contrary to the assignment by Barj *et al.*³³

Figure 3.2 shows Raman spectra of NZP at different pressures. Bands below 150 cm^{-1} correspond to lattice modes; bending modes of PO_4 units appear around 600 cm^{-1} , and above 1000 cm^{-1} stretching modes of PO_4 units exhibit themselves. It is seen that, the low energy bands at 72 cm^{-1} and 112 cm^{-1} which arise from PO_4 libration and Zr translation soften with increasing pressure. As the pressure is increased to above 5 GPa, intensities of the bands at 127, 303 and 433 cm^{-1} decrease

and new broad bands appear below 500 cm^{-1} with splitting of internal modes around 1000 cm^{-1} indicating a phase transition to a structure of a lower symmetry (Phase II) which is indexed below using high pressure X-Ray diffraction as $R3 (C_3^4)$ space group. With two formula units per primitive cell, group theoretical analysis of this phase II using correlation method³² results in 70 Raman active modes distributed as $\Gamma_{\text{Optical}} = 35A + 35E$. Total irreducible representation including acoustic modes is given by $\Gamma_{\text{Total}} = 36A + 36E$. This comprises of internal modes of phosphate unit $\Gamma_{\text{Int}} = 18A + 18E$, $\Gamma(\text{PO}_4)^{\text{Trans,Lib}} = 12A + 12E$ and lattice modes $\Gamma_{\text{ext}} = 6A + 6E$.

In KTiPO_5 framework structure, a first order phase transition was reported to be due to the softening of a phonon band at 56 cm^{-1} associated with potassium atom³⁷. Our DFT calculation on NZP revealed that two E_u (IR) modes with Na translations show usual hardening behavior²⁹. Two soft modes (72 and 112 cm^{-1}) which show Zr displacements and PO_4 librations respectively suggest phase transition by a polyhedral Zr-O-P tilt mechanism. Such a mechanism was reported by high pressure x-ray diffraction studies of $\text{RbTi}_2(\text{PO}_4)_3$ where there was a reduction of Ti-O-P angles with concomitant collapse of alkali sites⁸. Thus these modes can be directly related to the structural instability and phase transformation. The coexistence of phases I and II is evident at 5 GPa from the presence of the bands at 301, 430, 1089 and 1105 cm^{-1} . New bands around 60, 105, 125 and 190 cm^{-1} at 5 GPa corresponding to the $R3$ phase show a red shift with increasing pressure up to 5.8 GPa. The softening of these low energy phonon modes indicates an increase in negative contribution to overall thermal expansion due to the associated negative Gruneisen parameters. Softening of such low energy vibrations has been observed in the well known NTE material, $\text{Zr}(\text{WO}_4)_2$ at ambient pressure.³⁵ This increase in the number of vibrational modes with negative Gruneisen parameter could lead to an enhancement of NTE coefficient above 5 GPa.

A recent study on $\text{Zn}(\text{CN})_2$ reveals such a pressure enhancement of NTE and pressure induced framework softening up to 0.6 GPa³⁸. In case of framework compounds, compression principally leads to increased variation of bond angle³⁰ which enhances bending flexibility of Zr-O-P moiety with only minor contribution from compression of the stiff polyhedral bonds.

On further compression, several new broad modes appear in the low frequency region with sharp increase in intensities around 275 and 674 cm^{-1} . Broadening of Raman bands in the range $\sim 300\text{--}1100 \text{ cm}^{-1}$ signals distortion of PO_4 tetrahedra. Splitting of sharp bands corresponding to internal modes of PO_4 unit indicate phase transition towards a lower symmetry (Phase III). Phase coexistence was observed at 5.8 GPa and gradually modes corresponding to Phase III increase in intensity with rise in pressure. A plot of mode frequency *vs.* pressure (Figure 3.5) clearly indicates all three phase transitions. The frequencies of all modes in this Phase III increase with pressure, indicating a normal positive thermal expansion behavior. Phase III remains stable up to 30 GPa, the highest pressure up to which Raman measurements were carried out.

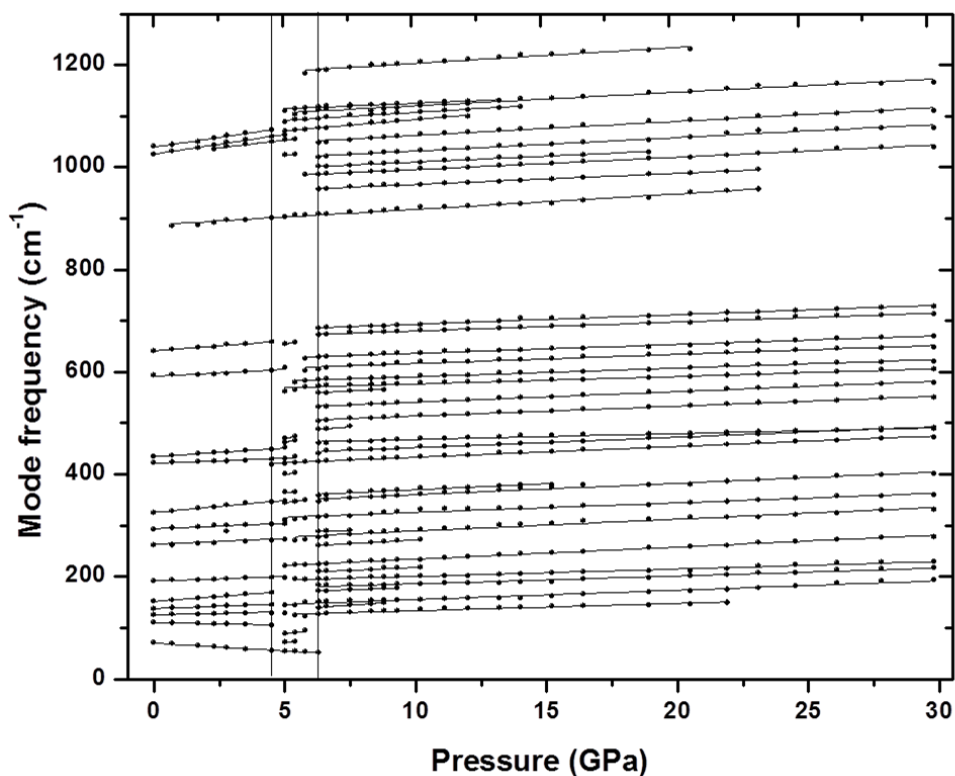


Figure 3.5 ω vs. P of NZP. Changes in the spectral frequencies are clearly seen at 5.5 GPa, signifying a phase transformation that is confirmed from XRD measurements.

It is also found that the two transitions are found to be reversible: spectra were recorded at ten different pressures in the decreasing pressure cycle, and the phase I is recovered with negligible hysteresis (Figure 3.5). Table 3.2 lists the mode frequencies (ω_i) and the corresponding Gruneisen parameters ($\gamma_i = \left(\frac{B_0}{\omega_i}\right)\left(\frac{d\omega_i}{dP}\right)$), where B_0 is the bulk modulus obtained from high pressure XRD measurements described later. Gruneisen parameters for several internal modes are significantly positive which indicates that these modes contribute positively to thermal expansion (PTE). Negative contribution to thermal expansion is by the two low frequency modes at 72 and 112 cm^{-1} that correspond to librations of PO_4 tetrahedra and Zr translation respectively,³⁴ reminiscent of other NTE systems such as $\text{Zr}(\text{WO}_4)_2$ and $\text{Zn}(\text{CN})_2$.^{35, 36}

Phonon spectrum was also computed at a higher pressure of 2.65 GPa ($V=512.96 \text{ \AA}^3$) after reoptimizing the ionic positions. The Γ -point phonon frequencies at this volume and the equilibrium volume were employed to obtain the mode Gruneisen parameters using the expression $\gamma_i = \frac{V_{eq} \Delta\omega_i}{\omega_i \Delta V}$. γ_i for all 70 optical modes except the lowest energy Raman active E_g band ($\omega_{\text{calculated}}=113 \text{ cm}^{-1}$, $\omega_{\text{experimental}}=72 \text{ cm}^{-1}$) mentioned above are positive, whereas experimentally the next higher energy E_g mode ($\omega_{\text{calculated}}=124 \text{ cm}^{-1}$, $\omega_{\text{experimental}}=112 \text{ cm}^{-1}$) also is found to be negative. The close matching of γ_i for this mode is fortuitous, considering the extent of mismatch for other modes. Table 3.1 shows a comparison of the computed and experimental mode Gruneisen parameters for the 17 observed Raman modes. Using Einstein's specific heat $C_i = R[x_i^2 \exp(x_i)]/[\exp(x_i) - 1]^2$, where $x_i = \frac{\hbar\omega_i}{k_B T}$, for the various modes ($i=1$ to 70) the total specific heat C_V was obtained. Here R is the universal gas constant. Thermal expansion coefficient $\alpha = \frac{\gamma_{av} C_V}{3V_m B_0}$, where $\gamma_{av} = \frac{1}{2} \sum p_i C_i \gamma_i / C_V$, p_i are the degeneracies of the respective ω_i phonon branches at the Brillouin zone centre, V_m is the molar volume. The bulk modulus and its pressure coefficients ($B_0=45 \text{ GPa}$ and $B' = 8$) was computed by fitting the DFT calculated energy vs. volume data to the Vinet universal equation of state.⁴⁵ The equilibrium volume V_m is determined to be $3.2 \times 10^{-4} \text{ m}^3/\text{mole}$, and the calculated value of $\alpha = 7.5 \times 10^{-6} \text{ K}^{-1}$ is in good agreement with the reported value of $4.5 \times 10^{-6}/\text{K}$.

Figure 3.6 shows the Raman spectra of NZP at different temperatures over the complete range of phonon frequencies. Frequencies of most of the modes decrease as a function of temperature, but the modes at 72 and 112 cm^{-1} exhibit opposite behavior.

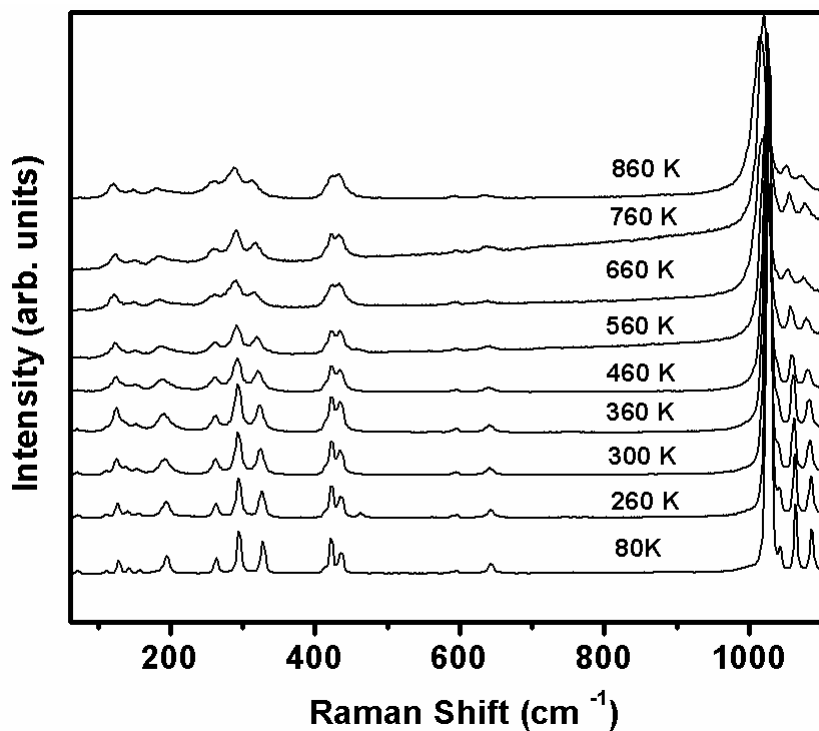


Figure 3.6 Raman spectra of NZP at different temperatures. The compound is stable in the entire temperature range from 80 K to 860 K.

No discontinuous changes are noted, indicating the absence of any phase transition that also agrees with high temperature XRD results.⁴ $d\omega_i/dT$ of the various phonon frequencies were obtained by linear fits to ω vs. T (Figure 3.7).

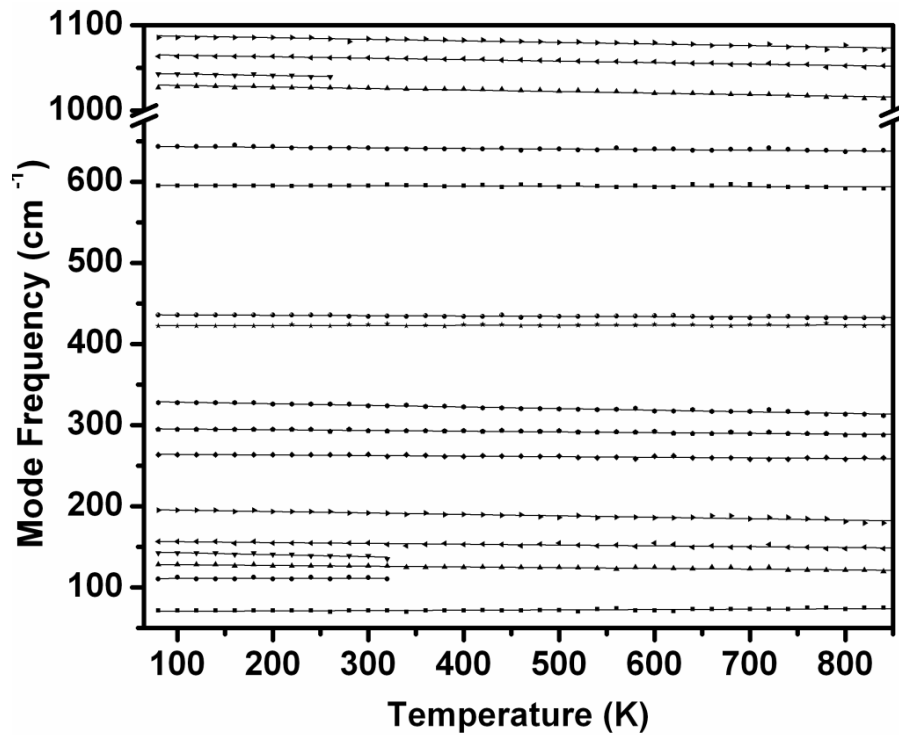


Figure 3.7 ω vs. T of NZP showing monotonic decrease in the mode frequencies of all modes except the two lowest at 72 and 110 cm^{-1} that exhibit opposite behaviour.

These numbers represent the total anharmonicities of the modes. Separation of true anharmonic and quasiharmonic parts was effected using the eq. (1.5).⁷ Using the present mode Gruneisen parameters γ_i and thermal expansion coefficient $\alpha=4.5\times 10^{-6}\text{K}^{-1}$, we obtain the anharmonicities of 17 of the 27 modes at 80 K (Table.3.3).

Table 3.3 Total anharmonicities, quasiharmonic and true-anharmonic contributions of different phonons in NZP. The numbers in the parentheses are standard errors in the least significant digit.

Mode Frequencies (cm^{-1})	Total anharmonic (10^{-5} K^{-1})	Quasiharmonic $\alpha\gamma_j$ (10^{-5} K^{-1})	True anharmonic (10^{-5} K^{-1})
72	5.9(3)	-1.0(2)	4.9
110	1.7(3)	-0.2(9)	1.6(2)
126	-7.1(9)	0.08(5)	-7.1
139	-10.9(3)	0.2(6)	-10.7(5)
154	-6.5(3)	0.3(8)	-6.1(5)
192	-9.1(9)	0.1(9)	-9.0(6)
262	-2.7(4)	0.1(1)	-2.6(2)
293	-3.0(9)	0.1(4)	-2.9(5)
325	-6.1(1)	0.2(9)	-5.8(2)
422	0.2(7)	0.05(4)	0.3(3)
435	-0.9(7)	0.1(4)	-0.8(3)
595	-0.4(4)	0.06(8)	-0.3(7)
642	-1.1(1)	0.1(1)	-1.0(3)
1026	-1.7(8)	0.08(6)	-1.6(8)
1040	-1.7(6)	0.1(3)	-1.6(2)
1061	-1.6(2)	0.09(9)	-1.5(2)
1084	-1.7(2)	0.08(1)	-1.6(3)

The magnitude of anharmonicity of these modes is almost an order of magnitude less compared to zirconium tungstate⁴⁶ which indicates lower contribution to thermal expansion. The values of true-anharmonicities for all modes except 72, 112 and 422 cm^{-1} are negative. The magnitude of intrinsic (true) anharmonicity is higher for low frequency modes (especially for modes at 126, 139, 154, 192, 325 cm^{-1}) compared to the high frequency modes which agrees well with the fact that the internal modes are harder compared to the low frequency modes. Table 3.3 also shows that quasi-harmonic (implicit) contribution for all modes are small; thus the true anharmonicities are nearly the same as the total anharmonicities. It also signifies the little change in lattice volume with increase in temperature so that the modes remain stable and intact without any phase transition due to small values of implicit contribution.

3.3.2. High Pressure XRD

We have performed *in situ* high pressure x-ray diffraction measurements on NZP to obtain the bulk modulus and to confirm the phase transformation indicated by Raman spectroscopy. XRD patterns at several different pressures (Figure 3.8) were analyzed using POWD software. Up to 4.8 GPa the patterns could be indexed with a good figure of merit of 11 to a hexagonal structure $R\text{-}3c$ with monotonically decreasing volume. Several new peaks (at $2\theta=9.8, 11.2, 15.1, 21.1$ deg.) emerge around 5.4 GPa, some old peaks ($2\theta=16.1, 24.9$) disappear, and the pattern is quite different from the starting phase around 9.1 GPa.

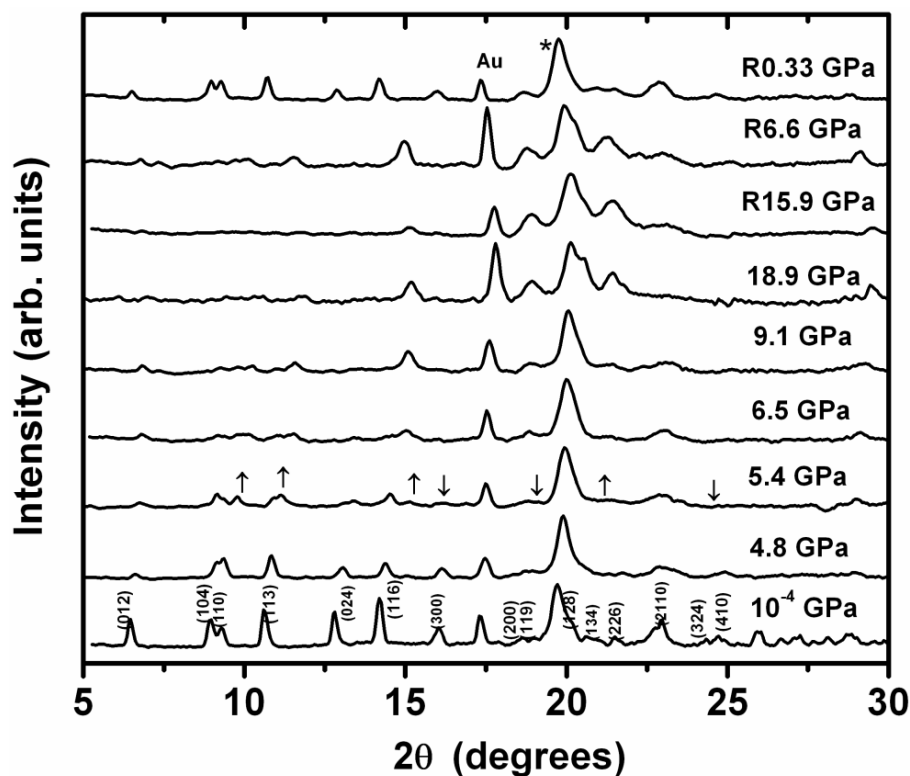


Figure 3.8 XRD patterns at different pressures. * denotes gasket peak, Au – pressure marker. Disappearance of several reflections is noticeable above 6 GPa. Patterns recorded in the pressure reducing cycle are indicated by the prefix ‘R’.

The quality of XRD patterns in this high pressure phase does not permit us to unambiguously determine its structure. When the P vs. V in the hexagonal phase is fitted to third order Birch Murnaghan equation,⁴⁷ a bulk modulus value B_0 of 47 ± 5 GPa and $B_0' = 8 \pm 4$ are obtained. On decompression the XRD patterns corresponding to the original phase are obtained (Figure 3.8), indicating the reversibility of the phase transformation.

High pressure studies on flexible materials such as SiO_2 and GeO_2 with α -quartz structure indicate large compressibilities without much variation in bond lengths. There are large changes in bond angles but there is no bond breaking; tilting and rotation of polyhedral units help the structures remain stable.³⁰ Earlier high pressure XRD study⁸ on $\text{RbTi}_2(\text{PO}_4)_3$ also showed an isostructural phase

transformation (from $R-3c$ to $R-3$) due to the distortion of Ti-P framework that causes the interstitial cavities to collapse around the larger rubidium cation with increase in coordination of the cation. From the present results we conclude that a reversible phase transformation occurs around 6 GPa and this phase continues to exist at least up to 20 GPa.

Raman spectroscopic and x-ray diffraction investigations of NZP at high pressures shows a phase transformation at 5.4 GPa, but the structure of the high pressure phase could not be ascertained from the XRD data obtained from a laboratory based instrument due to poor signal intensities. We have now carried out XRD measurements in a synchrotron to study this transition. Selected diffraction patterns up to 10 GPa are plotted in Figure 3.9.

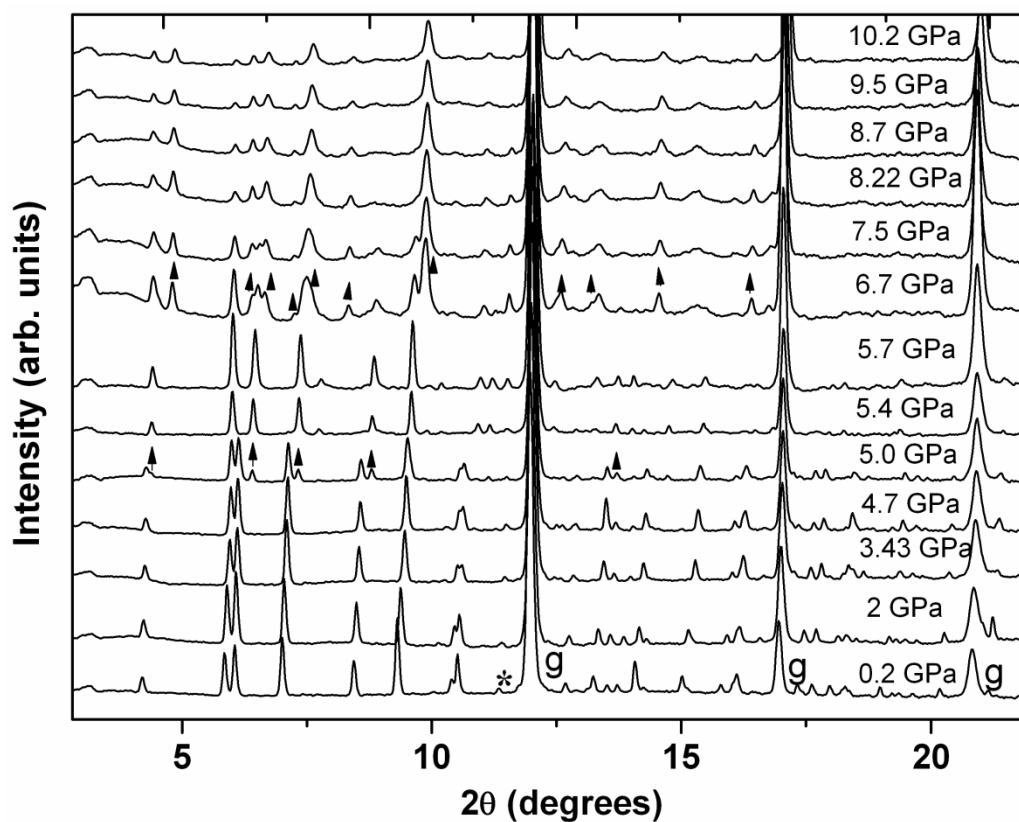


Figure 3.9 X-ray diffraction patterns of NZP at different pressures. ‘g’ indicates peaks arising due to tungsten gasket. Note that the upward arrows indicate the reflections arising in the new phases around 5 and 6.7 GPa.

All peaks shift to larger 2θ that is expected from a reduction of d spacings with increasing pressure. Variation of lattice parameters with pressure is shown in Figure 3.10. Compressibility of c -axis is three times greater than that of the a -axis (inset Figure 3.10) for ambient phase. Bulk modulus of the compound for the low pressure phase (up to 5 GPa) is calculated to be 53.2(3) GPa with $B'=4$ by fitting the P - V data to third order Birch-Murnaghan equation of state (Figure 3.11).

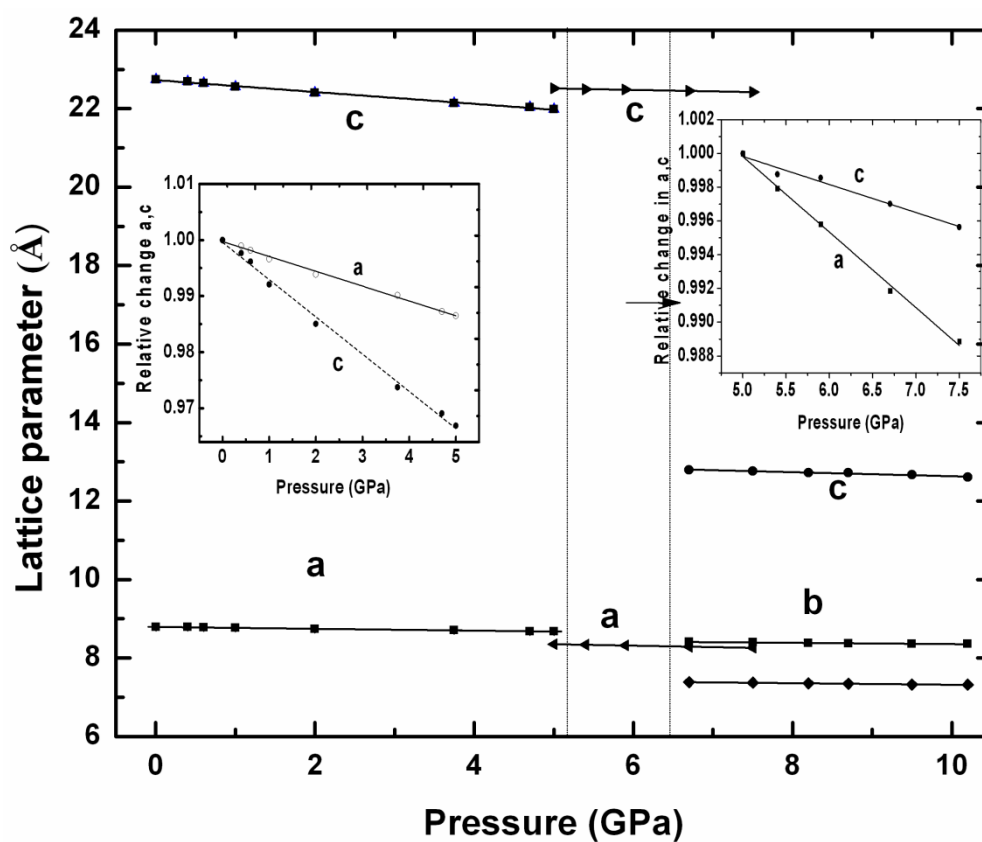


Figure 3.10 Variation of lattice parameters with pressure. Dotted lines partition different phases such as $R-3c$, $R3$ with a and c lattice parameter and orthorhombic structure with a , b and c lattice parameter.

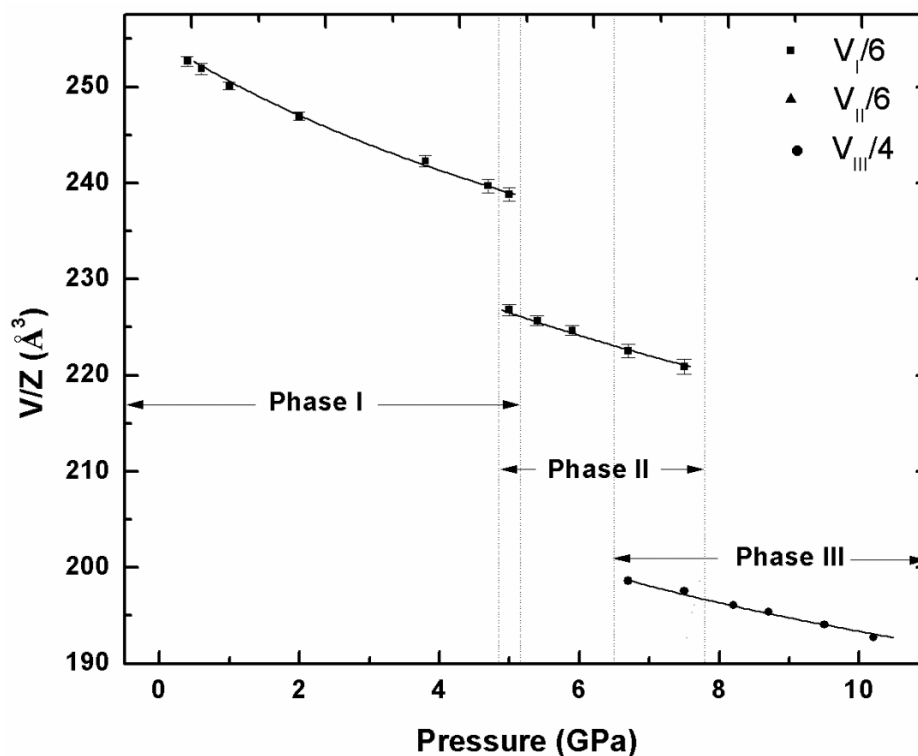


Figure 3.11 Pressure dependence of volume per N/ZP formula unit (Z). The solid lines show the fitting with the third order Birch Murnaghan equation of state for the three different phases.

It is noteworthy that the bulk modulus of low pressure phase of $\text{RbTi}_2(\text{PO}_4)_3$ (up to 1.7 GPa) was reported to be 104 GPa⁸. On comparison, it is seen that compressibility increases or lattice softens with substitution of a smaller cation (Na). The increase in compressibility in N/ZP compounds can be explained as due to the cooperative interaction of bond compression and bond angle bending mechanism³⁰.

On further compression of N/ZP from 5 GPa, five new weak peaks appear, and their intensities increase at higher pressures. This suggests the appearance of a new phase (phase II) that coexists with the original phase at 5 GPa. The new diffraction peaks could be indexed to $R3$ structure similar to isostructural $\text{RbTi}_2(\text{PO}_4)_3$ ⁸ (Figure 3.12). The corresponding variation of lattice parameters with pressure is shown in Figure 3.10. Above 5 GPa the intensities of reflections corresponding to (0 0 9) and (3

0 15) (Figure 3.13) increase significantly, which is responsible for violation of c -glide symmetry indicating a transition from $R-3c$ to $R3$ structure⁸.

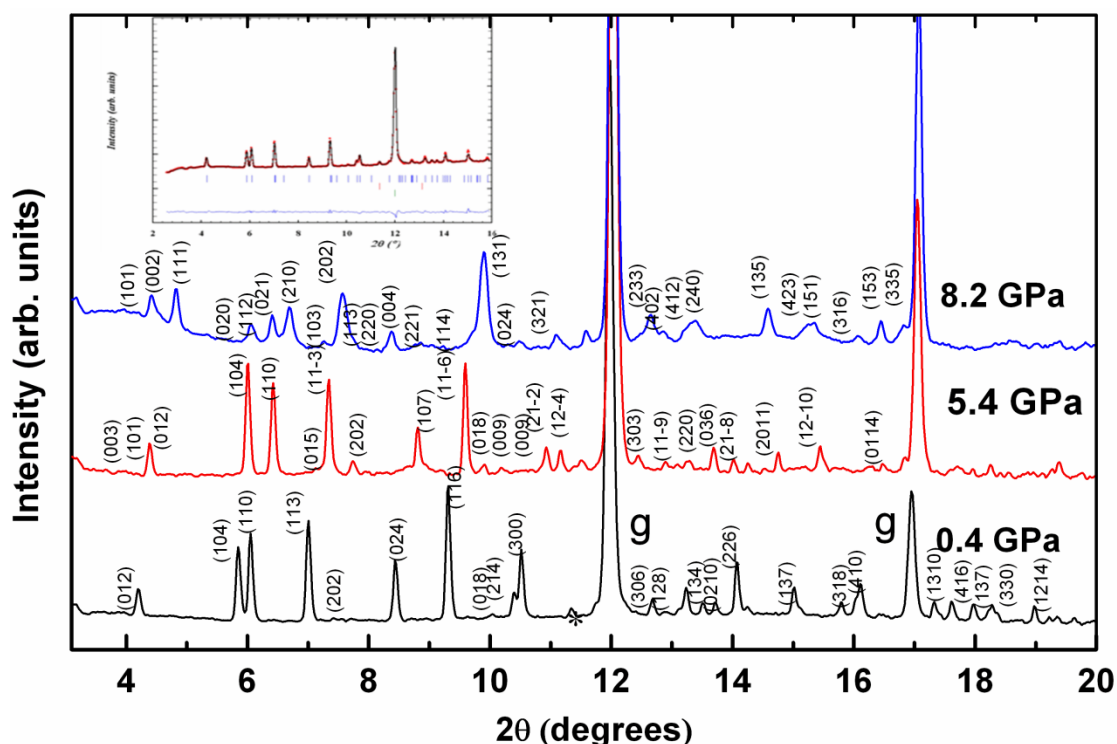


Figure 3.12 X-ray diffraction peaks are indexed with $R-3c$, $R3$ and orthorhombic phases at 0.4, 5.4, 8.2 GPa. Inset shows the Rietveld fitted pattern at 0.4 GPa.

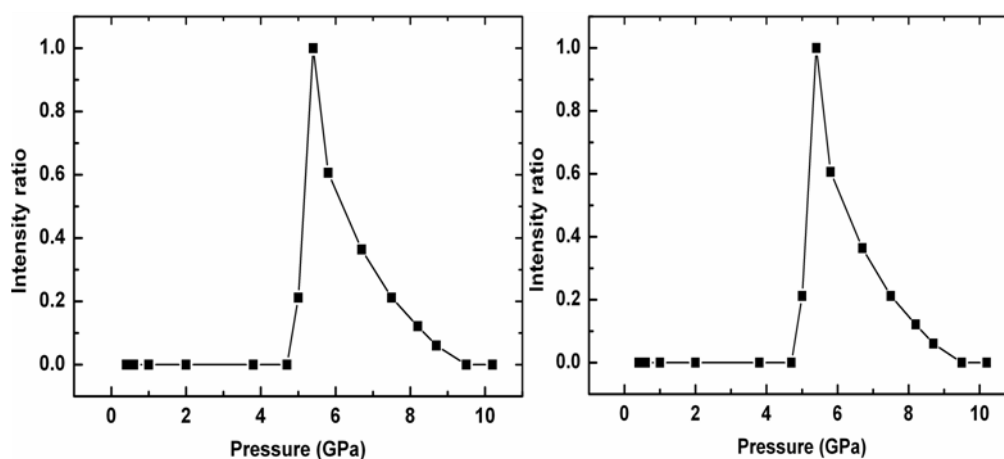


Figure 3.13 Intensity of the peak corresponding to the (009) plane (a) and the (3015) plane (b) on compression suggests a transition to $R3$ phase. To take into account differences in exposure time between diffraction images, the intensity was scaled to that of the strongest

peak in the diffraction pattern. The resultant values were normalized to that of 8.2 GPa measurement.

This transition might be due to a reduction of Zr-O-P angles and the consequent collapse of Na sites similar to the case of $\text{RbTi}_2(\text{PO}_4)_3$ ⁸. In this phase, the reduction in the *a*-lattice parameter is more than that of the *c*-parameter (inset Figure 3.10) that could be due to the rotation of ZrO_6 octahedra along the *c*-axis. The bulk modulus of this phase II (5 - 7.5 GPa) of NZP is found to be 36(1) GPa with $B' = 4$ whereas the high pressure phase of $\text{RbTi}_2(\text{PO}_4)_3$ (1.7 – 6 GPa) was found to be 60 GPa with $B' = 4$. While most solids become less compressible at high pressure NZP shows a different behavior. NZP becomes more compressible with increasing pressure over a limited range of pressures, 5 – 7.5 GPa. Increased compressibility at high pressure has been observed in other flexible framework compounds indicating a commencement of a reversible tilt transition to a structure of lower symmetry⁸. Similar to $\text{RbTi}_2(\text{PO}_4)_3$ ⁸, angles between corner linked polyhedra defined by Zr-O-P linkage in NZP might change significantly leading to a collapse of cavities around Na cations increasing their coordination from six to twelve.

On further compression, several new broad peaks arise around 6.7 GPa with increase in X-ray scattering background indicating the formation of a new phase (phase III) that could be disordered. Coexistence of phases II and III was observed between 6.7 and 7.5 GPa. At 8.2 GPa, the pattern could be indexed to a single, orthorhombic structure with space group *Pbcn* using POWD software (Figure 3.12). The corresponding lattice parameters are plotted in Figure 3.10. The bulk modulus $B = 65$ GPa with $B' = 4$ for this phase III was estimated by fitting the P-V data to the third order Birch Murnaghan equation. The increase in bulk modulus indicates stiffening of the lattice on compression, and this phase is stable up to 10 GPa. The disorder in this

phase might be due to the difference in Na occupancy over different sites. The observed orthorhombic phase is found to be similar to the high temperature orthorhombic phase³¹ of monoclinic $\text{LiZr}_2(\text{PO}_4)_3$. Pressure induced phase transition has been predicted for high temperature rhombohedral ($R\bar{3}c$) phase³¹ of triclinic $\text{LiZr}_2(\text{PO}_4)_3$ to high temperature orthorhombic ($Pbna$) phase of monoclinic $\text{LiZr}_2(\text{PO}_4)_3$ ³¹ due to a difference in unit cell volumes. Similar kind of transition is possible for $\text{NaZr}_2(\text{PO}_4)_3$ at high pressure, with an intermediate $R\bar{3}$ phase (i.e., Phase II).

3.4. Summary and conclusion

Thermal expansion behavior of $\text{NaZr}_2(\text{PO}_4)_3$ is investigated using Raman spectroscopy as a function of temperature at ambient pressure, and as a function of pressure at ambient temperature. From an analysis of these results the anharmonicity of the various phonon modes are obtained and the individual modes that make negative and positive contributions to thermal expansion in this material are identified. Modes at 72 and 112 cm^{-1} contribute negatively to overall thermal expansion. We find indications of phase transformation at 5 and 5.8 GPa from our high-pressure Raman studies. First principles density functional theoretical calculations were carried out using VASP code. Mode assignments were carried out using Phonopy combined with VASP computed zone-centre phonon frequencies and Eigen vectors. Thermal expansion coefficient obtained from the calculated phonon mode frequencies at different volumes is in good agreement with reported experimental value. Two NTE modes identified in Raman studies corresponds to PO_4 tetrahedral librations and Zr translations. From our first principles equation of state calculations at several pressures from ambient to 5 GPa, we find that $\text{NaZr}_2(\text{PO}_4)_3$ has a bulk modulus of 45 GPa, in agreement with the measured value of 53 GPa. High

pressure XRD confirms two phase transitions around 5 and 6.7 GPa which are indexed to a rhombohedral ($R3$) and an orthorhombic phase respectively. The bulk modulus for high pressure phases is calculated. Two soft E_g modes in the ambient phase are found to be responsible for polyhedral tilt transition at 5 GPa.

3.5. References

- ¹J. Alamo, *Solid State Ionics* **63**, 547 (1993).
- ²T. Ota and I. Yamai, *J. Ceram. Soc. Jpn.* **95**, 531 (1987).
- ³K. V. G. Kutty, R. Asuvatharaman, C. K. Mathews, and U. V. Varadaraju, *Mater. Res. Bull.* **29**, 1009 (1994).
- ⁴V. I. Petkov, A. I. Orlando, G. N. Kasantsev, S. G. Samoilo, and M. L. Spiridonova, *J. Therm. Anal. Cal.* **66**, 623 (2001).
- ⁵V. I. Petkov, E. A. Asabina, A. V. Markin, N. N. Smirnova, and D. B. Kitaev, *J. Therm. Anal. Cal.* **80**, 695 (2005).
- ⁶I. J. Kim and G. Cao, *J. Eur. Ceram. Soc.* **22**, 2627 (2002).
- ⁷B. A. Weinstein and R. Zallen in *Light Scattering in Solids IV* Eds. M. Cardona and G. Guntherodt, (Springer-Verlag), Berlin, p. 463 (1984).
- ⁸R. M. Hazen, D. C. Palmer, L. W. Finger, and G. D. Stucky, *J. Phys.: Condens. Matter* **6**, 1333 (1994).
- ⁹D. K. Agarwal and J. H. Adair, *J. Am. Ceram. Soc.* **73**, 2153 (1990).
- ¹⁰E. Wu, *J. Appl. Cryst.* **22**, 506 (1989).
- ¹¹K. K. Pandey, H. K. Poswal, A. K. Mishra, A. Dwivedi, R. Vasanthi, N. Garg and S. M. Sharma, *Pramana J. Phys.* **80**, 4607 (2013).
- ¹²E. Prleto, *Phys. Rev. B* **129**, 37 (1963).
- ¹³W. B. Holzapfel, M. Hartwig and W. Sievers, *J. Phys. Chem.* **30**, 515 (2001).
- ¹⁴A. P. Hammersley, S. O. Svensson, M. Hanfland, A. N. Fitch and D. Hauserman, *High Pressure Res.* **14**, 235 (1996).
- ¹⁵J. Roisnel, J. Rodriguez-carvajal, *Material Science Forum* **118**, 378 (2001).
- ¹⁶G. Kresse and J. Hafner, *Phys Rev. B* **47**, 558 (1993).
- ¹⁷G. Kresse and J. Hafner, *Phys. Rev. B* **49**, 14251 (1991).

- ¹⁸G. Kresse and J. Furthmuller, *Phys. Rev. B* **54**, 11169 (1996).
- ¹⁹L. O. Hagman and P. Kierkegaard, *Acta Chem. Scand.* **22**, 1822 (1968).
- ²⁰D. Vanderbilt, *Phys. Rev. B* **41**, 7892 (1990).
- ²¹J. P. Perdew, J. A. Chevary, S. H. Vosko, K. A. Jackson, M. R. Pederson, D. J. Singh and C. Fiolhais, *Phys. Rev. B* **46**, 6671 (1992).
- ²²H. J. Monkhorst and J. D. Pack, *Phys. Rev. B* **13**, 5188 (1976).
- ²³X. Gonze and C. Lee, *Phys. Rev. B* **55**, 10355 (1997).
- ²⁴S. Baroni, S. de Gironcoli, and A. Del Corso, *Rev. Mod. Phys.* **73**, 515 (2001).
- ²⁵X. Wu, D. Vanderbilt and D. R. Hamann, *Phys. Rev. B* **72**, 035105 (2005).
- ²⁶D. Karhanek, T. Bucko and J. Hafner, *J. Phys.: Condens. Matter* **22**, 265006 (2010).
- ²⁷A. Togo, F. Oba, and I. Tanaka, *Phys. Rev. B* **78**, 134106 (2008).
- ²⁸K. Momma and F. Izumi, *J. Appl. Crystallogr.* **41**, 653 (2008).
- ²⁹K. Kamali, T. R. Ravindran, C. Ravi, Y. Sorb, N. Subramanian and A. K. Arora, *Phys. Rev. B* **86** 144301 (2012).
- ³⁰R. M. Hazen, *Comparative Crystal Chemistry*, New York: Wiley (1982).
- ³¹M. Catti, N. Morgante and R. M. Ibberson, *J. Solid State Chem.* **152** 340 (2000).
- ³²W. G. Fateley and F. R. Dollish, *Infrared and Raman Selection Rules for Molecular and Lattice Vibrations*, Wiley-Interscience, New York, 1972.
- ³³M. Barj, H. Perthuis, and Ph. Colomban, *Solid State Ionics* **11**, 157 (1983).
- ³⁴P. Tarte, A. Rulmont, and C. Merckaert-Ansay, *Spectrochimica Acta A*, **42**, 1009 (1986).
- ³⁵T. R. Ravindran, A. K. Arora, and T. A. Mary, *J. Phys.: Condens. Matter* **13**, 11573 (2001).
- ³⁶T. R. Ravindran, A. K. Arora, S. Chandra, M. C. Valsakumar, and N. V. Chandra Shekar, *Phys. Rev. B* **76**, 054302 (2007).

- ³⁷ A. Kourouklis, A. Jayaraman, A. and A. Ballman, *Solid State Commun.* **62**, 379 (1987).
- ³⁸ K. W. Chapman and P. J. Chupas, *J. Am. Chem. Soc.* **129**, 10090 (2007).
- ³⁹ C. A. Perottoni and J. A. H. Jornada, *Science* **280**, 886 (1998).
- ⁴⁰ H. K. Poswal, A. K. Tyagi, A. Lausi, S. K. Deb, and S. M. Sharma, *J. Solid State Chem.* **182**, 136 (2009).
- ⁴¹ A. K. Arora, R. Nithya, T. Yagi, N. Miyajima and T. A. Mary, *Solid State Commun.* **129**, 9 (2004)
- ⁴² T. Sakuntala, A. K. Arora, V. Sivasubramanian, R. Rao, S. Kalavathi, and S. K. Deb, *Phys. Rev. B* **75**, 174119 (2007).
- ⁴³ R. Rao, Alka. G. Garg, and T. Sakuntala *J. Appl. Phys.* **108**, 083508 (2010).
- ⁴⁴ N. Chandrabhas and A. K. Sood, *Phys. Rev. B* **51**, 14 (1995).
- ⁴⁵ P. Vinet, J. H. Rose, F. Ferrante, and J. R. Smith, *J. Phys.: Condens. Matter* **1**, 1941 (1989).
- ⁴⁶ T. R. Ravindran, A. K. Arora, and T. A. Mary, *Phys.Rev.B* **67**,064301 (2003).
- ⁴⁷ F. Birch, *J. Geophys. Res.***83**, 1257 (1978).

Chapter 4

Comparative Raman spectroscopic study of phase stability and anharmonic effects in $AZr_2(PO_4)_3$ (A= K, Rb and Cs)

4.1. Introduction

In $AZr_2(PO_4)_3$ (A= K, Rb, Cs) substitution of Na by K, Rb and Cs does not change the parent rhombohedral structure with space group R-3c. $NaZr_2(PO_4)_3$ (NZP), $KZr_2(PO_4)_3$ (KZP), $RbZr_2(PO_4)_3$ (RbZP) and $CsZr_2(PO_4)_3$ (CsZP) exhibit overall thermal expansion coefficient $\alpha_{av} \approx 4.5 \times 10^{-6} \text{ K}^{-1}$, $-0.4 \times 10^{-6} \text{ K}^{-1}$, $-0.36 \times 10^{-6} \text{ K}^{-1}$ and $0.4 \times 10^{-6} \text{ K}^{-1}$ respectively from 293 to 1273 K.¹ Thermal expansion coefficients can be tuned by substitution of interstitial cations of different sizes.² On substitution of larger cations, thermal expansion coefficients become larger along the *a*-axis and shorter along the *c*-axis due to the bridging of PO_4 tetrahedra.² Hence, thermal expansion anisotropy is observed to be decreased when larger cations are substituted in place of smaller cations.² In the work of Tarte *et al*, Raman and IR spectra of rhombohedral orthophosphates $M^I M_2^{IV}(PO_4)_3$ were discussed on the basis of various chemical composition.³ Temperature and pressure dependent Raman spectroscopic and first principles computational studies have provided valuable insight into the role of the various phonon modes to anisotropic thermal expansion in prototypic $NaZr_2(PO_4)_3$.⁴ In the present work the influence of temperature and pressure on these compounds is investigated to explain the anharmonic low thermal expansion behavior.

Low thermal expansion compounds are sensitive to pressure induced phase instability which limit technological applications. For example, ZrW_2O_8 with large isotropic negative thermal expansion coefficient over a wider range of temperature exhibits an irreversible structural phase transformation at 0.3 GPa followed by amorphization at 2.2 GPa.⁵ $\text{Zn}(\text{CN})_2$ undergoes a cubic-orthorhombic phase transformation around 1.3 GPa under hydrostatic conditions.⁶ At ambient temperature, orthorhombic-monoclinic phase transition at 0.3 GPa has been reported in anisotropic $\text{Sc}_2(\text{MO}_4)_3$.⁷ Alkali cation substituted NZP compounds are stable up to 1273 K.⁸ There are not many reports on the behavior of NZP family with respect to pressure: prototypic NZP undergoes structural phase transformations around 5 and 6 GPa maintaining structural integrity up to 32 GPa.⁹

Raman shifts originate from the polarization of chemical bonds and hence Raman spectroscopy is helpful in probing structural changes at the level of chemical bonds. In situ Raman spectroscopy study at high temperature and pressure is preferred method to compare the phase stability of compounds of NZP family. Study of anharmonicity is important to explain thermal expansion property due to intrinsic phonon scattering in a solid.

The current study is focused on two aspects: (a) to compare and analyze the contribution of various phonon modes to anisotropic low thermal expansion with increasing size of alkali cations through experiments and first-principles calculations and (b) to investigate the structural stability of the cation substituted compounds with pressure. Raman spectroscopic studies were carried out up to 30 GPa at ambient temperature and from 80 to 860 K at ambient pressure to identify anharmonic phonons. Raman modes contributing to NTE are visualized by attaching atomic displacement vectors computed from density functional perturbation theory (DFPT).

Bulk moduli for the above compounds are computed by fitting energy-volume data obtained from density functional theory (DFT) to third order Birch-Murnaghan equation.

4.2. Experimental and computational details

$\text{KZr}_2(\text{PO}_4)_3$, $\text{RbZr}_2(\text{PO}_4)_3$ and $\text{CsZr}_2(\text{PO}_4)_3$ were synthesised using sol gel technique described elsewhere.⁴ X-ray diffraction patterns were recorded using GNR ATD 2000Pro (Italy) X-Ray diffractometer with CuK_α radiation. The XRD patterns of all three samples match with the respective ICDD powder diffraction files confirming single phase without any impurities.¹⁰

For high pressure Raman measurements, AZP powder was loaded along with 4:1 methanol:ethanol pressure medium and a few ruby specks for pressure measurement in a 200 μm hole drilled in a pre indented stainless gasket and mounted in a compact, symmetric diamond anvil cell with diamonds of culet diameter 500 μm . Raman spectroscopic measurements were carried out using a micro Raman spectrometer (Renishaw, UK, model inVia) with 514.5 nm laser excitation. Spectra were recorded in both increasing and decreasing pressure cycles. Temperature dependent Raman measurements from 80 to 860 K were carried out using a heating and cooling microscope stage (Linkam THMS 600). The spectra were fitted to Lorentzian line shapes to determine the peak positions and full widths at half maxima (FWHM) using PeakFit software (JANDEL).

Theoretical calculation of phonon spectrum was carried out using VASP (Vienna *ab initio* simulation package).¹¹⁻¹³ Structural relaxations of the 36 atom rhombohedral primitive unit cell of $\text{AZr}_2(\text{PO}_4)_3$ A= K, Rb and Cs (space group $R-3c$ (167))¹⁴ were carried out. Phonon spectrum of KZP, RbZP and CsZP were computed using the

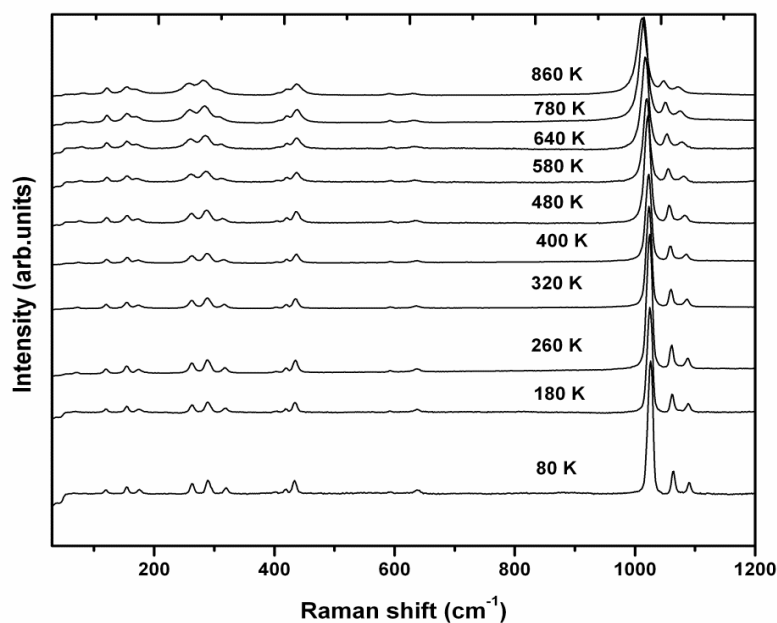
procedure reported elsewhere.⁴ Bulk moduli of $\text{KZr}_2(\text{PO}_4)_3$, $\text{RbZr}_2(\text{PO}_4)_3$ and $\text{CsZr}_2(\text{PO}_4)_3$ were computed by fitting DFT calculated energy-volume data to third order Birch-Murnaghan equation. Specific heat capacity is computed using Phonopy¹⁵ with $8 \times 8 \times 8$ k -grid mesh and VASP calculated force constants. Visual representations of the different phonon modes were obtained by plotting the eigenvectors of displacement of the various atoms in the unit cell using the VESTA visualization software.¹⁶

4.3. Results and discussion

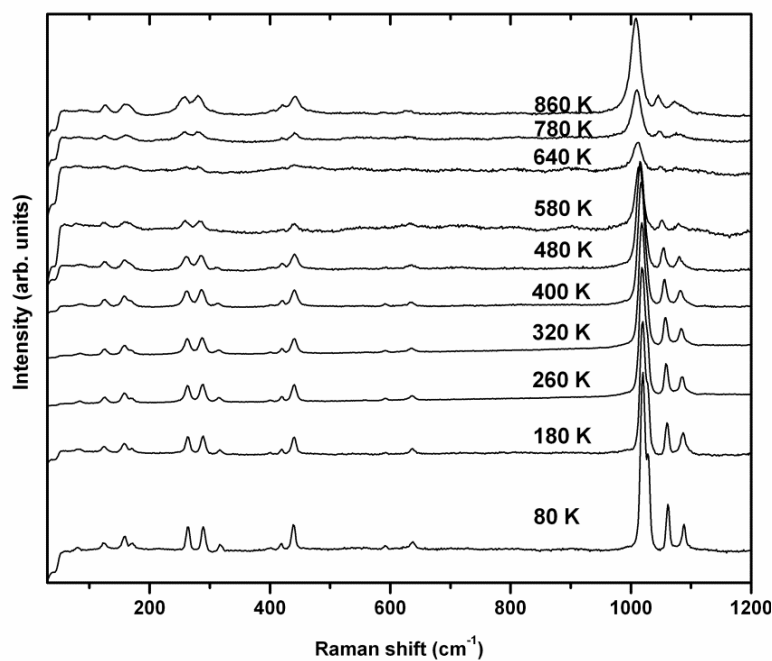
At ambient conditions, $\text{AZr}_2(\text{PO}_4)_3$, A= Na, K, Rb and Cs compounds have six formula units in the crystallographic unit cell (space group $R\bar{3}c$) giving rise to 108 degrees of freedom. Factor group analysis results in the total irreducible representation of $\Gamma_{\text{Total}}=8A_{1g}+9A_{2g}+17E_g+9A_{1u}+10A_{2u}+19E_u$. The irreducible representations associated with the Raman and IR active phonons are $8A_{1g} + 17E_g$ and $9A_{2u} + 18E_u$. Detailed classification into internal modes of phosphate ion and external modes are described elsewhere.⁴

4.3.1. Raman spectroscopic studies

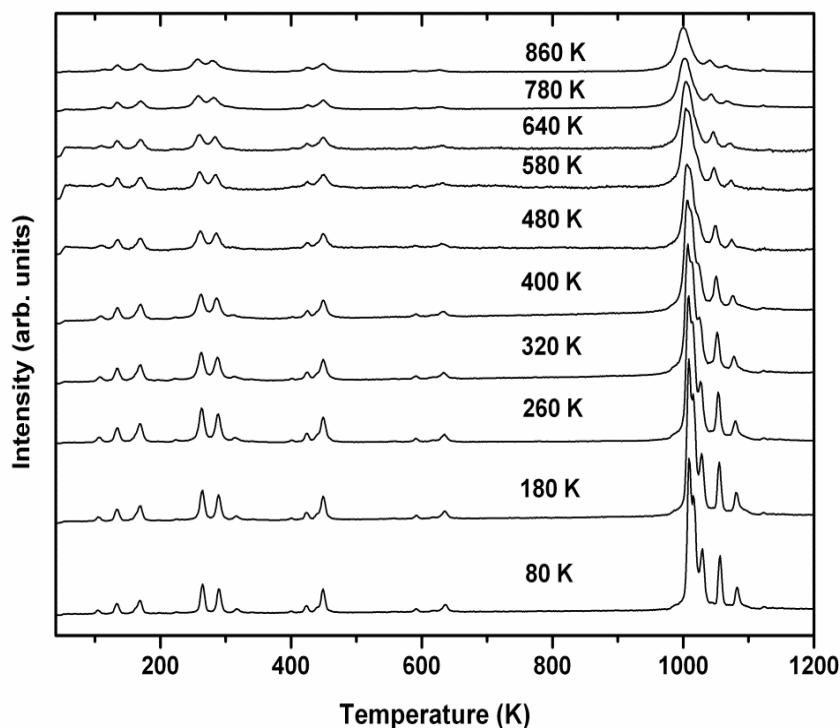
Raman spectra of NZP at different temperatures and their coefficients were reported in ⁴. Figure 4.1 (a, b and c) show the Raman spectra of $AZr_2(PO_4)_3$, $A = K, Rb$ and Cs at different temperatures up 860 K.



(a)



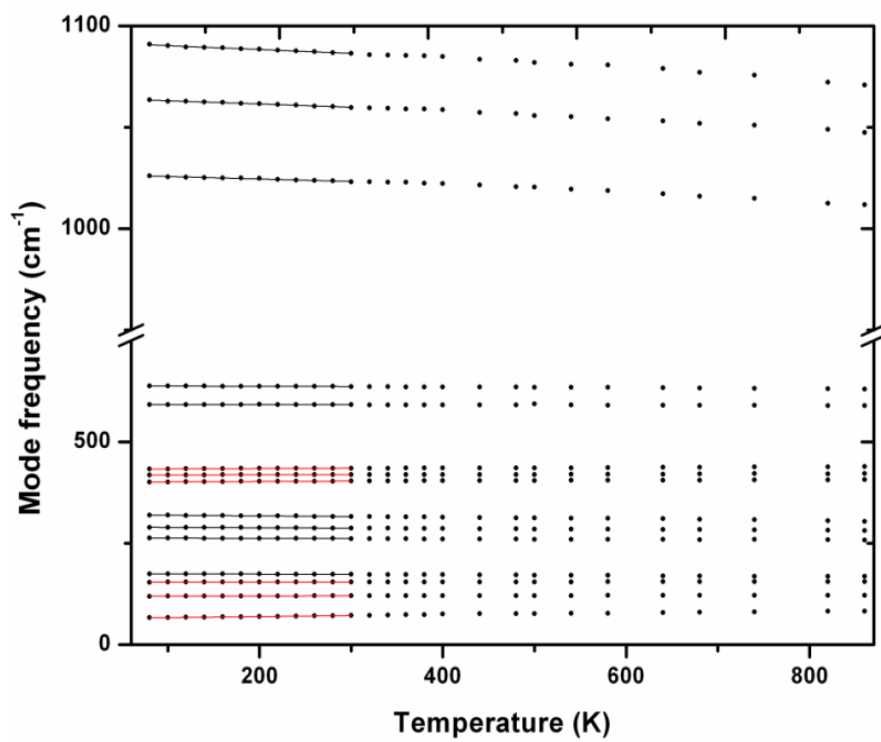
(b)



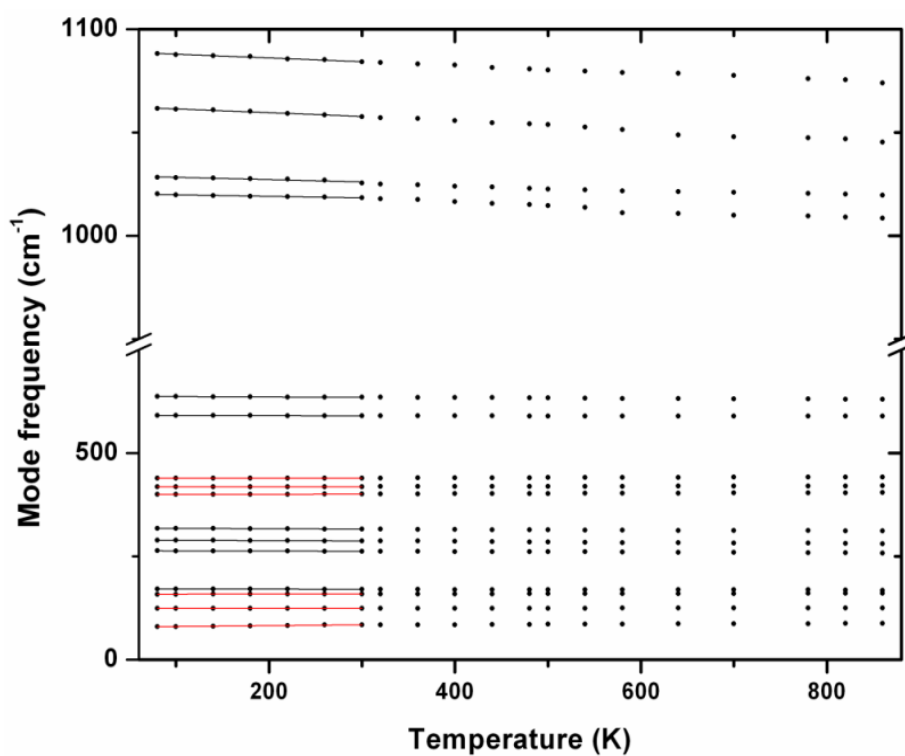
(c)

Figure 4.1 Raman spectra of (a) $\text{KZr}_2(\text{PO}_4)_3$ (b) $\text{RbZr}_2(\text{PO}_4)_3$ and (c) $\text{CsZr}_2(\text{PO}_4)_3$ at different temperatures. Low frequency region covers lattice modes and bending modes of PO_4 ion from $70\text{-}450\text{ cm}^{-1}$ and high frequency region corresponds to stretching modes of phosphate ion.

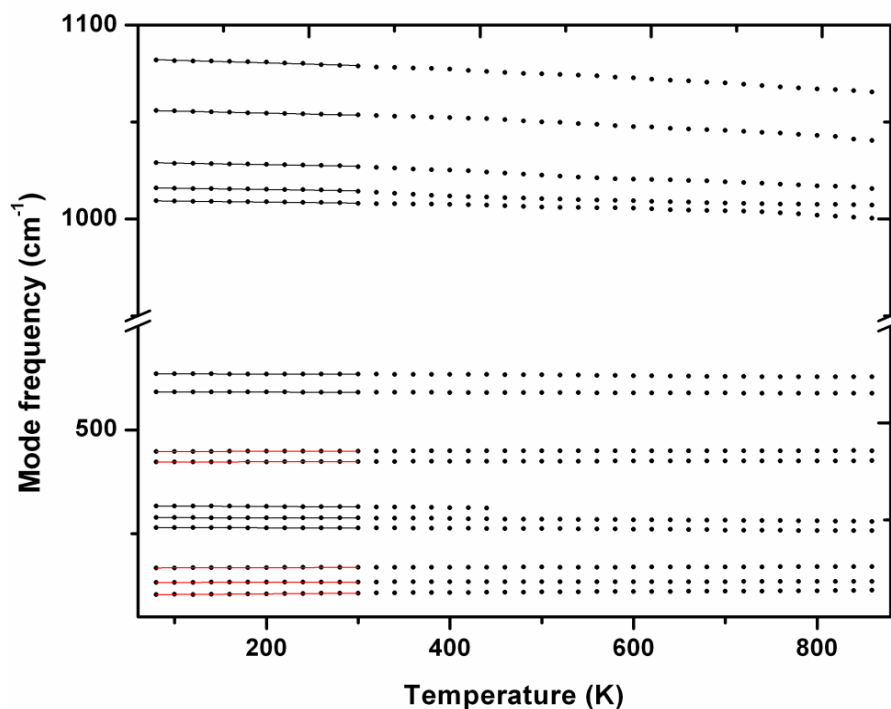
Temperature coefficients of the various phonon frequencies were obtained by linear fits to ω vs. T (Figure 4.2 a, b and c) only up to 300 K due to strong Umklapp process at high temperatures leading to non-linear dependence. At 80 K, a total of 15, 16 and 15 distinct Raman modes are observed in $\text{KZr}_2(\text{PO}_4)_3$ (KZP), $\text{RbZr}_2(\text{PO}_4)_3$ (RbZP) and $\text{CsZr}_2(\text{PO}_4)_3$ (CsZP) respectively, though 25 Raman modes are expected. Observation of less number of Raman modes than expected could be either due to accidental degeneracy of phonon frequencies or due to poor intensities arising from small polarisabilities.



(a)



(b)



(c)

Figure 4.2. Mode frequencies of various Raman modes as a function of temperature for (a) $\text{KZr}_2(\text{PO}_4)_3$ (b) $\text{RbZr}_2(\text{PO}_4)_3$ and $\text{CsZr}_2(\text{PO}_4)_3$. Modes at 74, 124, 403, 419 and 435 cm^{-1} for KZP and modes at 85, 126, 159, 401, 421 and 441 cm^{-1} for RbZP and modes at 105, 134, 168, 423 and 449 cm^{-1} in CsZP increase with increase in temperature which marked as red lines.

Tables 1, 2, 3 and 4 list the vibrational frequencies for NZP, KZP, RbZP and CsZP at ambient conditions for all observed Raman modes for comparison. Mode assignments for $\text{AZr}_2(\text{PO}_4)_3$, A= K, Rb and Cs are the same as those reported for $\text{NaZr}_2(\text{PO}_4)_3$.⁴ Vibrational frequencies for the first three low energy Raman bands and bands around 420 cm^{-1} of all four compounds (Table 4.1, 4.2, 4.3 and 4.4) increase with increase in the size of alkali cations (Na-K-Rb-Cs) whereas other bands show a slight decrease in frequency due to an increase in molecular volume. Tarte *et al*³ suggested that the anomalous behavior of the above four Raman modes was due to a contraction along the *a*-axis with increasing size of the A^{I} cation.

Table 4.1 Total anharmonicities, quasiharmonic and true-anharmonic contributions of different phonons in $\text{NaZr}_2(\text{PO}_4)_3$ with computed bulk modulus ($B_0=80$ GPa). The numbers in the parentheses are standard errors in the least significant digit.

Experimental Raman frequencies (cm^{-1})	Calculated Raman frequencies (cm^{-1})	Mode assignment	Isothermal Gruneisen parameter	Total anharmonicity (10^{-5} K^{-1})	Quasi-harmonicity (10^{-5} K^{-1})	True anharmonicity (10^{-5} K^{-1})
72	113	E_g	-1.9(4)	3.0(2)	-0.8(7)	2.14
112	127	E_g	-0.7(6)	3.4(7)	-0.3(4)	3.1(3)
126	141	A_{1g}	0.7(3)	-8.0(2)	0.3(2)	-7.6(9)
139	157	E_g	1.0(1)	-9.7(9)	0.4(5)	-9.3(3)
154	166	E_g	1.9(5)	-6.3(1)	0.8(7)	-5.4(3)
192	185	A_{1g}	0.7(4)	-8.2(2)	0.3(3)	-7.8(8)
262	273	E_g	0.6(9)	-2.7(4)	0.3(1)	-2.4(6)
293	298	A_{1g}	0.5(8)	-2.1(8)	0.2(6)	-1.9(3)
325	337	E_g	1.1(1)	-4.2(5)	0.5(2)	-3.7(3)
422	425	E_g	0.3(8)	0.2(7)	0.1(7)	0.4(4)
435	431	A_{1g}	0.6(3)	-1.3(6)	0.2(7)	-1.0(9)
595	577	A_{1g}	0.3(7)	-0.4(4)	0.1(6)	-0.3(7)
642	623	E_g	0.4(8)	-1.7(2)	0.2(2)	-1.5(9)
1026	927	E_g	0.5(9)	-0.6(5)	0.2(6)	-0.3(2)
1040	947	A_{1g}	0.5(8)	-1.0(9)	0.2(6)	-0.8(9)
1061	991	E_g	0.5(2)	-0.8(5)	0.2(4)	-0.6(8)
1081	1018	A_{1g}	0.6(1)	-1.1(2)	0.2(7)	-0.8(5)

Table 4.2 Total anharmonicities, quasiharmonic and true-anharmonic contributions of different phonons in $\text{KZr}_2(\text{PO}_4)_3$. The numbers in the parentheses are standard errors in the least significant digit.

Experimental Raman frequencies (cm^{-1})	Calculated Raman frequencies (cm^{-1})	Mode assignment	Isothermal Gruneisen parameter	Total anharmonicity (10^{-5} K^{-1})	Quasiharmonic (10^{-5} K^{-1})	True anharmonicity (10^{-5} K^{-1})
73	112	E_g	-9.0(7)	13.4(3)	0.3(6)	13.7(8)
120	124	E_g	-1.7(2)	4.0(7)	0.06(8)	4.1(4)
155	155	E_g	0.5(9)	1.6(2)	-0.01(9)	1.6(1)
174	169	A_{1g}	1.0(1)	-3.1(1)	-0.04(7)	-3.2(5)
263	268	E_g	1.3(4)	-2.0(7)	-0.05(4)	-2.0(2)
287	285	A_{1g}	0.8(8)	-3.4(7)	-0.03(5)	-3.5(1)
317	311	E_g	1.5(8)	-4.7(8)	-0.06(3)	-4.8(4)
403	405	E_g	0.5(5)	2.4(8)	-0.02(2)	2.4(6)
419	422	E_g	0.5(1)	1.0(2)	-0.02(1)	1.0(9)
435	424	A_{1g}	0.7(4)	2.1(8)	-0.02(9)	2.1(5)
593	571	A_{1g}	1.2(6)	-0.2(7)	-0.05(1)	-0.3(2)
636	616	E_g	0.5(9)	-0.8(2)	-0.02(3)	-0.8(4)
1023	1008	A_{1g}	0.8(9)	-1.1(8)	-0.03(6)	-1.2(5)
1060	1104	E_g	0.6(9)	-1.5(7)	-0.02(7)	-1.5(9)
1086	1116	A_{1g}	0.7(6)	-1.7(1)	-0.03(1)	-1.7(4)

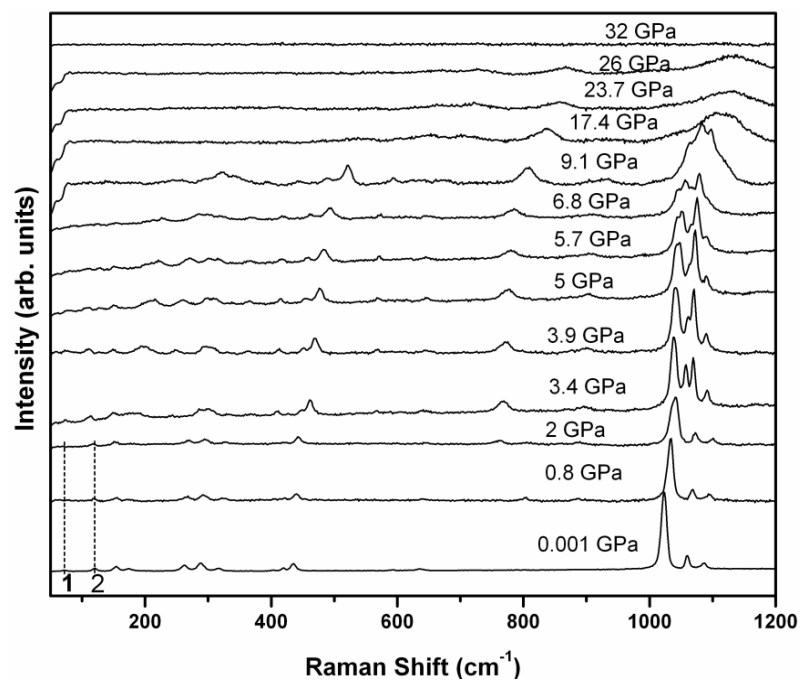
Table 4.3 Total anharmonicities, quasiharmonic and true-anharmonic contributions of different phonons in $\text{RbZr}_2(\text{PO}_4)_3$. The numbers in the parentheses are standard errors in the least significant digit.

Experimental Raman frequencies (cm^{-1})	Calculated Raman frequencies (cm^{-1})	Mode assignment	Isothermal Gruneisen parameter	Total anharmonicity (10^{-5} K^{-1})	Quasiharmonic (10^{-5} K^{-1})	True anharmonicity (10^{-5} K^{-1})
85	128	E_g	-5.9(6)	15.6(4)	0.1(9)	15.7(6)
126	134	E_g	-2.5(1)	1.5(9)	0.05(1)	1.6(8)
159	142	E_g	-1.3(5)	0.9(6)	0.03(5)	0.9(1)
170	174	A_{1g}	-1.2(9)	-0.9(1)	0.04(5)	-0.8(1)
264	264	E_g	3.1(3)	-1.9(2)	-0.07(1)	-2.0(3)
288	297	A_{1g}	1.4(3)	-2.9(8)	-0.3(2)	-2.9(2)
315	324	E_g	1.8(6)	-2.8(9)	-0.04(7)	-2.8(6)
401	394	E_g	0.2(4)	1.0(3)	-0.005(7)	1.0(2)
421	411	E_g	0.1(8)	0.6(7)	-0.004(5)	0.6(6)
441	434	A_{1g}	1.0(2)	0.6(7)	-0.02(7)	0.6(3)
592	574	A_{1g}	0.1(6)	-0.7(7)	-0.004(8)	-0.8(7)
636	616	E_g	0.4(3)	-0.7(5)	-0.101(5)	-1.5(6)
1019	917	A_{1g}	0.2(5)	-1.0(2)	-0.006(1)	-0.7(3)
1028	921	E_g	0.8(2)	-1.1(7)	-0.02(9)	-1.1(9)
1059	986	A_{1g}	0.2(9)	-1.6(1)	-0.007(1)	-1.7(1)
1085	1008	E_g	0.3(6)	-1.6(3)	-0.08(3)	-1.7(4)

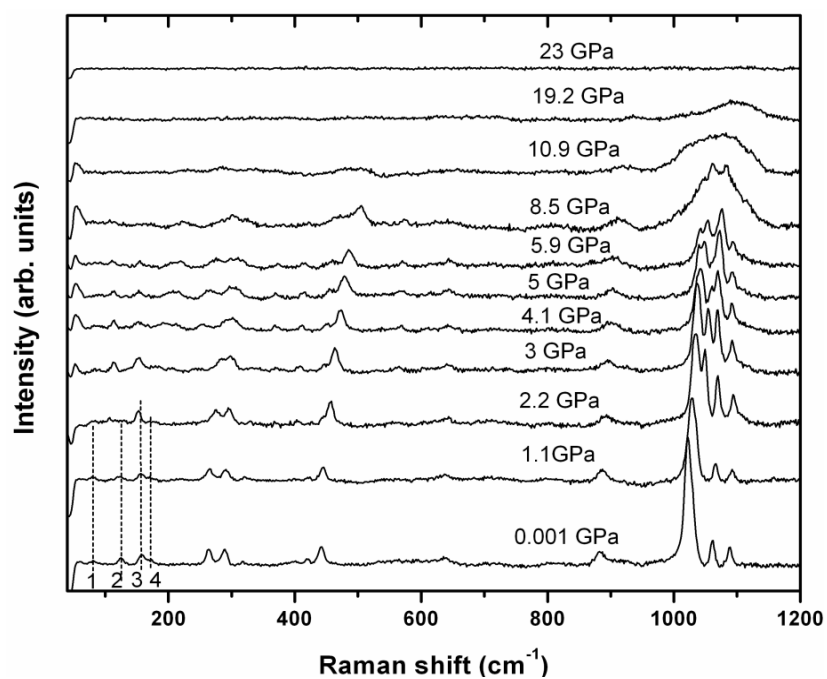
Table 4.4 Total anharmonicities, quasiharmonic and true-anharmonic contributions of different phonons in $\text{CsZr}_2(\text{PO}_4)_3$. The numbers in the parentheses are standard errors in the least significant digit.

Experimental Raman frequencies (cm^{-1})	Calculated Raman frequencies (cm^{-1})	Mode assignment	Isothermal Gruneisen parameter	Total anharmonicity (10^{-5} K^{-1})	Quasiharmonic (10^{-5} K^{-1})	True anharmonicity (10^{-5} K^{-1})
105	118	E_g	-5.0(2)	15.3(1)	-0.2(9)	15.4(1)
134	125	E_g	-1.1(5)	3.4(1)	-0.04(6)	3.3(6)
168	140	E_g	-1.3(8)	2.9(8)	-0.05(5)	2.8(5)
263	264	E_g	2.4(1)	-1.5(8)	0.09(6)	-1.4(8)
287	286	A_{1g}	1.3(3)	-1.3(8)	0.05(2)	-1.2(3)
313	312	E_g	1.7(8)	-3.1(9)	0.07(2)	-3.1(2)
423	430	E_g	0.3(4)	0.9(6)	0.01(4)	0.9(7)
449	440	A_{1g}	1.4(9)	1.1(4)	0.05(9)	0.5(9)
591	572	A_{1g}	0.7(3)	-0.8(3)	0.02(9)	-0.8(1)
634	614	A_{1g}	0.5(8)	-0.6(4)	0.02(3)	-0.5(2)
1007	847	E_g	0.3(4)	-0.5(3)	0.01(4)	-0.5(6)
1013	856	A_{1g}	0.3(7)	-0.7(8)	0.01(5)	-0.6(7)
1025	880	E_g	0.4(5)	-0.8(4)	0.01(8)	-0.7(3)
1052	947	E_g	0.7(5)	-0.9(1)	0.02(9)	-0.9(8)
1079	971	A_{1g}	0.8(1)	-0.9(9)	0.03(2)	-0.9(6)

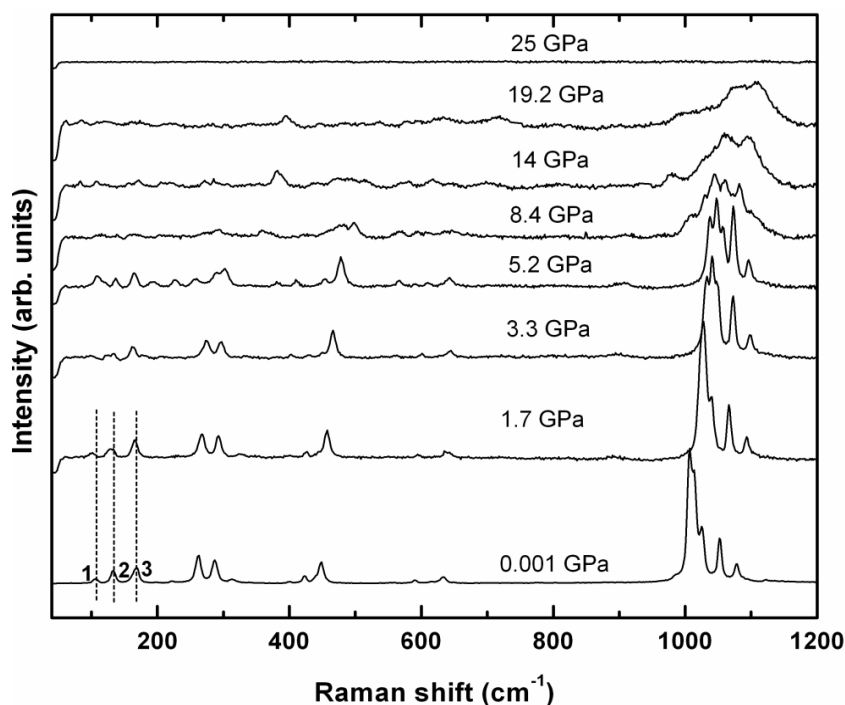
Figure 4.3 (a, b and c) show Raman spectra at different pressures of $AZr_2(PO_4)_3$, A= K, Rb and Cs. Pressure coefficients were obtained from mode frequency vs. pressure plots (Figure 4.4 (a, b and c)).



(a)



(b)

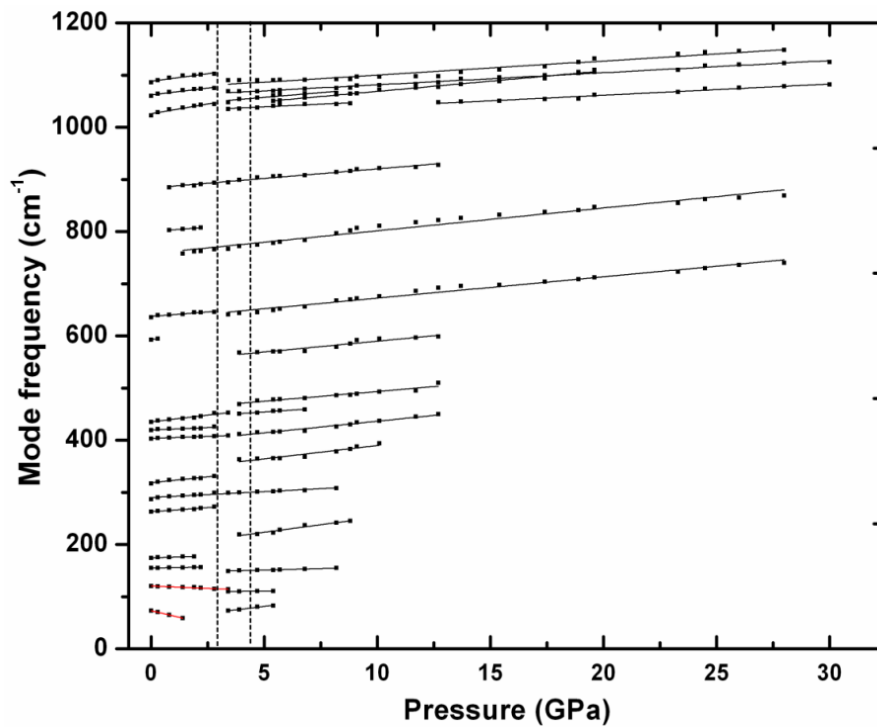


(c)

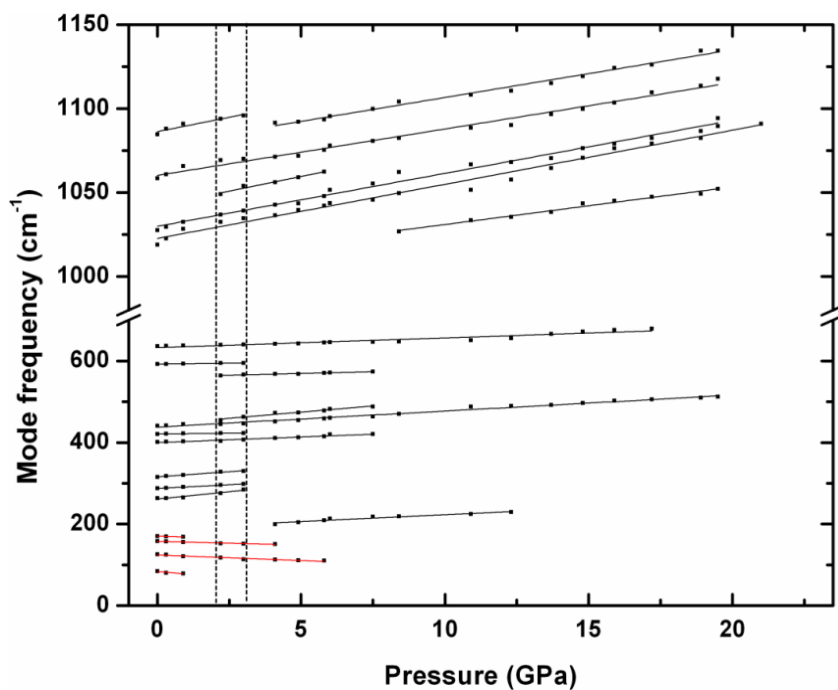
Figure 4.3 Raman spectra of (a) $\text{KZr}_2(\text{PO}_4)_3$ (b) $\text{RbZr}_2(\text{PO}_4)_3$ and (c) $\text{CsZr}_2(\text{PO}_4)_3$ at different pressures. KZP and RbZP show phase transition around 3.5 and 2.2 GPa and CsZP shows two transitions around 3.5 and 8.4 GPa. Pressure induced amorphisation for KZP, RbZP and CsZP occurs at higher pressures.

KZP and RbZP show a phase transition around 3.5 and 2.5 GPa respectively whereas CsZP exhibits two phase transitions at 3.4 and 8.4 GPa which is comparable to the two transition pressures of 5 and 6.6 GPa of NZP.⁹ Raman spectra after the first transition in KZP, RbZP and CsZP are observed to be similar to the Raman spectrum of NZP at 5.4 GPa⁹ indicating $R\bar{3}$ structure for first high pressure phase as in NZP.⁹ Indeed, high pressure XRD studies on isostructural $\text{RbTi}_2(\text{PO}_4)_3$ have revealed a phase transition from $R\bar{3}c$ to $R\bar{3}$ structure around 1.7 GPa.¹⁷ Raman bands in NZP (72 and 112 cm^{-1}),⁹ KZP (74 and 120 cm^{-1}), RbZP (85, 126, 159 and 170 cm^{-1}) and CsZP (105, 134 and 168 cm^{-1}) soften with increase in pressure and hence they are termed as soft modes. Such modes are responsible for structural instabilities at high pressure and amorphization later.

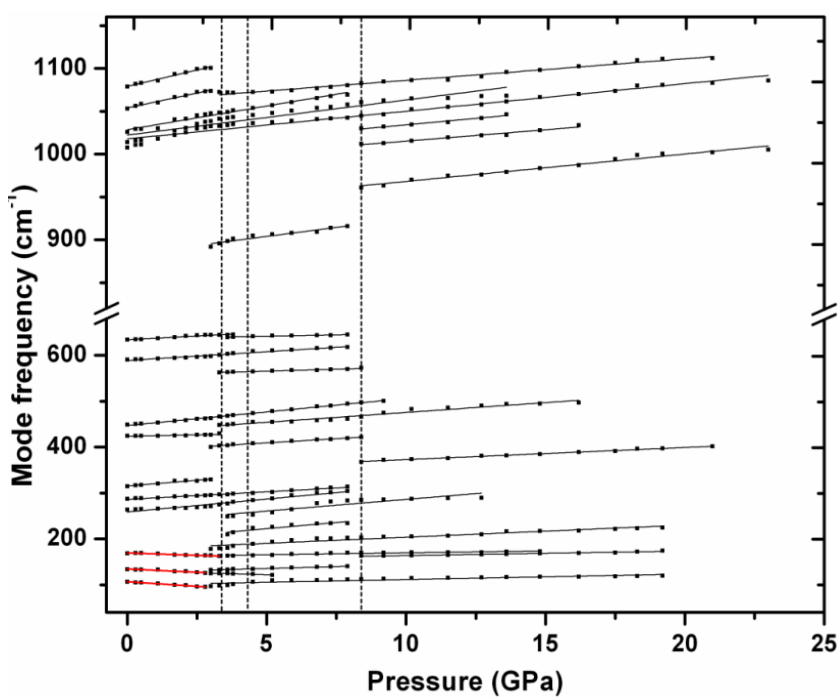
Compared to NZP that has two soft modes, RbZP has four soft Raman modes leading a phase transition to occur at a lower pressure of 2.2 GPa instead of 5 GPa. These soft modes contribute negatively to thermal expansion which is determined from the mode Gruneisen parameters $\gamma_i = \left(\frac{B_0}{\omega_i}\right) \left(\frac{d\omega_i}{dP}\right)$, where B_0 is the bulk modulus obtained from first principles calculations described later, and i is the i^{th} phonon mode. Thermal expansion coefficient above the phase transition is likely to be positive since the pressure coefficients of all Raman bands in the first high pressure phase are positive (Figure 4.4 (a), (b) and (c)).



(a)



(b)



(c)

Figure 4.4 Variation of Raman mode frequencies as a function of pressure for (a) $\text{KZr}_2(\text{PO}_4)_3$ (b) $\text{RbZr}_2(\text{PO}_4)_3$ and (c) $\text{CsZr}_2(\text{PO}_4)_3$. Modes at 74 and 124 cm^{-1} for KZP and

modes at 85, 126 155 and 170 cm^{-1} for RbZP and 105, 134 and 168 cm^{-1} decrease with increase in pressure which marked as red lines. These modes are considered as soft modes.

In KZP, RbZP and CsZP the intensities of the same modes (internal modes of PO_4) as a function of pressure is different. This suggests orientational disorder of polyhedral ions which is known to cause amorphization. Above 10 GPa broadening of modes is rapid; several weak bands lose their identity and only three broad bands centered around 900, 950 and 1020 cm^{-1} are present, indicating pressure induced amorphisation. NZP was found to be stable up to 32 GPa but compounds with larger cationic size amorphized at gradually lower pressures.

It has been established that pressure induced decomposition can occur at a high temperature and high pressure condition if the daughter compounds occupy less volume than the parent compound.¹⁸



The volume of above daughter compounds are found to be less than the volume of parent compound indicating possible decomposition at high temperature and high pressure conditions. On the other hand all these compounds exhibit pressure induced amorphisation at ambient temperature. Amorphisation in these compounds might be due to kinetic hindrance of equilibrium decomposition.

4.3.2. Computation of phonon dispersion curves and bulk moduli

The phonon dispersion curves for KZP, RbZP and CsZP are computed at equilibrium volume and eigen frequencies for the various modes were obtained by diagonalizing the dynamical matrix using VASP. The computed zone centre Raman phonon frequencies are close to the experimental values (Table 4.1, 4.2, 4.3 and 4.4). The total irreducible representation obtained from computations is found to be

consistent with the results of group theoretical analysis described earlier. Computed atomic displacements for the lowest energy soft Raman mode for all compounds shows a combination of Zr translation and PO₄ librations (Figure 4.5 (a)). Other soft Raman modes show coupled rotation of ZrO₆ and PO₄ polyhedra with different displacements when the cations are changed (Figure 4.5(b) for RbZP and CsZP). The number of soft Raman modes increases with increase in size of alkali cation up to Rb and decreases with substitution of Cs indicating its hindrance to coupled rotation of PO₄ and ZrO₆ polyhedra.

The mode corresponding to 159 cm⁻¹ in RbZP shows the highest amplitude of displacement in a coupled rotation of ZrO₆ and PO₄ polyhedra compared to 155 cm⁻¹ in KZP (Figure 4.5 (c)). This mode in RbZP contributes significantly to contraction along the *a*-axis with negative Gruneisen parameter (-1.3) while the same mode in KZP exhibits a slight positive Gruneisen parameter (0.5). The soft modes in these compounds are not restricted to one specific type of vibration instead they are observed as combined movements of PO₄ and ZrO₆ polyhedra similar to the role played by WO₄ in Zr(WO₄)₂¹⁹ and MO₄ in Sc₂(MO₄)₃.⁷ This could be due to larger cations causing strain along the *c*-axis; further expansion with temperature is suppressed by the bridging PO₄ tetrahedra which consequently contracts along the *a*-axis by an increase in of O-P-O bond angles.² Hence, vibrational modes associated with the combined movement of bridging PO₄ tetrahedra and ZrO₆ octahedra can be readily related to contraction along the *a*-axis with temperature. Figure 4.5(d) shows the translation vibration of Na and Cs atoms contributing to positive thermal expansion with comparatively less amplitude of displacement in CsZP than NZP.

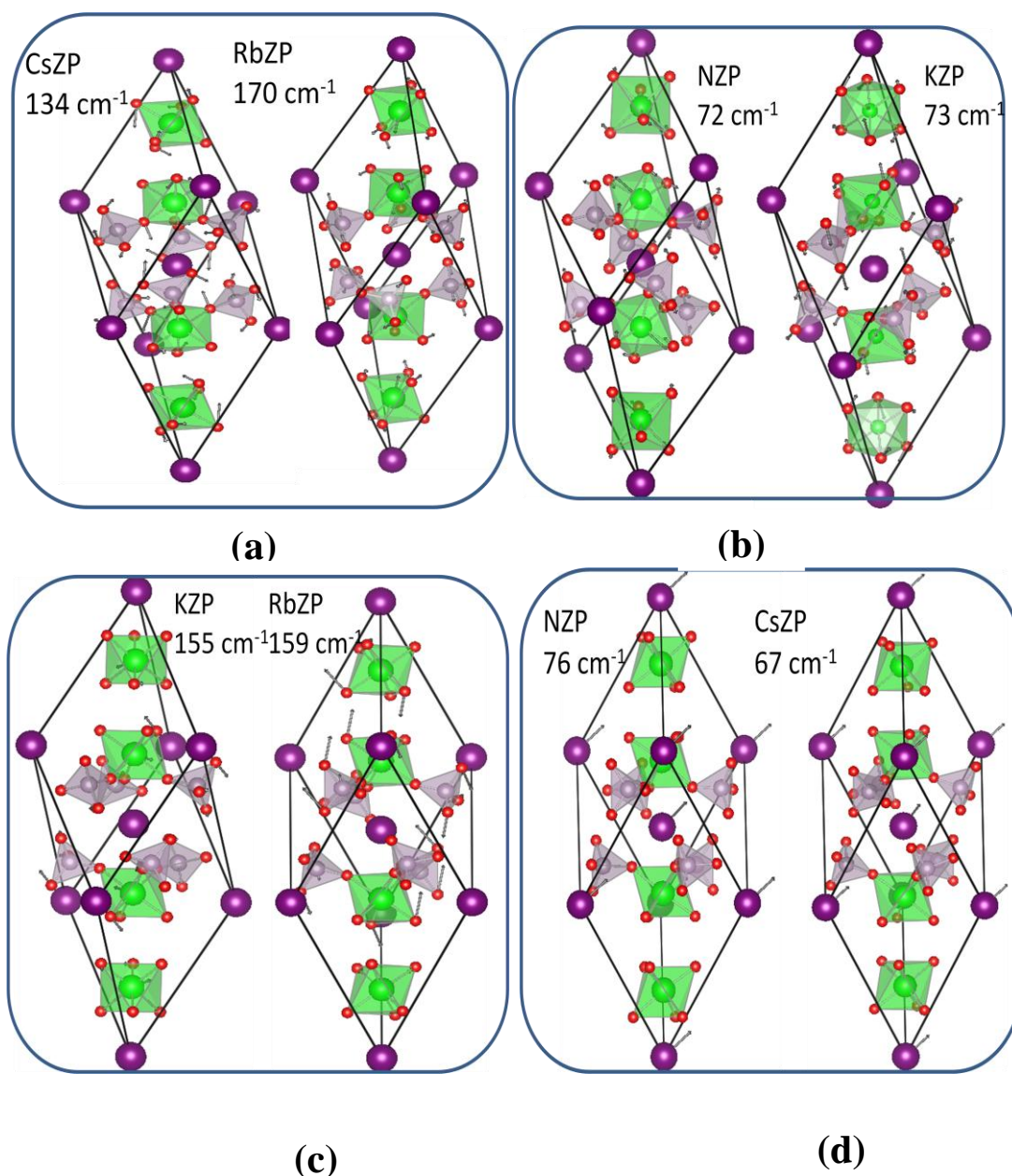


Figure 4.5 Atomic displacements of (a) the 72 cm⁻¹ mode of NZP and 73 cm⁻¹ of KZP showing Zr translation and PO₄ librations (b) the 134 cm⁻¹ mode of CsZP and 170 cm⁻¹ of RbZP showing coupled rotation of PO₄ tetrahedra and ZrO₆ octahedra (c) the 159 cm⁻¹ mode of RbZP exhibit maximum amplitude of displacement in coupled rotation of PO₄ tetrahedra and ZrO₆ octahedra than 155 cm⁻¹ in KZP (c) the 76 cm⁻¹ IR mode of NZP with Na translation shows large magnitude of displacement than 67 cm⁻¹ mode of CsZP with Cs translation.

Bulk moduli were computed for $\text{KZr}_2(\text{PO}_4)_3$, $\text{RbZr}_2(\text{PO}_4)_3$ and $\text{CsZr}_2(\text{PO}_4)_3$ by fitting the DFT calculated energy vs. volume data to the Birch third order equation of state. The bulk modulus for NZP, KZP, RbZP and CsZP are found to be 80, 112,

115 and 113 GPa respectively with pressure derivative $B_0' = 4$. The experimental bulk modulus for NZP is reported to be 53 GPa.⁹ The deviation of the computed bulk modulus of NZP from experiment are likely to be due to the difference between the experimental volume (507.88 \AA^3) and the calculated volume (528.66 \AA^3) similar to the case of scandium oxide.²⁰ Compressibility decreases significantly from NZP to KZP and remains constant with further increase in size of alkali cation. Compression mechanism in NZP type of ceramic compounds is explained by co operative interaction of bond compression and bond angle bending.²¹

4.3.3. Temperature dependent Raman studies

Figure 4.1 (a, b and c) shows the Raman spectra of $AZr_2(PO_4)_3$, A= K, Rb and Cs at different temperatures over the complete range of phonon frequencies. Frequencies of most of the modes decrease as a function of temperature, but the modes around 72, 110, 120, 155 and 420 cm^{-1} exhibit opposite behavior. The change in the phonon mode frequencies as a function of temperature at constant pressure occurs due to true anharmonicity (change in phonon occupation number) and quasiharmonicity (change in volume). These two effects are decoupled in the eq. (1.5).²¹

Quasiharmonic term is found from reported thermal expansion coefficients¹ and mode Gruneisen parameter. Mode Gruneisen parameters (γ_i) were obtained from pressure coefficients and the computed bulk modulus. Tables 1, 2, 3 and 4 show the contribution of the two terms for NZP, KZP, RbZP and CsZP respectively. On comparison of quasiharmonic term in Table 4.1, it is seen that Raman modes with frequencies 72 and 112 cm^{-1} in NZP, 73 and 120 cm^{-1} in KZP, 85, 126 and 159 and 170 cm^{-1} in RbZP and 105, 134 and 168 cm^{-1} in CsZP give rise to contraction with

temperature. With substitution of larger cations, magnitude of positive contribution is found to decrease which in turn lowers thermal expansion anisotropy. The first Raman band of all compounds shows maximum temperature dependence. Bands around 400 cm^{-1} (Table 4.1, 4.2, 4.3 and 4.4) corresponding to bending modes of PO_4 were found to be rigid, exhibiting positive temperature coefficient. Positive temperature coefficients occur if the potential wells for atomic vibrations (at constant volume) become steeper at higher temperature (a positive quartic term in the potential), making the force constants stiffer. The increase in the frequency with temperature essentially results from the cubic and/or quartic anharmonic part of the phonon potential, which is able to explain the temperature dependence of bending modes of PO_4 unlike the low-energy modes in the case of ZrW_2O_8 .²² The above mentioned low energy Raman bands which arise due to Zr translation and PO_4 libration and coupled rotation of PO_4 and ZrO_6 polyhedra has both maximum volume (thermal expansion) and amplitude contribution (pure temperature effect).

Phonon frequency shift and broadening can be analysed by considering phonon-phonon interactions. Explicit term in eq. (1.5) can be broken up into

$$\frac{1}{\omega_i} \left. \frac{d\omega_i}{dT} \right|_V = \Delta_3 + \Delta_4 \quad (4.2)$$

Implicit term can be written as

$$-\gamma_i \alpha = \Delta_E \quad (4.3)$$

Where Δ_3 and Δ_4 are the contributions of cubic and quartic anharmonicities respectively. Considering phonon-phonon interactions, anharmonic contributions to

phonon self-energy have a real phonon frequency shift (Δ) and imaginary phonon life time (Γ).²³ Eq. (1) can be written as,

$$\Delta = \Delta_3 + \Delta_4 + \Delta_E \quad (4.4)$$

$$\Gamma = \Delta_3 + \Delta_4 \quad (4.5)$$

Δ_E corresponds to frequency shift produced by thermal expansion. In the simplest anharmonic approximation, the phonons decay into two channels namely, the three-phonon and four phonon interactions through three phonon coupling is based on Klemens approach.²⁴ The temperature dependence of Raman frequency shift is

$$\Delta(T) = \Delta_0 + C \left[1 + \frac{2}{e^x - 1} \right] + D \left[1 + \frac{3}{e^y - 1} + \frac{3}{(e^y - 1)^2} \right] \quad (4.6)$$

Where Δ_0 is the phonon frequency shift extrapolated 0 K, $x = \hbar\omega_0/2k_B T$ and $y = \hbar\omega_0/3k_B T$. C and D are fitting parameters for three-phonon and four-phonon process. The underlying theory²⁵ of eq. (4.6) refers to anharmonic decay of a phonon into other phonons of lower frequencies; that is it corresponds to Raman modes which soften with increasing temperature. Hence, such a fitting has no physical meaning for above mentioned low frequency Raman modes and modes around 400 cm^{-1} whose true anharmonicity (maximum temperature dependence) values are large (Figure 4.6 (a, b)). Moreover, the compounds of NZP family are stable with temperature, so they cannot be attributed to unstable soft phonons associated with a phase transition. Explicit anharmonicity contributions due to cubic and quartic forms for modes around 1020 cm^{-1} for four different cations fitted using eq. (4.6) are shown in Figure 4.6 (c). From the fitted parameters, it is recognized that quartic anharmonicity has significant contribution.

The three phonon process for decay of an optical phonon at the Γ -point is relatively simple and yields a linear temperature dependence of line width broadening of Raman spectrum. If one considers four-phonon processes, the temperature dependence becomes more complex and an analogous expression to eq. (4.6) for the temperature dependence of Raman peak linewidth has been obtained by replacing Δ_0 by Γ_0 where Γ_0 is the FWHM extrapolated to 0 K.²³ Anharmonicity constants C and D terms are replaced by A and B that correspond to symmetrical decay of 3-phonon and 4-phonon process. Line width is expressed in terms of anharmonic coupling only and does not depend on the thermal expansion contribution. Figure 4.6 (d, e, f) shows the variation of line width with temperature for modes like 72 (both volume and pure temperature contribution), 420 (only temperature contribution) and 1020 cm^{-1} (usual softening with temperature). Line widths have been corrected for the instrumental resolution following a procedure described elsewhere.²⁶

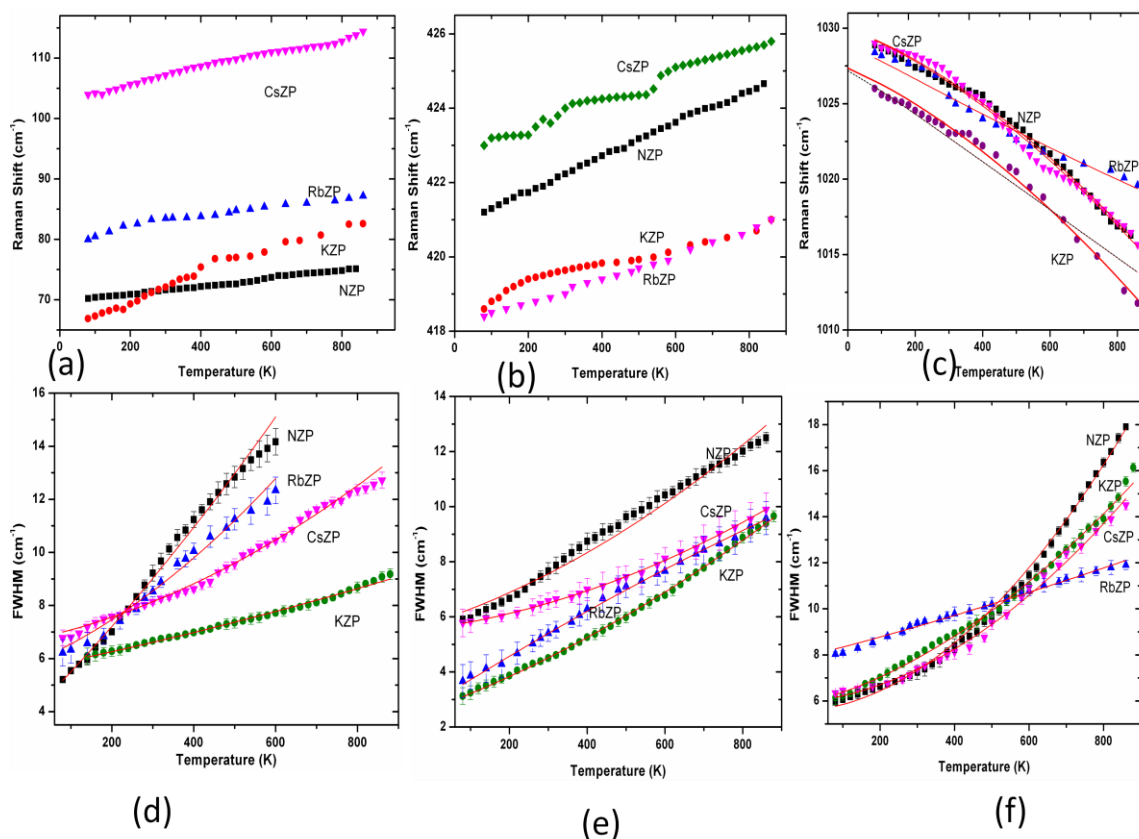


Figure 4.6 Temperature variation of (a) Raman shift of modes corresponding to 72 (NZP), 73 (KZP), 85 (RbZP) and 105 cm^{-1} (CsZP) shows abnormal hardening behaviour (b) Raman shift of modes corresponding to 422 (NZP), 419 (KZP), 421 (RbZP) and 423 cm^{-1} (CsZP) with bending vibration of PO_4 also shows abnormal hardening behaviour (c) Raman shift of modes corresponding to 1026 (NZP), 1023 (KZP), 1028 (RbZP) and 1025 cm^{-1} (CsZP) with symmetric stretching vibration of PO_4 shows usual softening. The data points are fitted using eq. (4.6) to determine cubic and quartic anharmonicity constants (red solid line). Black dotted line for 1023 (KZP) is fitted with only cubic term in eq. (4.6). (linear fit) which shows significant deviation from experimental points. (d) FWHM for modes corresponding to 72 (NZP), 73 (KZP), 85 (RbZP) and 105 cm^{-1} (CsZP) are fitted using eq. (4.6) to determine cubic and quartic anharmonicity constants (red solid line) (e) FWHM for modes corresponding to 422 (NZP), 419 (KZP), 421 (RbZP) and 423 cm^{-1} (CsZP) are fitted using eq. (4.6) to determine cubic and quartic anharmonicity constants (red solid line) (f) FWHM for modes corresponding to 1026 (NZP), 1023 (KZP), 1028 (RbZP) and 1025 cm^{-1} (CsZP) are fitted using eq. (4.6) to determine cubic and quartic anharmonicity constants (red solid line).

Table 4.5 shows the fitting parameters for both line widths and frequency shifts. The Raman bands at 420 cm^{-1} show large peak broadenings and hardening

with respect to temperature suggest there are important effects from explicit anharmonicity.

Table 4.5 Coefficients of cubic and quartic anharmonicities obtained from the analysis of the line width and phonon frequency shift with variation of temperature using eq.(4.6). Γ_0 and ω_0 represent line width and phonon frequency at 0K (extrapolated from 80 K in Figure 4.6), and their corresponding fitting parameters using eq. 4.6.

Mode frequencies 300 K at (cm^{-1})	Γ_0 (cm^{-1})	A	B	ω_0 (cm^{-1})	C	D
NZP						
72	3.88(2)	0.064(1)	0.000051(1)			
420	5.73(1)	0.117(7)	0.0014(2)			
1020	5.49(2)	0.122(3)	0.031(7)	1029.4(2)	-0.457(2)	-0.020(1)
KZP						
74	5.66(2)	0.010 (1)	0.000008			
419	2.64(2)	0.127(1)	0.0010			
1024	6.10(2)	0.18(1)	0.0178(6)	1027.6(2)	-0.628(2)	-0.018(1)
RbZP						
85	5.74(2)	0.030(2)	0.000097			
422	2.85(2)	0.211(2)	0.00041			
1019	7.83(1)	0.26(1)	0.00018	1021.0(2)	-0.455(3)	-0.018(2)
CsZP						
105	6.72(2)	0.011(5)	0.00004(1)			
423	5.6(1)	0.049(2)	0.0012(4)			
1025	5.89(1)	0.116(4)	0.0199(8)	1030.0(2)	-0.58(2)	-0.019(2)

The line width for the mode at 72 cm^{-1} with largest value of true anharmonicity is expected to show large quartic fitting parameter (B) but shows least value. This approach often gives good fits to experimental data, but the results can be misleading owing to the oversimplified approximation.

4.4. Summary and Conclusion

Raman spectra were measured on $A\text{Zr}_2(\text{PO}_4)_3$, $A = \text{Na, K, Rb, Cs}$ at temperatures to 860 K and pressures up to 25 GPa. Phase stability of these compounds at high pressure is discussed with respect to phase transformation and pressure induced amorphisation. The pressure and temperature dependence of the Raman peak shifts were used to separate the anharmonic contribution to thermal expansion from quasiharmonic contribution. VASP computed atomic displacements for these NTE modes shows combined movement of PO_4 tetrahedra and ZrO_6 octahedra unlike in other NTE compounds with specific single type of vibration. Apart from low frequency translational and librational modes, several other bending modes of phosphate ions are found to be strongly anharmonic. Raman modes above the high pressure phase transition exhibit normal positive pressure coefficient that would result in positive thermal expansion.

4.5. References

- ¹ T. Ota and I. Yamai, *J. Ceram. Soc. Jpn.* **95**, 531 (1987).
- ² T. Oota and I. Yamai, *J. Am. Ceram. Soc.* **69**, 1 (1986).
- ³ P. Tarte, A. Rulmont and C. Merckaert-Ansay, *Spectrochimica Acta A*, **42**, 10 (1986).
- ⁴ K. Kamali, T. R. Ravindran, C. Ravi, Y. Sorb, N. Subramanian and A. K. Arora, *Phys. Rev. B* **86**, 144301 (2012).
- ⁵ A. K. Arora, T. R. Ravindran and S. Chandra, *J. Phys.: Condens. Matter* **19**, 226210 (2007).
- ⁶ H. K. Poswal, A. K. Tyagi, A. Lausi, S. K. Deb and S. M. Sharma, *J Solid State Chem.* **182**, 136 (2009).
- ⁷ T. R. Ravindran, V. Sivasubramanian and A. K. Arora, *J. Phys.: Condens. Matter* **17**, 277 (2003).
- ⁸ V. I. Petkov, E. A. Asabina, A. V. Markin, N. N. Smirnova and D. B. Kitaev, *J. Therm. Anal. Cal.* **80**, 695 (2005).
- ⁹ K. Kamali, T. R. Ravindran, K. K. Pandey, S. M. Sharma and N. V. Chandra Shekar, *J. Solid State Chem.* **221**, 225 (2015).
- ¹⁰ V. I. Petkov, A. I. Orlova and O. V. Egorkova, *J. Struct. Chem.* **37**, 993 (1996).
- ¹¹ G. Kresse and J. Hafner, *Phys Rev. B* **47**, 558 (1993).
- ¹² G. Kresse and J. Hafner, *Phys. Rev. B* **49**, 14251 (1991).
- ¹³ G. Kresse and J. Furthmuller, *Phys. Rev. B* **54**, 11169 (1996).
- ¹⁴ L. O. Hagman and P. Kierkegaard, *Acta Chem. Scand.* **22**, 1822 (1968).
- ¹⁵ A. Togo, F. Oba and I. Tanaka, *Phys. Rev. B* **78**, 134106 (2008).
- ¹⁶ K. Momma and F. Izumi, *J. Appl. Crystallogr.* **41**, 653 (2008).

- ¹⁷ R. M. Hazen, D. C. Palmer, L. W. Finger and G. D. Stucky, *J. Phys.: Condens. Matter* **6**, 1333 (1994).
- ¹⁸ A. K. Arora, *Solid State Commun.* **115**, 665 (2000).
- ¹⁹ T. R. Ravindran, A. K. Arora and T. A. Mary *J. Phys.: Condens. Matter* **13**, 11573 (2001).
- ²⁰ S. Barzilai, I. Halevy and O. Yeheskal, *J. Appl. Phys.* **110**, 043532 (2011).
- ²¹ R. M. Hazen, 1982 *Comparative Crystal Chemistry*, New York: Wiley.
- ²² M. K. Gupta, R. Mittal and S. L. Chaplot, *Phys. Rev. B* **88**, 014303 (2013).
- ²³ T. Lan, X. Tang and B. Fultz *Phys. Rev. B* **85**, 094305 (2012).
- ²⁴ P. G. Klemens *Phys. Rev. B* **148**, 845 (1966).
- ²⁵ M. Balkanski, R. F. Wallis and E. Haro, *Phys. Rev. B* **28**, 1928 (1983)
- ²⁶ A. K. Arora and V. Umadevi, *Appl. Spectrosc.* **36** 424 (1982).

Chapter-5

High pressure Raman spectroscopic study of phase transformation in TaO₂F

5.1. Introduction

TaO₂F belongs to the broad Perovskite (ABX₃) family with vacant A sites and it crystallizes in cubic ReO₃ structure¹ with corner sharing Ta(O/F)₆ octahedra in which oxygen and fluorine atoms occupy the same (Wyckoff *d*) site. It exhibits isotropic, ultra-low thermal expansion coefficient of $6 \times 10^{-7} \text{ K}^{-1}$ from 20-400 K.³ This was attributed to thermally induced rocking of octahedral rigid unit modes involving transverse thermal motion of oxygen and fluorine atoms.³ Recently, pair distribution functions derived from total x-ray scattering measurements showed an average thermal expansion coefficient of -1 to $+1 \times 10^{-6} \text{ K}^{-1}$ between 100-380 K² and absence of significant negative thermal expansion (NTE) was shown to be due to the presence of geometrically distinct Ta-X-Ta links.² Well known NTE materials such as cubic ZrW₂O₈ and Zn(CN)₂ exhibit large isotropic NTE due to low energy rigid unit mode of WO₄ tetrahedral libration⁴ and translation mode of CN rigid unit⁵ respectively. Both these compounds amorphized around 2.2⁶ and 11 GPa⁷, whereas NaZr₂(PO₄)₃ (NZP), a low positive thermal expansion material that exhibits anisotropic thermal expansion shows no sign of amorphisation up to 20 GPa.⁸ Most of the NTE materials with framework structures amorphized at high pressures, but no such reports exist for TaO₂F.

The prototype ReO₃ does not exhibit NTE at room temperature but it was shown to exhibit NTE from 2-220 K and 600-680 K.⁹ ReO₃ synthesized by various routes was reported to show NTE due to static disorder.⁹ Oxygen displacement

parameters reveal that static disorder contribution is greater for samples with diminished NTE behavior.⁹ It exhibits a phase transformation of its cubic structure (*Pm-3m*) to another cubic structure (*Im-3*) at 0.5 GPa and then to a monoclinic phase around 3.1 GPa. At 13 GPa, it gets transformed into a rhombohedral phase of R-3c symmetry. At around 38 GPa, it further transforms into another rhombohedral phase and retains this structure up to 52 GPa. On decompression, it regains its ambient cubic structure.¹¹ Though no first order Raman bands are expected from symmetry considerations, cubic ReO₃ at ambient conditions shows defect induced broad Raman modes due to lowering of symmetry¹². Isostructural ScF₃ also shows strong NTE over the temperature range of 60-110 K due to thermally induced rocking of rigid structural units¹³ and a structural phase transition to R-3c at 0.6 GPa.¹⁴ At ambient conditions ScF₃ shows no Raman modes¹⁴ in accordance with symmetry selection rule indicating absence of disorder in the structure. NbO₂F with a similar structure shows rhombohedral phase transition (*R-3c*) around 0.5 GPa and pressure induced amorphisation above 18.5 GPa. The phase transition was shown to involve a slight distortion of Nb(O/F)₆ octahedra besides octahedral tilting¹⁴. Disorder in NbO₂F is due to one dimensional ordering of O and F atoms with significant static displacement of Nb from ideal cation site.¹⁶ High pressure XRD studies on TaO₂F reported two phase transitions around 0.7 and 4 GPa with the latter corresponding to a rhombohedral structure (*R-3c*)¹⁷. It also suggests the absence of isolated cubic grains and single phase of rhombohedral structure above 0.7 GPa¹⁷. But the phase between 0.7 and 4 GPa is ambiguous.

VF₃ type compounds (V=Al, Cr, Fe, Ga, In, Ti) at ambient conditions adopt rhombohedral structure (*R-3c*) and transform into cubic ReO₃ structure at elevated temperatures.¹⁹ High pressure investigations on TiF₃ and FeF₃ up to 7.6 and

9 GPa do not show any phase transition and the structure was characterized by cooperative tilting of octahedra.²⁰

The purpose of current study is to examine the behavior of the various phonon modes of TaO₂F at ambient condition and high pressures and temperatures using Raman spectroscopy, and to obtain more clarity on its structure in the intermediate pressure range of 0.7 to 4 GPa than was reported by high pressure x-ray diffraction studies.¹⁷

5.2. Experimental details

TaO₂F was synthesized by dissolving Ta metal powder in 48% HF in a Platinum crucible at 353 K. After evaporation to dryness, the powder was calcined at 573 K in air for 6 hrs.²¹ The final product is a fine white powder whose XRD pattern matches with JCPDS [PDF NO: 762370] data.

In-situ high pressure Raman spectra were recorded up to 19 GPa from a symmetric diamond anvil cell (DAC) with diamonds of culet diameter 500 μm , using a micro Raman spectrometer (Renishaw, UK, model inVia) with 488 nm laser excitation. The sample (~ 100 μm lateral dimensions) was loaded along with a few specks of ruby chips for pressure calibration and a 4:1 mixture of methanol-ethanol as pressure transmitting medium into a 200 μm hole drilled into a pre-intended stainless steel gasket. Pressure is hydrostatic up to 10 GPa in ethanol+methanol medium, after which it is quasihydrostatic up to ~ 20 GPa. Spectra were recorded in both increasing and decreasing pressure cycles. Temperature dependent Raman measurements were carried out from 80 K to 573 K at 20 K intervals using a heating and cooling microscope stage (Linkam THMS 600). IR spectrum of the sample, dispersed in CsI, was recorded using a BOMEM DA-8 FTIR spectrometer. Broad bands in Raman and IR spectra were resolved to determine peak positions using Peakfit software.

5.3. Results and discussion

TaO₂F crystallizes in a cubic Perovskite structure of space group $Pm-3m$ (O_h^1) with one formula unit per unit cell.¹ Factor group analysis was carried out to obtain total irreducible representation at the Brillouin zone center, $\Gamma_{\text{tot}}=2F_{1u}(\text{IR})+F_{2u}$ (silent) + F_{1u} (acoustic); i.e., no Raman active modes are expected for this structure.

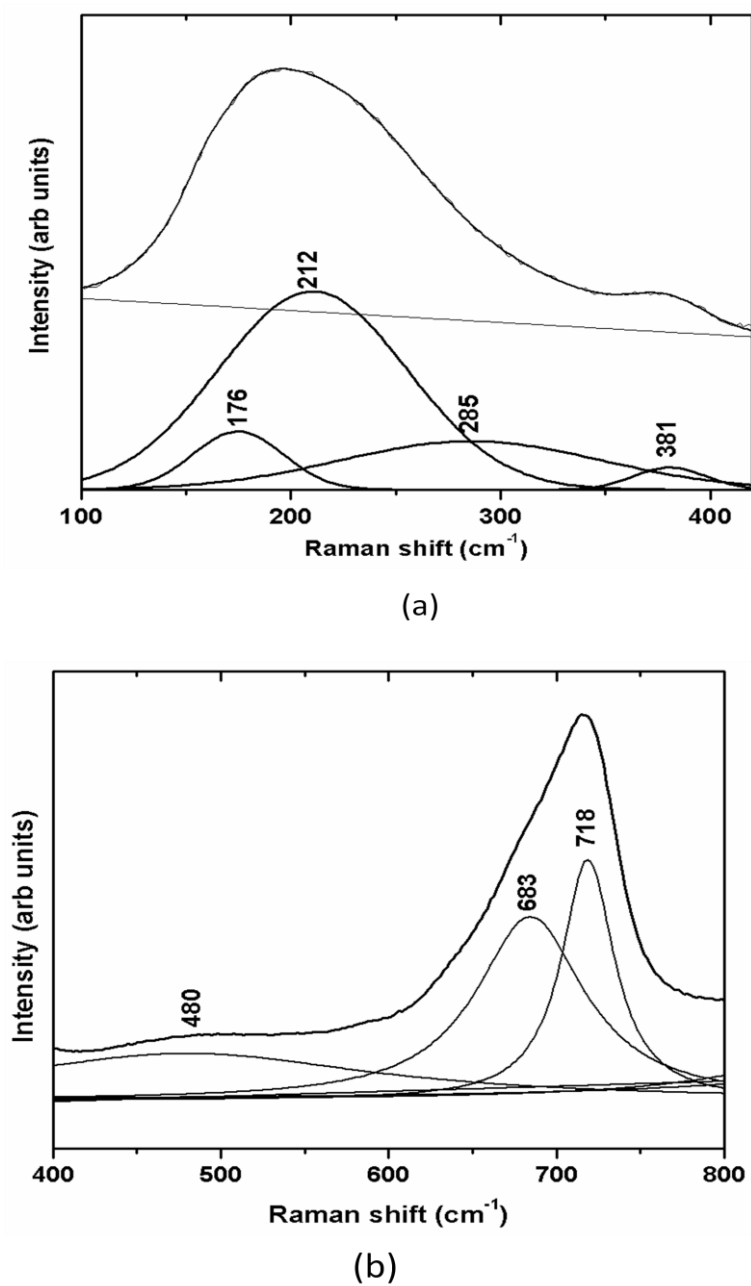
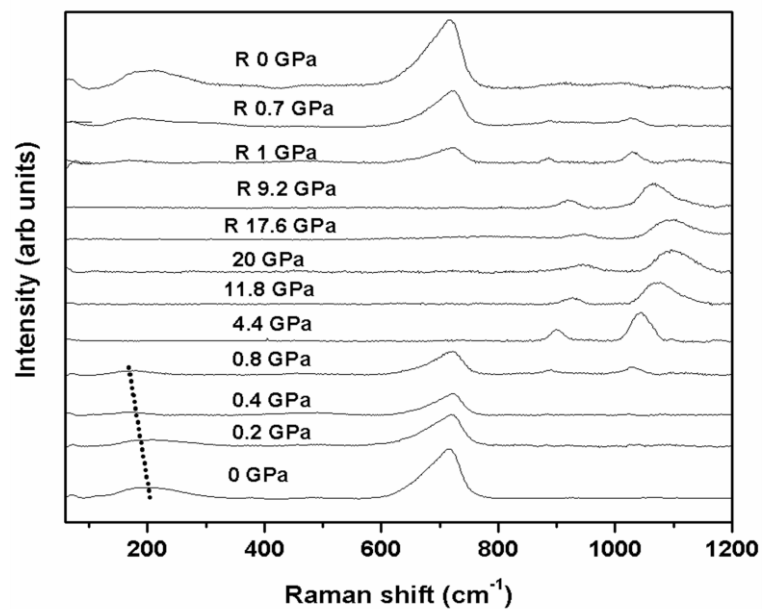


Figure 5.1 (a, b) Raman spectrum of TaO₂F at ambient conditions with peaks fitted using Peakfit software.

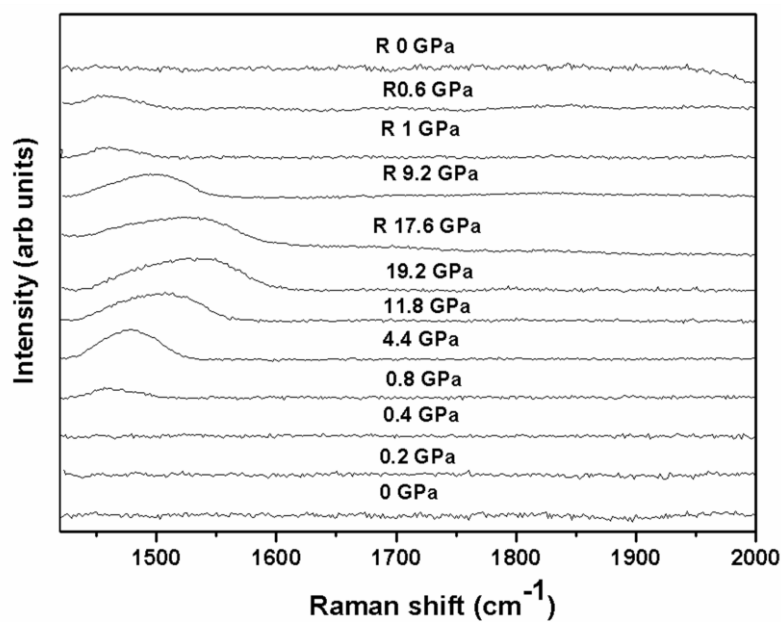
However, we do obtain several broad Raman bands of TaO₂F at ambient conditions with maxima near 200, 385 and 700 cm⁻¹ (Figure 5.1). They could either be second order Raman bands, or some of them could be first order bands that could arise due to static or dynamic disorder in anion and/or metal sublattice which would relax the local symmetry constraints and allow disorder induced first order Raman spectrum.²⁵ Recently, a cubic 3×3×3 supercell modeled with different Ta-O and Ta-F bond distances and O/F off-axis displacements was found to result in a better matching with experimental pair distribution functions at 80 K than from perfect cubic ReO₃ model with random distribution of O and F atoms below $r = 8 \text{ \AA}^3$. This is found to be due to strains associated with the disordered arrangement of geometrically distinct Ta-O-Ta and Ta-F-Ta links leading to local distortions away from the ideal structure of TaO₂F.² In TaO₂F, O/F atoms appear to occupy sites along the Ta...Ta axes only on average but in practice these sites are at potential energy maxima. The potential energy minima for O/F anions are located away from the Ta...Ta axes, giving rise to local distortion of the structure at ambient conditions. Tao *et al*³ termed the disorder as static because of higher displacement of Ta and transverse anions at low temperature. The consequence of anionic (O/F) disorder is to disrupt the inversion symmetry and allow first order Raman scattering at ambient pressure as proposed by Porto *et al* for BaTiO₃.²⁶ Hence disorder induced first order Raman bands are due to transverse motion of Ta-O-Ta and Ta-F-Ta. On resolving the broad bands, seven modes (Figure 1) were obtained due to lifting of degeneracy.

High pressure XRD on TaO₂F shows two phase transitions around 4 and 0.7 GPa with single phase rhombohedral structure above 4 GPa on decompression but the structure between 4 and 0.7 GPa remained unclear.¹⁷ High pressure Raman spectroscopic studies were carried out to get more insight into the structural

transitions. Factor group analysis was carried out to obtain the irreducible representation for the $R-3c$ structure at the zone center: $\Gamma_{\text{tot}}=A_{1g} + 3E_g + 2A_{1u} + 5E_u + 2A_{2g} + 3A_{2u}$; four modes ($A_{1g} + 3E_g$) are Raman active, six ($4E_u + 2A_{2u}$) IR active and others are silent.



(a)



(b)

Figure 5.2 Raman spectra at various pressures both in increasing and decreasing pressure cycles. Dotted line indicates the softening of 200 cm⁻¹ band with increasing pressure.

Figure 5.2 shows Raman spectra on both increasing and decreasing pressure cycles. The Raman bands at ambient conditions could be resolved into 7 components and followed as a function of pressure. Three distinct additional bands around 890, 1045 and 1426 cm^{-1} appear at 0.8 GPa whose intensities increase on further compression. The intensities of broad bands around 200 and 700 cm^{-1} gradually fall and disappear around 4 GPa along with the appearance of a new mode at 1091 cm^{-1} and thus all four group theoretically predicted modes corresponding to $R-3c$ structure are evident at 4.4 GPa (Figures. 5.2 and 5.3). This indicates that pressure could force the atoms back to their average positions and result in disappearance of broad band spectrum. These results indicate the onset of phase transition at 0.8 GPa and its completion around 4.4 GPa with the complete disappearance of the disorder-induced bands corresponding to the cubic phase. ω vs. P plot (Figure 5.3) clearly shows the disordered cubic (c) to disorder free rhombohedral (r) phase transition around 4.4 GPa and TaO_2F exists as a mixed (cubic+rhombohedral) phase in the pressure region 0.7 to 4 GPa.

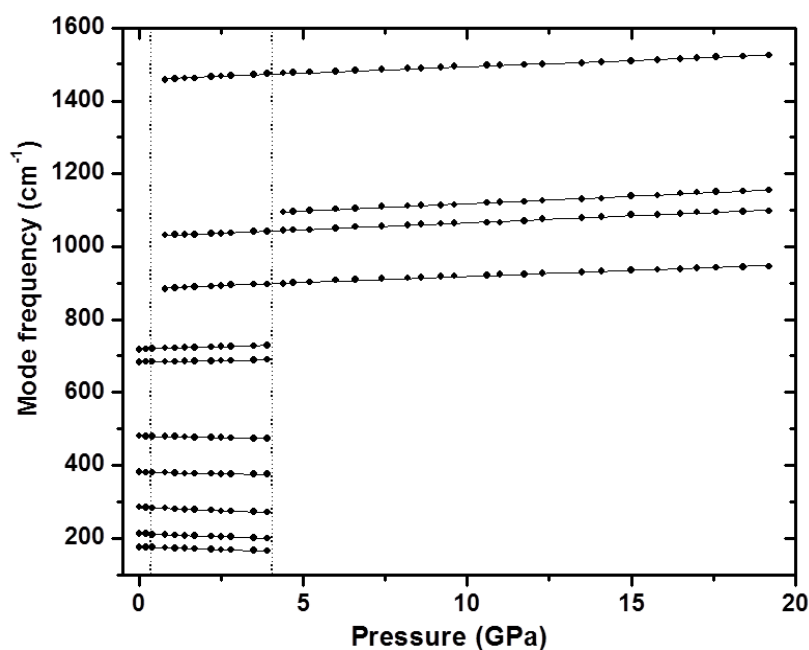


Figure 5.3 Frequency vs Pressure plot showing clear phase transition at 0.8 GPa.

Transition pressures for compounds of perfect cubic ReO_3 family were around 0.5-1 GPa and locally disordered TaO_2F also exhibits phase transformation around 0.8 GPa. This indicates the dominant role of repulsive interaction between cations to induce distortion in metal anion octahedra and deform to VF_3 type structure at 0.8 GPa. Geometrically distinct Ta-O-Ta and Ta-F-Ta links cause strain in local structure and which persist up to 4 GPa on compression. In high pressure XRD,¹⁷ isolated cubic grains did not show up above 0.7 GPa since XRD probes long range structures and could be ineffective if the grains are submicron sized whereas Raman spectroscopy is a local probe that can detect such domains.¹⁷

All Raman bands exhibit low positive Gruneisen parameter except the ones at 176, 212, 285, 381 and 485 cm^{-1} that soften with increase in pressure, i.e., they contribute negatively to the average thermal expansion. Table 5.1 lists the mode Gruneisen parameters for the seven observed Raman bands in the cubic phase.

Table 5.1 Gruneisen parameters for both disordered cubic phase and rhombohedral phase are obtained using the expression: $(B_0/\omega_i) (d\omega/dP)$, $B_0=36$ GPa for cubic phase and $B_0= 60$ GPa for VF_3 phase.¹⁷

Disordered cubic phase			VF_3 structure phase		
ω (cm^{-1})	$d\omega/dP$ ($\text{cm}^{-1}/\text{GPa}$)	γ_i	ω (cm^{-1})	$d\omega/dP(\text{cm}^{-1}/\text{GPa})$	γ_i
176	-2.77	-0.56(6)	884	3.32	0.22(5)
212	-3.04	-0.51(6)	1027	3.81	0.22(2)
285	-3.62	-0.45(7)	1077	4.06	0.22(4)
381	-1.56	-0.14(7)	1458	3.43	0.14(1)
480	-1.55	-0.11(6)			
683	1.55	0.08(2)			
718	2.68	0.13(4)			

The bulk modulus B_0 obtained from high pressure XRD data is 36 GPa.¹⁷ The equilibrium volume V_m is determined to be 3.56×10^{-5} m³/mole, average Gruneisen parameter $\gamma_{av} = -0.15$ and molar specific heat is $75 \text{ J mol}^{-1} \text{ K}^{-1}$. To account for the nine (optical) degrees of freedom ($2F_{1u} + F_{2u}$), it is empirically assumed that p_i value for all modes except the last two modes at 683 and 718 cm⁻¹ is unity. For these modes p_i is taken as 2. The thermal expansion coefficient $\alpha = -2.91 \times 10^{-6} \text{ K}^{-1}$ calculated using eq. (1.6) is in fair agreement with the reported value α of range -1 to $+1 \times 10^{-6} / \text{K}$. The lower value of α could be due to the underestimation of γ_{av} : for example, the γ_{av} obtained from Raman modes in $\gamma\text{-Mg}_2\text{SiO}_4$ was found to be substantially lower than the actual value.²⁷

The typical *c*-TaO₂F structure is expected to have no Raman active vibrations, as all its atoms are in inversion symmetry sites. But, in *r*-TaO₂F, only Ta atom (site: $2b$, S_6) is in inversion symmetry site while O/F atoms are in C_2 ($6e$) sites. So, Raman spectrum of *r*-TaO₂F involves vibrations in which only oxygen and fluorine atoms move. The normal modes of *r*-TaO₂F mainly comprise of deformation of Ta-O/F-Ta bridges. Absence of modes in low wavenumber region suggests the vibrations of only O/F atoms. All modes in *r*-TaO₂F harden with increasing pressure, contributing to positive thermal expansion. Table 5.1 shows Gruneisen parameters obtained for both disordered cubic and rhombohedral phases.

High pressure transformation of NbO₂F was shown to be of $\bar{a}\bar{a}\bar{a}$ type in Glazer notation²⁸ for Perovskite tilt system and this corresponds to octahedral rotation around only one of the triad axes leading to cubic to rhombohedral ($R\text{-}3c$) phase transition.²⁹ Similar tilt mechanism could be responsible for rhombohedral phase transformation ($R\text{-}3c$) in isostructural TaO₂F. The rhombohedral structure is robust and persists up to 20 GPa whereas isostructural NbO₂F amorphises above 18.5 GPa. On

decompression, *r*-TaO₂F regains its original disordered cubic structure indicating reversibility of this phase transition. VF₃ type compounds (V=Al, Cr, Fe, Ga, In, Ti) at ambient conditions adopt rhombohedral structure (*R-3c*) and transform into cubic ReO₃ structure at elevated temperatures.¹⁹ Temperature dependent phase transition in VF₃ type compounds was reported to be ferroelastic (rhombohedral) to prototype (cubic) structure. In a similar way, TaO₂F which adopts VF₃ type structure at high pressure might have ferroelastic domains and reversibly transform to prototypic cubic phase at decreasing pressure cycle. Whether ferroelastic domains are present at high pressures in VF₃ type compounds is an interesting possibility for further study.

The present temperature dependent Raman study shows that the intensity of broad bands remains almost unchanged with increase in temperature. This indicates that disorder is static. Raman spectra at high temperatures from 80 K to 873 K are shown in Figure 5.4.

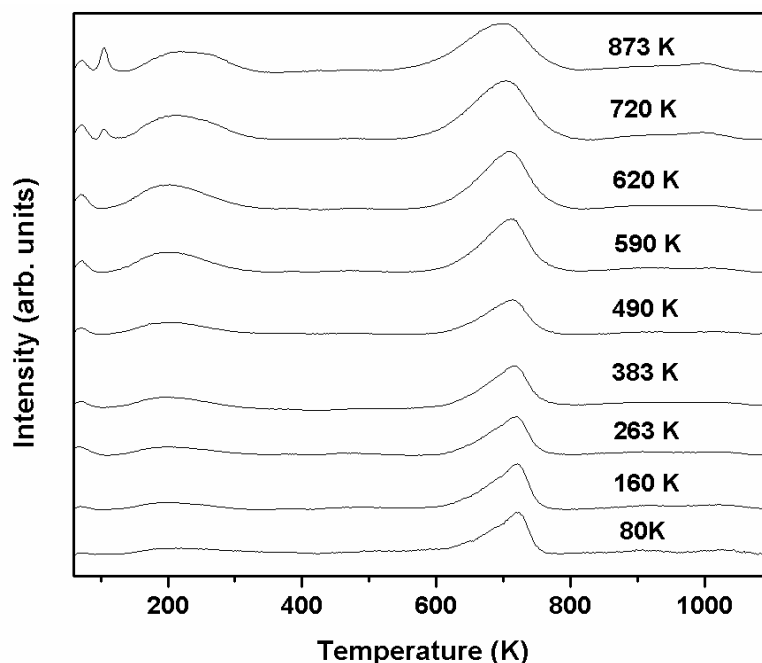


Figure 5.4 Raman spectra of TaO₂F in the temperature range 80 K to 873 K. Appearance of the mode at 106 cm⁻¹ indicates onset of decomposition to Ta₂O₅.

The compound decomposes to Ta_2O_5 above 773 K as reported earlier.¹ A new mode at 106 cm^{-1} indicates the onset of decomposition to Ta_2O_5 at 773 K¹. All Raman shifts of TaO_2F increase with decreasing temperature with gradual change in line widths. Freq vs. Temperature plot is shown in Figure 5.5. The $d\omega_i/dT$ values obtained by linear fits of this plot represent the total anharmonicities of the modes.

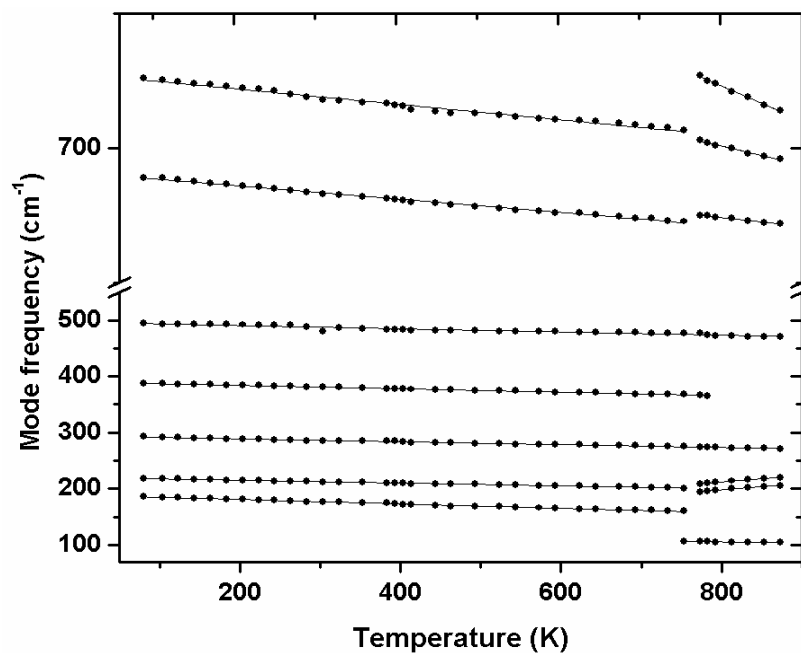


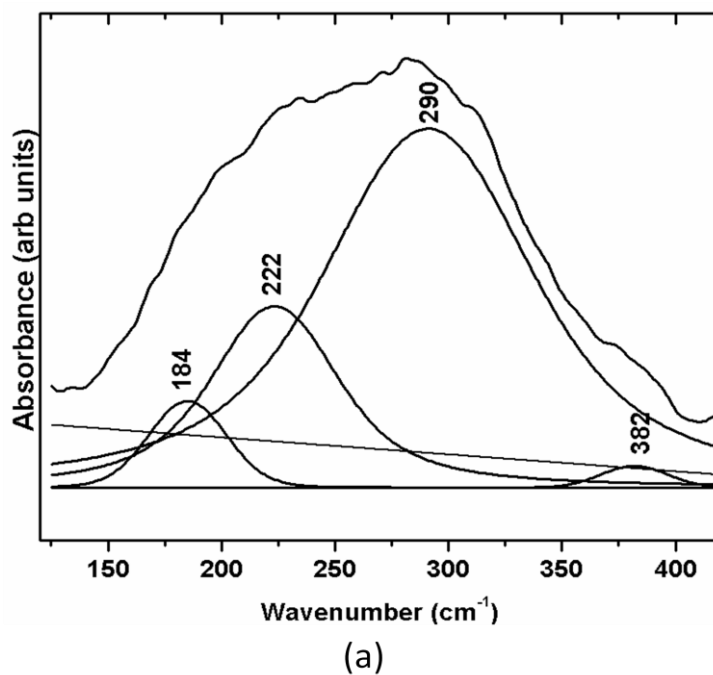
Figure 5.5 Temperature dependence of mode frequencies from 80 K to 873 K.

Static disorder of anions plays a significant role in ZTE behavior and hence Raman modes arise due to anionic disorder should also exhibit ZTE property. Variation of phonon frequency with temperature occurs due to anharmonicity of interatomic potential. Table 5.2 shows the true anharmonic and quasiharmonic parts for the seven Raman modes obtained using eq. (1.5).³⁰ The large magnitude of anharmonicity of mode at 176 cm^{-1} indicates maximum temperature dependence. Quasiharmonic contribution for all these modes is almost zero indicating ZTE behavior due to negligible change in lattice volume.

Table 5.2 Total anharmonicities, quasiharmonic and trueanharmonic contributions of different phonons in TaO₂F. The numbers in the parentheses are standard errors to the least significant digit. $\alpha=+1$ ppm K⁻¹

Mode frequency (cm ⁻¹)	Total anharmonic (10 ⁻⁵ K ⁻¹)	Quasiharmonic $\alpha\gamma_j$ (10 ⁻⁵ K ⁻¹)	Trueanharmonic (10 ⁻⁵ K ⁻¹)
176	-22	-0.0(5)	-22
212	-12(1)	-0.0(5)	-12(1)
285	-8.7(4)	-0.0(4)	-8.7(8)
381	-7.6(1)	-0.0(1)	-7.6(2)
480	-5.9(3)	-0.0(1)	-5.9(4)
683	-3.6(2)	0.0(1)	-3.6(3)
718	-3.8(6)	0.0(1)	-3.8(7)

Figure 5.6 (a, b) shows our recorded IR spectra of TaO₂F at ambient conditions in the range 100-1100 cm⁻¹.



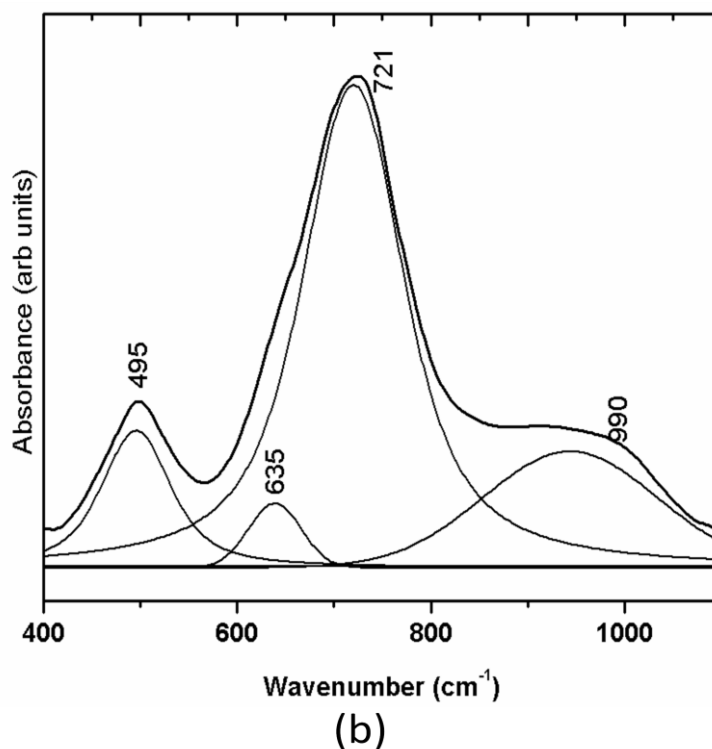


Figure 5.6 (a,b) IR absorption spectrum of TaO₂F at ambient conditions covering the range from 100-1100 cm⁻¹.

On resolving the whole IR spectrum, eight bands are obtained which is less than the expected nine ($2F_{1u} + F_{2u}$) optical degrees of freedom. Seven of these IR band frequencies are found to be in fair agreement with our Raman mode frequencies (Table 5.3).

Table 5.3 Comparison of Raman and IR mode frequencies in TaO₂F. Raman modes are active due to loss of center of symmetry. IR mode at 990 cm⁻¹ is found to be overtone of 495 cm⁻¹.

Raman mode frequencies (cm ⁻¹)	IR mode frequencies (cm ⁻¹)
176	184
212	222
285	290
381	382
480	495
683	635
718	721
--	990

We assign the eighth IR band at 990 cm⁻¹ to be an overtone of the one at 495 cm⁻¹ and hence we obtain only seven fundamental IR modes. Since anions (O/F) are displaced from the original cubic ReO₃ structure, local symmetry is altered due to loss of inversion symmetry and both Raman and IR modes are active.

5.4. Summary and conclusion

High pressure behavior of cubic TaO₂F is investigated up to 19.2 GPa using Raman spectroscopy. First order Raman bands arise due to distortion of cubic structure caused by disordered anions (O/F). Upon compression to 0.8 GPa, cubic to rhombohedral phase transition starts and completes at 4.4 GPa and retains the same structure up to 20 GPa. The rhombohedral structure reverts back to the original disordered cubic structure on decompression. Mode Gruneisen parameters in cubic

and rhombohedral phases are investigated. Five modes soften with increase in pressure and contribute negatively to the thermal expansion, resulting in nearly zero thermal expansion whereas all modes in the rhombohedral phase show positive Gruneisen parameter indicating positive average thermal expansion. The intensities of Raman bands remain unchanged with increase in temperature, indicating static disorder. Extreme broadness in IR spectrum also confirms the presence of local disorder in ambient condition in accordance with Raman spectroscopy.

5.5. References

- ¹L. K. Frevel, H. W. Rinn, *Acta Cryst.* **9**, 626 (1956).
- ²C. R. Morelock, B. K. Greve, M. Cetinkol, K. W. Chapman, P. J. Chupas and A. P. Wilkinson, *Chem. Mater.* **25**, 1900 (2013).
- ³J. Z. Tao and A. W. Sleight, *J. Solid State Chem.* **173**, 45 (2003).
- ⁴T. R. Ravindran, A. K. Arora and T. A. Mary, *Phys. Rev. Lett.* **84**, 3879 (2001).
- ⁵T. R. Ravindran, A. K. Arora, S. Chandra, M. C. Valsakumar and N. V. Chandra Shekar, *Phys. Rev. B* **76**, 054302-1 (2007).
- ⁶T. R. Ravindran, A. K. Arora and T. A. Mary, *J. Phys.: Condens. Matter* **13**, 11573 (2007).
- ⁷A. K. Arora, R. Nithya, T. Yagi, N. Miyajima and T. A. Mary, *Solid State. Commun.* **129**, 9 (2004).
- ⁸K. Kamali, T. R. Ravindran, C. Ravi, Y. Sorb, N. Subramanian and A. K. Arora, *Phys. Rev. B* **86**, 144301-1 (2012).
- ⁹T. Chatterji, T. C. Hansen, M. Brunelli and P. F. Henry, *App. Phys. Lett.* **94**, 241902-1 (2009).
- ¹⁰E. E. Rodriguez, A. Llobet, T. Proffen, B. C. Melot, R. Seshadri, P. B. Littlewood and A. K. Cheetham, *J. Appl. Phys.* **105**, 114901-1 (2009).
- ¹¹J. E. Jorgensen, J. S. Olsen and L. Gerward, *J. Appl. Crystallogr.* **33**, 279 (2000).
- ¹²J. Purans, A. Kuzmin, E. Cazzanelli and G. Mariotto, *J. Phys.: Condes. Matter* **19**, 226206 (2007).
- ¹³B. K. Greve, K. L. Martin, P. L. Lee, P. L. Chupas, K. W. Chapman and A. P. Wilkinson *J. Am. Chem. Soc.* **132**, 15496 (2010).
- ¹⁴K. S. Aleksandrov, N. V. Voronov, A. N. Vtyurin, A. S. Krylov, M. S. Molokeev, A. S. Oreshonkov, S. V. Goryainov, A. Yu. Likhacheva and A. I. Ancharov, *Physics of Solid State* **53**, 564 (2011).

- ¹⁵S. Carlson, A. K. Larsson and F. E. Rohrer, *Acta. Crystallogr. B* **56**, 189 (2000).
- ¹⁶F. J. Brink, R. L. Withers and L. Noren, *J. Solid State Chem.* **166**, 73 (2002).
- ¹⁷M. Cetinkol, A. P. Wilkinson, C. Lind, W. A. Bassett and C. S. Zha, *J. Phys. Chem. Solids* **68**, 611 (2007)
- ¹⁸L. F. Silva, W. Avansi, J. Andres, C. Ribeiro, M. L. Moreira, E. Longo and V. R. Mastelaro, *Phys. Chem. Chem. Phys.* **15**, 12386 (2013).
- ¹⁹A. Mogusmilankovic, J. Ravez, J. P. Chaminade and P. Hagenmuller, *Mater. Res. Bull.* **20**, 9 (1985).
- ²⁰H. Sowa and H. Ahsbabs, *Acta. Crystallogr. B* **54**, 578 (1998).
- ²¹S. Sawhill and E. Savrun, *Ceram. Int.* **38**, 1981 (2012).
- ²²H. K. Mao, P. M. Bell, J. W. Shaner and D. J. Steinberg, *J. Appl. Phys.* **49**, 3276 (1978).
- ²³A. Jayaraman, *Rev. Mod. Phys.* **55**, 65 (1983).
- ²⁴S. Klotz, J. –C. Chervin, P. Munsch and G. Le Marchand, *J. Phys. D: Appl. Phys.* **42**, 075413 (2009).
- ²⁵A. Grzechnik, G. H. Wolf and P. F. McMillan, *J. Raman. Spectrosc.* **28**, 885 (1997).
- ²⁶J. L. Verble, E. G. Lluesma and S. P. S. Porto, *J. Raman. Spec.* **7**, 7 (1978).
- ²⁷A. M. Hofmeister and H. K. Mao, *Proc. Natl. Acad. Sci.* **99**, 559 (2002).
- ²⁸A. M. Glazer, *Acta. Cryst. B* **28**, 3384 (1972).
- ²⁹S. Carlson, *J. Appl. Cryst.* **33**, 1175 (2000).
- ³⁰B. A. Weinstein, T. Zallen 1984 *Light Scattering in Solids IV*, Ed. M. Cardona and M. Guntherodt (Springer-Verlag, Berlin) p.463

Chapter 6

Negative linear compressibility and thermal expansion of $\text{KMn}[\text{Ag}(\text{CN})_2]_3$ studied by Raman spectroscopy and first-principles calculations

6.1. Introduction

Solids in general expand with temperature and shrink with pressure. However, many substances are known to exhibit anisotropic thermal expansion or linear compressibility or both.¹⁻²³ Goodwin et al^{14,15} have recently studied the thermal expansion and linear compressibility of $\text{Ag}_3[\text{Co}(\text{CN})_6]$ using x-ray and neutron diffraction and density functional theory calculations. They have shown that this material exhibits colossal positive and negative thermal expansion in different directions and a large negative linear compressibility. The trigonal crystal structure of $\text{Ag}_3[\text{Co}(\text{CN})_6]$ consists of alternating layers of Ag^+ and $[\text{Co}(\text{CN})_6]^{3-}$ ions, stacked parallel to the trigonal axis and strongly bonded Co-CN-Ag-NC-Co linkages running parallel to the $\langle 101 \rangle$ directions. This trigonal structure can be considered a three dimensional wine-rack and is topologically equivalent to three interpenetrating α -Po (cubic) nets.²¹ It exhibits NLC of $\chi_c = -75 \text{ TPa}^{-1}$ (along trigonal axis) by densification of wine-rack like framework through rapid compression of a and b crystal axes and expansion along c . Despite the magnitude of this NLC response, it is unlikely to find widespread application due to a shear instability at 0.2 GPa.¹⁵

The structure of $\text{KMn}[\text{Ag}(\text{CN})_2]_3$ is closely related to $\text{Ag}_3[\text{Co}(\text{CN})_6]$. The main difference is the inclusion of K^+ ions within the cavities of the dicyanometallate

framework, lowering the crystal symmetry from P-31m to P312. The coefficients of thermal expansion of $\text{KMn}[\text{Ag}(\text{CN})_2]_3$ ($\alpha_{a=}$ $+61 \times 10^{-6} \text{K}^{-1}$, $\alpha_{c=}$ $-60 \times 10^{-6} \text{K}^{-1}$) and the linear compressibilities ($\chi_{a=}$ $+33.2 \text{TPa}^{-1}$ and $\chi_{c=}$ -12TPa^{-1}) in the pressure range 0.2-2.2 GPa was shown to be due to the same hinging mechanism in wine-rack like structure.²¹ It shows a higher magnitude of NLC up to 2 GPa without any phase transformation,²¹ which makes it more suitable for applications since most machining processes subjects materials to pressures of 1-2 GPa²⁴. Cairns *et al* speculated that the pressure range is extended due to frustration of collapse of ambient framework caused by phase transition with inclusion of counter ions (K^+).²¹ The above speculation and stability at high pressures are yet to be verified with further studies.

Low energy vibrational modes play an important role in anomalous thermal expansion. We have computed the zone center phonon mode frequencies for $\text{KMn}[\text{Ag}(\text{CN})_2]_3$ and probed the anharmonicity of phonons responsible for anomalous thermal expansion coefficients. Elastic constants were calculated to illustrate the elastic properties of $\text{KMn}[\text{Ag}(\text{CN})_2]_3$.

In the present paper, we report our study of vibrational and elastic properties of $\text{KMn}[\text{Ag}(\text{CN})_2]_3$ using Raman spectroscopy and first-principles calculations. Raman modes assignment at ambient conditions is carried out using Polarized Raman spectroscopy. Anharmonicity analysis has been carried out for all Raman modes in order to calculate the contributions of pure volume (implicit) and pure temperature (explicit) effects to the total Raman shift observed at different temperatures. Density Functional Perturbation Theory (DFPT) calculations combined with the quasi-harmonic approximation was used to obtain the phonon spectrum and Gruniesen parameters for comparison with experimental values. Pressure variation of elastic

constants and average partial phonon frequencies gives insight into the large persistent negative linear compressibility of $\text{KMn}[\text{Ag}(\text{CN})_2]_3$ compared to $\text{Ag}_3[\text{Co}(\text{CN})_6]$. Experimental and computational techniques are described in the next section followed by analysis and discussion of possible mechanism for linear compressibility, thermal expansion and pressure induced phase transformation. We summarize our results in the final section.

6.2. Experimental and computational details

Single crystals of $\text{KMn}[\text{Ag}(\text{CN})_2]_3$ were grown by a layering technique, employing the procedure reported by Geiser *et al.*²⁴ We obtained crystals with typical dimensions of 0.6 mm×0.2 mm×0.03 mm.

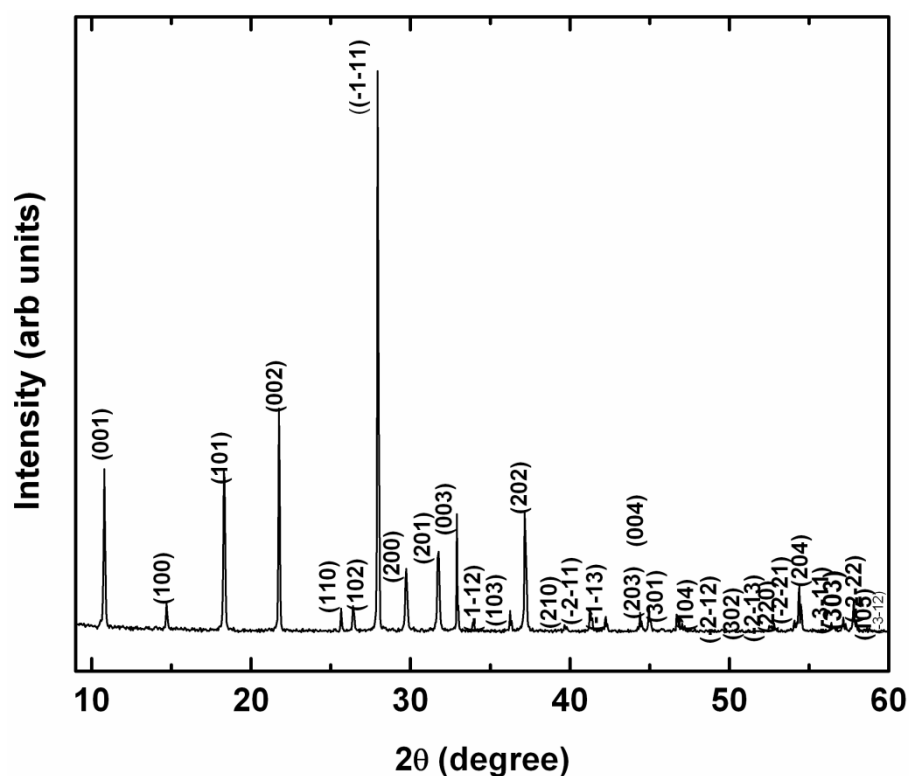


Figure 6.1 Powder XRD pattern of $\text{KMn}[\text{Ag}(\text{CN})_2]_3$ showing single phase.

A part of the sample was ground and characterized by x-ray powder diffraction, and the pattern is found to match with the JCPDS pattern of trigonal crystal structure [PDF NO: 04-011-0797] without any impurity peaks (Figure 6.1). Distinct colorless hexagonal plates were carefully handpicked and observed through a polarizing optical microscope under cross polarized condition. The crystals that appear dark and remain dark through 360° rotation are the ones with their crystallographic c -axis (i.e., the optic axis) perpendicular to the basal plane within the crystal [Figure 6.2].

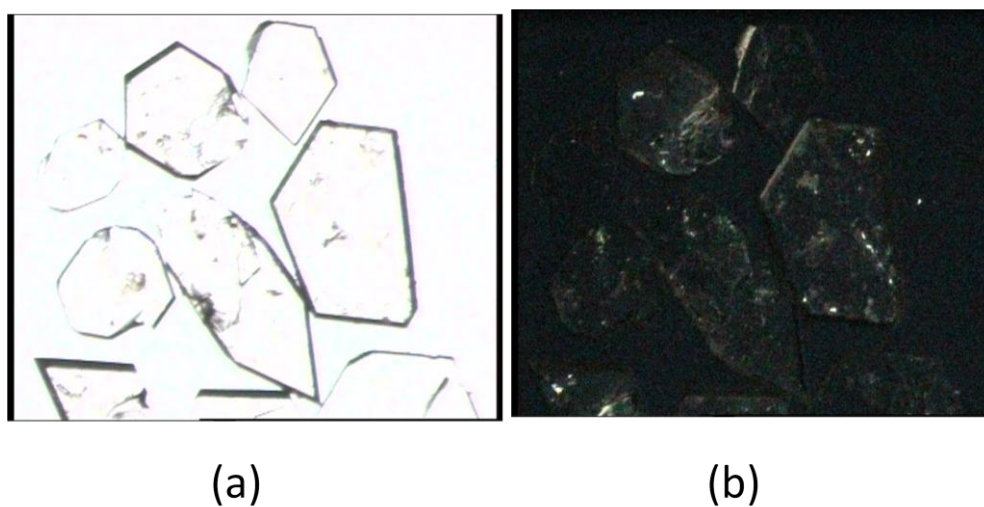


Figure 6.2 A few hexagonal shaped crystals (a); under cross-polarized condition (b).

Such c -oriented single crystals were then used in the polarized Raman measurements to assign the phonon modes. Spectra were measured at $T=80$ K in $Z(XX)Z'$ (VV) and $Z(XY)Z'$ (VH) scattering geometries (Porto's notation) where Z is the microscope axis, which is the direction of incident laser, Z' is the direction of the scattered signal, and X and Y are on the crystal plane.

In-situ high pressure Raman spectra were recorded up to 14 GPa at 0.5 GPa intervals from a symmetric diamond anvil cell with diamonds of 500 μm culet diameter, using a micro Raman spectrometer (Renishaw, UK, model inVia) with 514

nm laser excitation. The sample (~100 μm lateral dimensions) was loaded along with a few specks of ruby chips for pressure calibration and a 4:1 mixture of methanol-ethanol as pressure transmitting medium into a 200 μm hole drilled into a pre-intended stainless steel gasket. Pressure is hydrostatic up to 10 GPa in ethanol+methanol medium, after which it is quasihydrostatic up to ~20 GPa. The spectra were recorded in both increasing and decreasing pressure cycles. High pressure Raman experiments were also carried out without pressure transmitting medium under non hydrostatic condition. Temperature dependent Raman measurements were carried out from 80 K to 533 K at 20 K intervals using a heating and cooling microscope stage (Linkam THMS 600). Infra Red (IR) spectrum of the sample, dispersed in CsI, was recorded using a BOMEM DA-8 Fourier Transform IR (FTIR) spectrometer.

The isothermal linear compressibilities were computed using the principal axis strain calculator PASCAL²⁵. PASCAL determines linear compressibility by fitting the lattice parameters at different volumes and the corresponding pressures to the equation²³:

$$\chi_l = -\frac{1}{l} \left[\frac{dl}{dP} \right]_T \quad (6.1)$$

Here χ_l is the compressibility along axis l , P is the pressure and T , the temperature. We have also computed the linear compressibilities alternatively from elastic constants C_{ij} . For trigonal crystals, the compressibilities in basal plane and along the trigonal axis are given by the relations²⁶:

$$\chi_a = \frac{C_{33} - C_{13}}{C_{11} C_{33} - 2C_{13}^2 + C_{12} C_{33}} \quad (6.2)$$

$$\chi_c = \frac{C_{11} + C_{12} - 2C_{13}}{C_{11} C_{33} - 2C_{13}^2 + C_{12} C_{33}} \quad (6.3)$$

Similarly, the isotropic and linear bulk moduli are expressed in terms of elastic constants by the relations:

$$B_{iso} = \frac{\Lambda}{(2+\tau)^2}, \quad B_a = \frac{\Lambda}{(2+\tau)}, \quad B_c = \frac{B_a}{\tau} \quad (6.4)$$

Where $\Lambda = C_{11} + 2C_{12} + C_{22} + 2C_{13}\tau + C_{33}\tau^2 + 2C_{23}\tau$ and

$$\tau = \frac{C_{11} + C_{12} - 2C_{13}}{C_{33} - C_{13}}$$

The linear thermal expansion coefficients are computed within the theoretical framework given in Hermet *et al.*²⁶ For trigonal crystals, the different thermal expansion coefficients are given by:

$$\alpha_a = \frac{1}{V_0} \sum_{j,q} c_v(j,q) \left[\frac{1}{2} (s_{11} + s_{12}) \gamma_a + s_{13} \gamma_c \right] \quad (6.5)$$

$$\alpha_c = \frac{1}{V_0} \sum_{j,q} c_v(j,q) [s_{13} \gamma_a + s_{33} \gamma_c] \quad (6.6)$$

Here the s_{ij} are elastic compliances, obtained by inverting the elastic constant matrix C_{ij} and the mode specific heat $c_v(j,q)$ is calculated using Einstein's model.^{19,27} The directional Gruneisen parameters (γ_a and γ_c) are defined by the weighted sums over the mode Gruneisen parameters:

$$\gamma_k(j,q) = - \left(\frac{\partial \ln [\omega(j,q, \{a_k\})]}{\partial \ln a_k} \right)_0 \quad (6.7)$$

Where $\omega(j,q)$ is phonon frequency of mode j at wave vector q and a_k are lattice parameters.

First principles calculations of the pressure dependent lattice parameters, phonon spectrum and elastic constants were carried out using Vienna Ab initio Simulation Package (VASP).²⁸⁻³⁰ The equilibrium geometry of $\text{KMn}[\text{Ag}(\text{CN})_2]_3$ was computed with the crystallographic data from Geiser *et al.*²⁴ A plane-wave basis set with 550 eV cut-off was used to expand the electronic wave function. Projected Augmented Wave pseudopotentials^{31, 32} were used to represent the interaction of valence electrons with the ion core. Brilluoin zone integrations were performed on a $7 \times 7 \times 7$ Γ -centered Monkhorst-Pack³³ k -grid, with a Gaussian smearing width of $\sigma=0.05$. Ionic relaxation was stopped when all forces were converged to smaller than 1×10^{-6} eV/Å. With the computed equilibrium geometry, the zone-center phonon spectrum was calculated using the VASP implementation of DFPT. Details of DFPT calculations can be found elsewhere.^{34-37,19} The elastic constants were calculated using the symmetry-general least-squares method as implemented by VASP.³⁸ The elastic constants were derived from the strain-stress relationships obtained from six finite distortions of the lattice. The calculated elastic moduli include contributions of distortions with rigid ions and ionic relaxations.

6.3. Results and discussion

6.3.1. Polarized Raman and IR spectroscopy results

$\text{KMn}[\text{Ag}(\text{CN})_2]_3$ crystallizes in a trigonal structure with space group $P312 (D_3^1)$ with one formula unit in the crystallographic unit cell. The K, Mn, Ag atoms occupy the Wyckoff sites e , a and k respectively; C and N occupy the l sites.²⁴ Factor group analysis was carried out using Correlation method³⁹ to obtain the total irreducible representation, $\Gamma_{\text{tot}}=7A_1+10A_2+17E$, which comprises of internal modes of cyanide

ion $\Gamma_{\text{int}}=6A_1+6A_2+12E$, lattice modes $\Gamma_{\text{ext}}=A_1+3A_2+4E$ and acoustic modes $\Gamma_{\text{acoustic}}=A_2+E$. Therefore, 23 Raman active ($7A_1+16E$) and 25 IR active modes ($9A_2+16E$) are expected from the sample.

Figure 6.3 shows the polarized Raman spectra measured at 80 K. The allowed symmetry species for c -oriented hexagonal single crystals in $Z(\text{XX})Z'$ (VV) scattering geometry are A_1 and E ; in $Z(\text{XY})Z'$ (VH) scattering geometry, only E species is allowed. The bands at 63, 140, 189, 298, 332, 429 and 2168 cm^{-1} are found to appear in the VV but not in the VH geometry and hence they are assigned as A_1 symmetry species. The remaining modes that appear in both the VV and VH geometry are labelled as E modes. The frequencies and their mode assignments are given in Table 6.1.

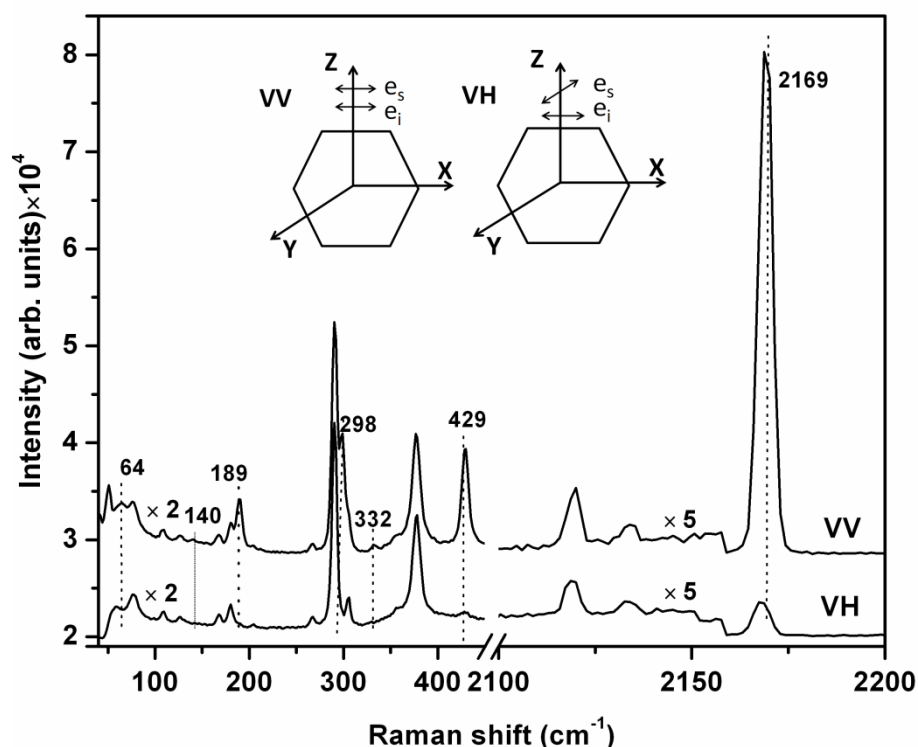


Figure 6.3 Polarized Raman spectra of $\text{KMn}[\text{Ag}(\text{CN})_2]_3$ in $Z(\text{XX})Z'$ (VV) and $Z(\text{XY})Z'$ (VH) scattering geometries at 80 K. Both A_1 and E modes appear in VV geometry. The labeled Raman modes that disappeared in the VH geometry are assigned as A_1 .

Table 6.1 Comparison of Raman and IR frequencies of $\text{KMn}[\text{Ag}(\text{CN})_2]_3$ and their mode assignments obtained using Polarised Raman measurements with the computed zone centre phonon frequencies and mode assignments. Mode Gruneisen parameters (γ_i) are also listed. Our DFPT calculations used vDW-DF2 and rPW86 exchange-correlation functional. Mode descriptions are obtained by visualizing atomic displacements using VESTA.

Experimental				DFPT with vDW-DF2 and rPW86			
Raman modes at 80 K (cm^{-1})	Mode label	IR modes at 300 K (cm^{-1})	Mode Gruneisen parameter (γ_i)	Zone center modes (cm^{-1})	Mode Gruneisen parameter (γ_i)	Mode label	Mode description
				38	-0.65	A ₂	Ag translation
				49	-0.05	E	Ag translation
				51	2.95	E	Ag translation
60	A ₁		0.31	64	2.94	A ₁	Ag translation
76	E		0.55	76	1.65	A ₂	Mn translation
107	E		0.17	95	1.12	E	K translation
126	E		0.67	125	1.38	E	K+CN translation
140	A ₁			144	1.28	A ₂	CN translation
168	E	164	0.29	154	1.21	E	CN translation
180	E		0.28				
189	A ₁		0.50	195	0.56	A ₁	CN translation
203	E	197		201	1.37	E	CN translation
				228	0.53	A ₁	CN translation
				233	0.57	E	CN translation
	A ₂	236		234	0.87	A ₂	CN translation
				253	0.44	A ₂	CN translation
265	E		0.12	267	0.24	E	Mn- CN bending
290	E		0.04	293	0.06	E	CN libration
298	A ₁		0.23	298	0.23	A ₂	CN libration
304	E			371	0.01	A ₁	CN libration
332	A ₁		0.21	372	0.01	E	CN libration
357	E		0.19	380	0.23	A ₁	CN libration
377	E	391	0.18	381	0.23	E	CN libration
				427	0.13	E	CN libration
	A ₂	421		430	0.27	A ₂	CN libration
				442	0.37	E	Asym. str. of CN
		452		460	0.38	E	Asymmetric stretching of CN
428	A ₁		0.12	468	0.44	A ₁	Asymmetric stretching of CN
		477		482	0.41	A ₂	Asymmetric stretching of CN
2119	E		0.02	2118	0.05	E	Symmetric stretching of CN
2133	E		0.02	2121	0.05	E	Symmetric stretching of CN
	A ₂	2154		2119	0.05	A ₂	Symmetric stretching of CN
2168	A ₁		0.03	2144	0.05	A ₁	Symmetric stretching of CN

We have obtained all expected 7 A_1 modes and only 13 out of 16 E modes. We are thus able to obtain 20 out of the 23 bands in the Raman spectrum. The three bands that could not be observed may be because they are accidentally degenerate with the observed bands, or their Raman scattering cross section could be low. The IR spectrum from 100-2200 cm^{-1} , in Figure 6.4, shows bands at 164, 197, 236, 391, 421, 452, 477 and 2154 cm^{-1} , several of them being broad features.

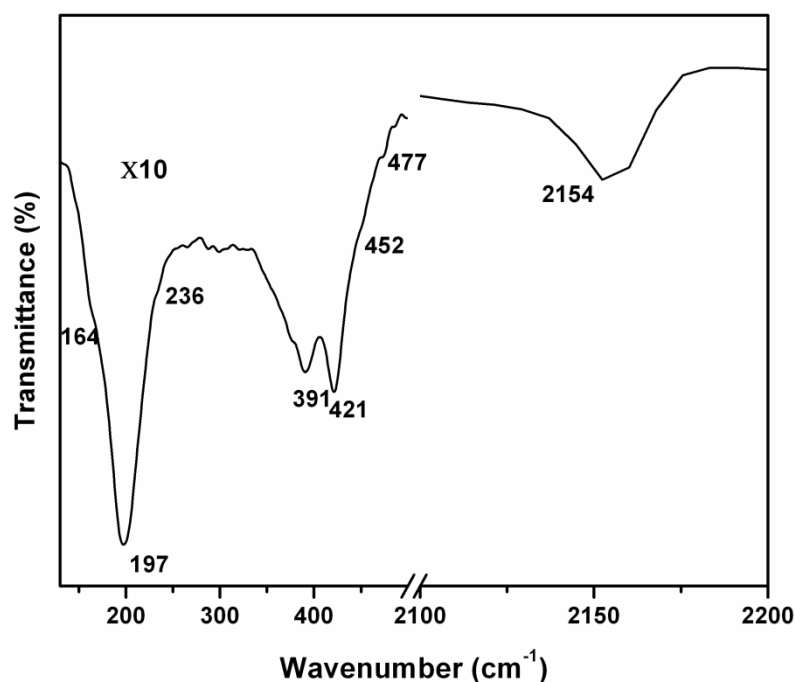


Figure 6.4 IR spectrum of $\text{KMn}[\text{Ag}(\text{CN})_2]_3$ at ambient conditions.

The bands in the range 2100-2170 cm^{-1} arise from the internal vibrations of cyanide ions whereas those below 500 cm^{-1} are due to librations of CN, and translations of Mn and Ag ions.

6.3.2. Pressure and temperature dependent Raman study

Figure 6.5 shows the Raman spectra of $\text{KMn}[\text{Ag}(\text{CN})_2]_3$ from 80 to 533 K in 20 K intervals. Frequencies of all modes are found to decrease monotonically as temperature is increased up to 500 K, pointing absence of phase transition up to this temperature.

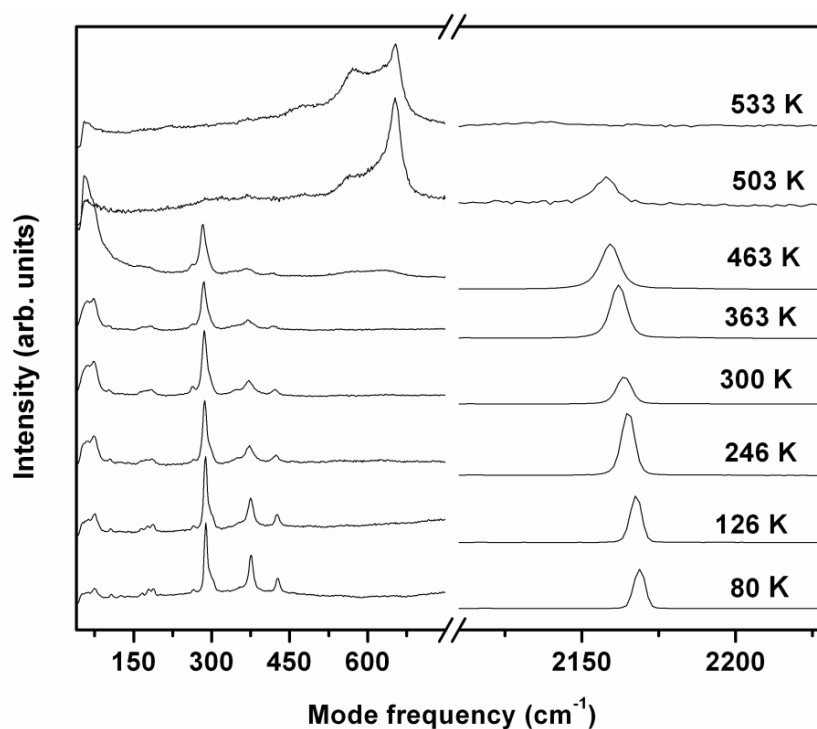


Figure 6.5 Raman spectra of $\text{KMn}[\text{Ag}(\text{CN})_2]_3$ at different temperatures. Distinct change in the spectrum due to the decomposition of the compound is clearly seen at 503 K.

The spectrum changes significantly at 503 K, indicating a possible decomposition, and visual inspection of the sample corroborates this. Mode frequency versus temperature plot, given in Figure 6.6, brings out these features more clearly.

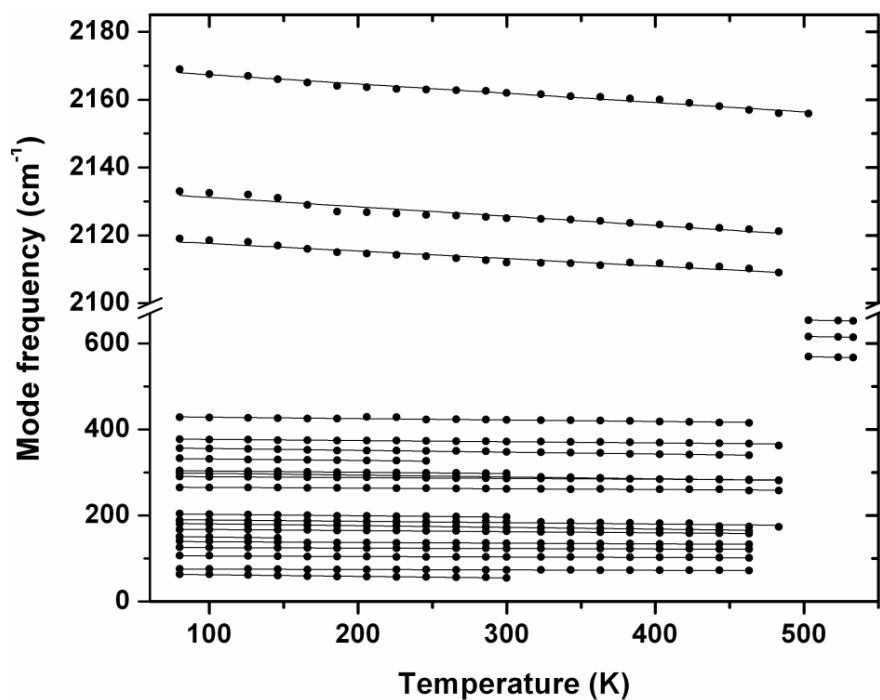


Figure 6.6 Temperature variation of phonon frequencies of $\text{KMn}[\text{Ag}(\text{CN})_2]_3$ showing monotonic decrease of all mode frequencies with increase in temperature.

The spectrum at 533 K exhibits Raman bands characteristic of Mn_5O_8 .⁴⁰ XRD pattern of the decomposed product shows cubic metallic silver as dominant phase similar to that reported in isostructural $\text{Ag}_3[\text{Co}(\text{CN})_6]$.¹⁴

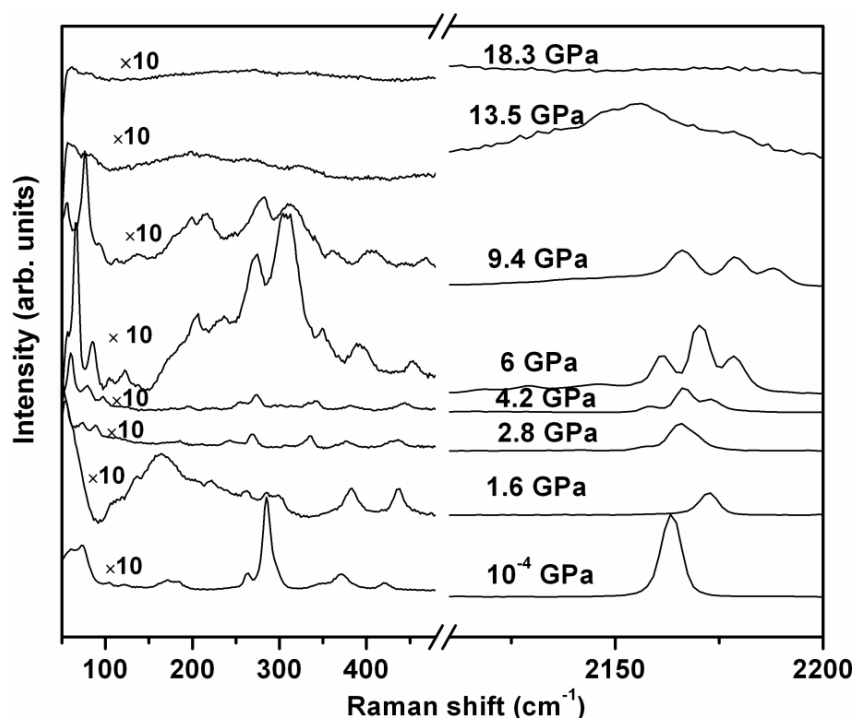


Figure 6.7 Raman spectra of $\text{KMn}[\text{Ag}(\text{CN})_2]_3$ at different pressures under hydrostatic conditions. Dramatic change at 2.8 GPa and amorphization around 13.5 GPa are evident.

Raman spectra of the sample with pressure transmitting medium in increasing pressure cycles are shown in Figure 6.7. Around 2.8 GPa the intensities of high frequency symmetric stretch mode at 2164 cm^{-1} and some low energy modes around 260 cm^{-1} fall rapidly. The bands near 160 cm^{-1} merge into a broad feature and several distinct new low energy bands appear around $53, 74, 88\text{ cm}^{-1}$. At 6 GPa, new Raman bands appear around 2117 cm^{-1} but there is no further change in the low frequency region. The intensities of low energy bands gradually decrease and disappears around 13 GPa indicating possible pressure induced amorphization. Mode frequency versus pressure plot in Figure 6.8 clearly shows the phase transition at 2.8 GPa and amorphization around 13.5 GPa.

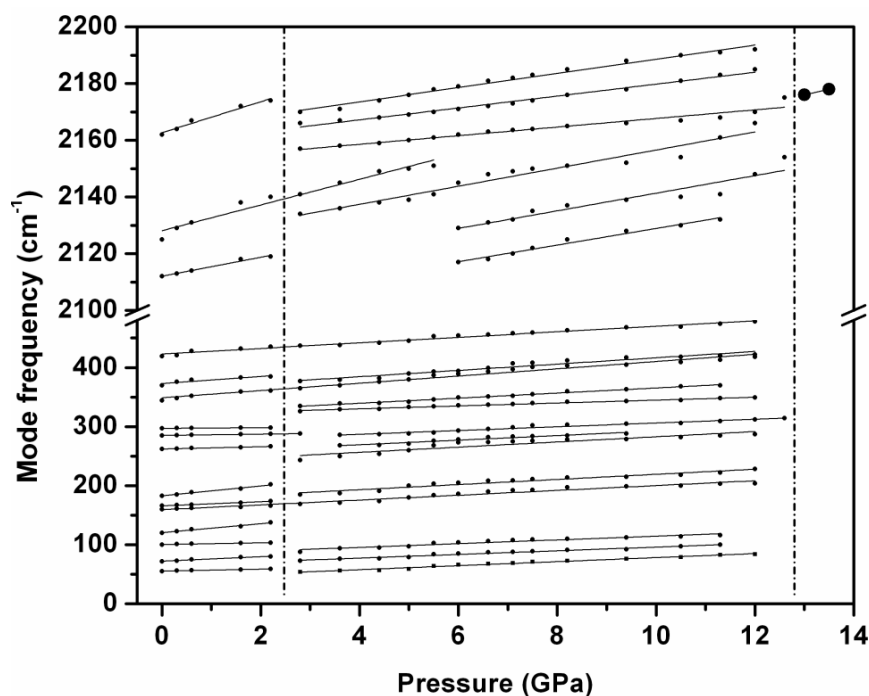


Figure 6.8 Pressure variation of phonon frequencies of $\text{KMn}[\text{Ag}(\text{CN})_2]_3$ under hydrostatic conditions. All modes, except the CN stretch band, disappear above 13 GPa.

The compound remains amorphous even in the pressure reducing cycle, unlike in the isostructural $\text{Ag}_3[\text{Co}(\text{CN})_6]$ that shows Raman bands corresponding to amorphous carbon nitride and crystalline Co_3O_4 in pressure reducing cycles.¹⁸ The spectra with and without medium is found to be similar except for a slight increase in the onset of pressure induced amorphization indicating no chemical reaction between $\text{KMn}[\text{Ag}(\text{CN})_2]_3$ and MeOH/EtOH in contrary to $\text{Zn}(\text{CN})_2$.⁴¹ Pressure dependence of Raman bands below 2.8 GPa were used to obtain their corresponding mode Gruneisen parameters. Table 6.1 lists the mode frequencies (ω_i) and the corresponding Gruneisen parameters (γ_i) obtained from the equation $\gamma_i = \left(\frac{B_0}{\omega_i}\right) \left(\frac{d\omega_i}{dP}\right)$ Here P is the pressure. B_0 is the bulk modulus obtained from high pressure XRD lattice parameters provided by Cairns *et al.*²¹ We find that all the γ_i of the Raman modes are positive,

which is in accordance with the increasing mode frequencies with increasing pressure. Hence, no experimentally observed modes contribute negatively to average thermal expansion. Table 6.2 shows the analysis of implicit and explicit contribution¹⁹ for all Raman modes.

Table 6.2 Total anharmonicities, quasiharmonic (implicit) and true anharmonic (explicit) contribution of different phonons of $\text{KMn}[\text{Ag}(\text{CN})_2]_3$. The numbers in the parentheses are standard errors in the least significant digit.

Mode frequency (cm^{-1})	Total anharmonic (10^{-5}) K^{-1}	Quasiharmonic $\alpha\gamma_i$ (10^{-5}) K^{-1}	True anharmonic (10^{-5}) K^{-1}
60	-50	0.6(2)	-49.3(8)
76	-9.9(9)	1.1	-8.8(9)
107	-10	0.3(4)	-9.6(6)
126	-7	1.3(4)	-5.6(6)
168	-21.7	0.5(8)	-14.1(2)
180	-22.7	0.5(6)	-22.1(4)
189	-17.9	1.0	-16.9
265	-6	0.2(4)	-5.7(6)
290	-7	0.0(8)	-6.9(2)
298	-14.7	0.4(6)	-14.2(4)
332	-24.5	0.4(2)	-9.3(8)
357	-12.2	0.3(8)	-11.8(2)
377	-7.4(6)	0.3(6)	-7.1(4)
428	-7.5(9)	0.2(4)	-7.3(5)
2119	-1.0(2)	0.04	-0.9(8)
2133	-1.1	0.04	-1.0(6)
2168	-1.3	0.06	-1.2(4)

It reveals that all modes involve large changes in vibrational amplitude (true anharmonic or explicit) and negligible change in lattice volume (quasi-harmonic or implicit) and hence it shows overall large thermal expansion behavior.

6.3.3. Results of computational studies

Equilibrium geometry of $\text{KMn}[\text{Ag}(\text{CN})_2]_3$ obtained with conventional DFT calculation gives unit cell volume in agreement with measurement (within 4%), whereas the ratio c/a , deviates by about 13%. Similar discrepancy has been observed in the DFT computed ground state structure of $\text{Ag}_3[\text{Co}(\text{CN})_6]$ and has been attributed to nonlocal electron correlation effects due to $\text{Ag}\dots\text{Ag}$ dispersion interactions.⁴² Moreover, phonon dispersion of $\text{KMn}[\text{Ag}(\text{CN})_2]_3$ computed with the above DFT equilibrium geometry is found to exhibit significant discrepancy compared to Raman spectroscopy results. Therefore, we recomputed the ground state structure of $\text{KMn}[\text{Ag}(\text{CN})_2]_3$ using VASP implementation⁴³ of the vDW-DF2 nonlocal correlation functional⁴⁴ with rPW86 exchange functionals.⁴⁵ Table 6.3 lists the computed lattice parameters along with experimental values.

Table 6.3 Comparison of computed lattice parameters, unit cell volume and bulk modulus of $\text{KMn}[\text{Ag}(\text{CN})_2]_3$ with experimental values. Bulk modulus (B) and its pressure derivative (B') were obtained by fitting volume-energy data to the universal equation of state⁴⁷.

Property	LDA	vDW+DF2+rPW86	Expt (300K)
a (Å)	7.150	6.887	6.922
c (Å)	7.3216	7.7685	8.1465
c/a	1.024	1.128	1.177
V (Å ³)	324.28	319.00	338.03
B (GPa)	17.09	12.24	12.86
B' (GPa)	3.26	6.84	5.01

Experimental bulk modulus was obtained using high pressure XRD lattice parameters of Cairns *et al*²¹ in PASCAL.

It is evident that the vDW-DF2 dispersion interaction correction predicts c/a ratio and unit cell volume in agreement with experiments within 4% and 5% respectively. We have also considered other options for exchange functional, such as revPBE, optPBE or optB86b. They are not found to improve the predicted lattice constants. Furthermore, we also considered LDA+U approach in view of the elements Mn and Ag comprising the substance⁴⁶ and we find that while it helps obtain lattice constants matching with experimental values, subsequent DFPT calculations produce phonon dispersion which significantly disagrees with Raman spectroscopy.

Therefore, we carried out all our calculations using the vDW-DF2 and rPW86 functional. To compute the mode Gruneisen parameters of $\text{KMn}[\text{Ag}(\text{CN})_2]_3$, the phonon spectrum was calculated at three different volumes corresponding to pressures 0.0, 1.0 and 2.0 GPa. Phonon dispersion computed by the interpolation of zone-center modes shows that one of the acoustic bands becomes imaginary over some segments of Brillouin zone. This could be due to unconverged long range interatomic forces. Calculations using supercells was not found to improve the acoustic band appreciably or becomes computationally more demanding, particularly with vDF-DF2 functionals. Therefore we proceeded with zone-center phonon as they are known to represent the thermal expansion coefficients fairly well^{48-50, 13}. The computed phonon frequencies and their mode assignments are compared with the corresponding Raman and IR spectroscopy results in Table 6.1. For most of the Raman modes, we find close matching of frequencies and symmetry labels between experiment and DFPT-Phonopy⁵¹ results. Computed IR modes are found to match with the experimental IR

bands. Table 6.1 also shows the calculated mode Gruneisen parameters. For the low energy A_2 and E optic modes, calculation gives negative Gruneisen parameter. For modes with frequencies above 100 cm^{-1} , we find good matching of computed and measured values. The discrepancy at low frequencies is likely due to the fact that the computed values are for $T = 0\text{ K}$ while the measured values correspond to finite temperatures. The difference between the computed and the measured lattice parameters could also contribute to this variation. Moreover, it is likely that the low frequency modes are more anharmonic which our current quasi-harmonic approximation could not capture accurately.

Figure 6.9 shows our computed linear compressibility of $\text{KMn}[\text{Ag}(\text{CN})_2]_3$ obtained using eq (6.1) with PASCAL principal axis strain calculator.

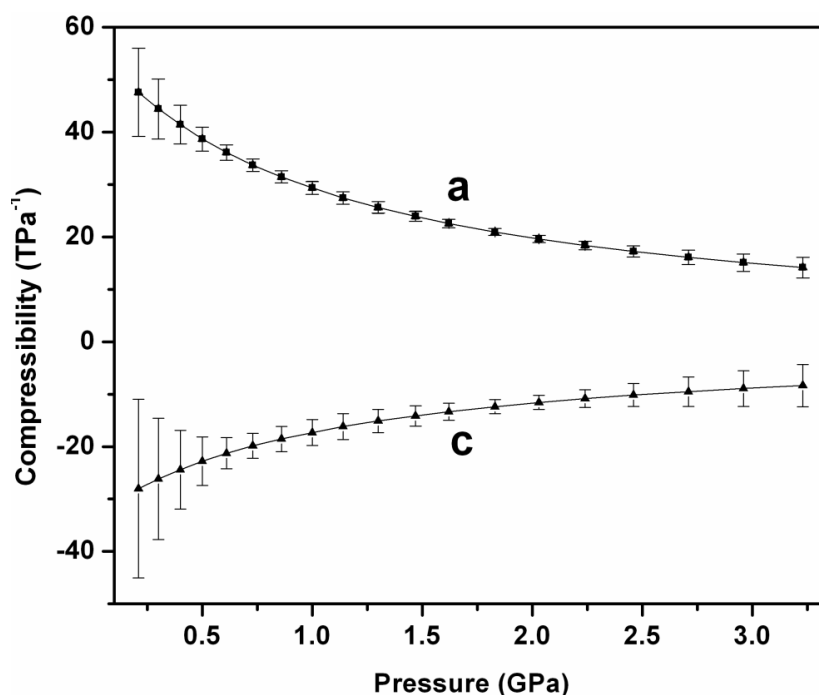


Figure 6.9. Linear compressibilities of $\text{KMn}[\text{Ag}(\text{CN})_2]_3$ calculated by fitting lattice parameters and their corresponding pressures using PASCAL. Pressures are obtained from equation of state calculation.

PASCAL requires data of lattice constants as a function of pressure. We first computed total energy of $\text{KMn}[\text{Ag}(\text{CN})_2]_3$ at 19 volumes ranging from 100% to 90% of the computed equilibrium volume, allowing relaxation of unit cell shape and ionic positions at each volume. Volume-energy data collected from these calculations is then used to compute the pressure-volume equation of state⁴⁷ (calculated bulk modulus and its pressure derivative are listed in Table 6.3). The computed lattice constants at different volumes and the respective pressures from the equation of state are then used in PASCAL calculation of linear compressibility. We find good agreement between our computed and the reported linear compressibility obtained from neutron diffraction.²¹

Table 6.4 lists the elastic constants of $\text{KMn}[\text{Ag}(\text{CN})_2]_3$ together with the linear compressibilities obtained from PASCAL using eq. (6.1) and elastic constants using eqs. (6.2) and (6.3). Experimental linear compressibilities from literature are also shown for comparison. PASCAL computed linear compressibilities shown in Table (6.4) are mean values from Figure 6.9. We find that our linear compressibilities, both from elastic constants and PASCAL fitting, show reasonable agreement with experimental values.²¹

Table 6.4 DFT computed elastic constants, bulk modulus and mean linear compressibilities of $\text{KMn}[\text{Ag}(\text{CN})_2]_3$. Linear compressibilities are obtained from zero pressure elastic constants.

Elastic constants (GPa) at different pressures			
Elastic constants	P_0 (0.0 GPa)	P_1 (1.0 GPa)	P_2 (2.0 GPa)
C_{11}	34.52	37.31	40.06
C_{33}	134.77	153.72	171.24
C_{44}	30.05	29.24	28.22
C_{12}	19.62	22.68	25.97
C_{13}	50.93	54.36	57.49
C_{14}	-12.32	-11.19	-10.17
Bulk modulus (GPa)			
B_{iso}	B_a	B_c	B_{PASCAL}
17.57	25.15	-44.18	10.48
Compressibility (TPa^{-1})			
Method	χ_a	χ_c	
Elastic constants	39.7	-22.6	
PASCAL	23.9	-14.3	
Expt.	33.2	-12.0	

Comparison of magnitudes of the linear compressibilities show that NLC (-14.1 TPa^{-1}) obtained from PASCAL matches with the experimental value (-12.0 TPa^{-1}) while the PLC ($+24.0 \text{ TPa}^{-1}$) is somewhat lower than the experimental value ($+33.2 \text{ TPa}^{-1}$). On the other hand, the bulk modulus obtained from equation of state (12.24 GPa) and

PASCAl fitting (10.48 GPa) are in good agreement with the experimental value (12.86 GPa). The PV equation of state and the PASCAl calculations are done with reference to DFT equilibrium geometry at 0 K. It is known that DFT equilibrium lattice parameters could be different by as much as 3- 4% compared to experimental values. Our calculation thus indicates that the difference in the equilibrium geometry between DFT and experiment influences the linear compressibilities more than the bulk modulus. The bulk modulus and linear compressibilities obtained from elastic constants have enhanced values (Table 6.4) compared to the respective experimental values due to zero pressure limit.

The linear thermal expansion coefficients are calculated using eqs. (6.5) and (6.6). To compute the required directional Gruneisen parameters, we first computed the phonon spectrum of $\text{KMn}[\text{Ag}(\text{CN})_2]_3$ at three different values of the lattice parameter a while the c lattice parameter is held fixed. The three values of a are chosen such that the first value corresponds to the computed equilibrium geometry and the other two values are 1 and 2% smaller than the first. Similar calculations were carried out for three values of c -lattice parameter. With these phonon spectra, the directional Gruneisen parameters are calculated (using eq. (6.7)) to be $\gamma_a = 0.663$ and $\gamma_c = -0.288$. The total specific heat (C_V) of $\text{KMn}[\text{Ag}(\text{CN})_2]_3$ is computed to be $406.3 \text{ J mol}^{-1} \text{ K}^{-1}$. The computed equilibrium molar volume (V_m) is $1.92 \times 10^{-4} \text{ m}^3 \text{ mol}^{-1}$. The appropriate elastic compliances are calculated to be $s_{11} = 0.118 \text{ GPa}^{-1}$, $s_{12} = -0.058 \text{ GPa}^{-1}$, $s_{13} = -0.023 \text{ GPa}^{-1}$ and $s_{33} = 0.025 \text{ GPa}^{-1}$. Using these data, the linear thermal expansion coefficients are computed to be $\alpha_a = 56 \times 10^{-6} \text{ K}^{-1}$ and $\alpha_c = -47 \times 10^{-6} \text{ K}^{-1}$. These thermal expansion coefficients are in good agreement with measured values of $\alpha_a = 61 \times 10^{-6} \text{ K}^{-1}$ and $\alpha_c = -60 \times 10^{-6} \text{ K}^{-1}$.

In $\text{Ag}_3[\text{Co}(\text{CN})_6]$, NTE behavior is partly mediated by local transverse vibrations.⁵² Therefore mode Gruneisen parameters for transverse vibrations of CN are observed to be negative.²⁶ On the other hand in $\text{KMn}[\text{Ag}(\text{CN})_2]_3$ all Gruneisen parameters for the transverse CN vibrations (CN librations) are positive (Table 6.1). This could be due to the hindrance of these vibrations by K^+ cations.⁵² Thus the overall negative contribution to the thermal expansion coefficient is reduced in $\text{KMn}[\text{Ag}(\text{CN})_2]_3$ compared to $\text{Ag}_3[\text{Co}(\text{CN})_6]$.

6.3.4. Mechanism of linear compressibility, thermal expansion and high pressure phase transformation.

We have modeled the linear compressibility by computing the equilibrium lattice parameters at different volumes, allowing the shape of the unit cell and the ionic positions to relax to their equilibrium state. With increasing pressure, we find that the structure of $\text{KMn}[\text{Ag}(\text{CN})_2]_3$ expands along its trigonal axis and shrinks along the basal plane as the overall volume decreases.

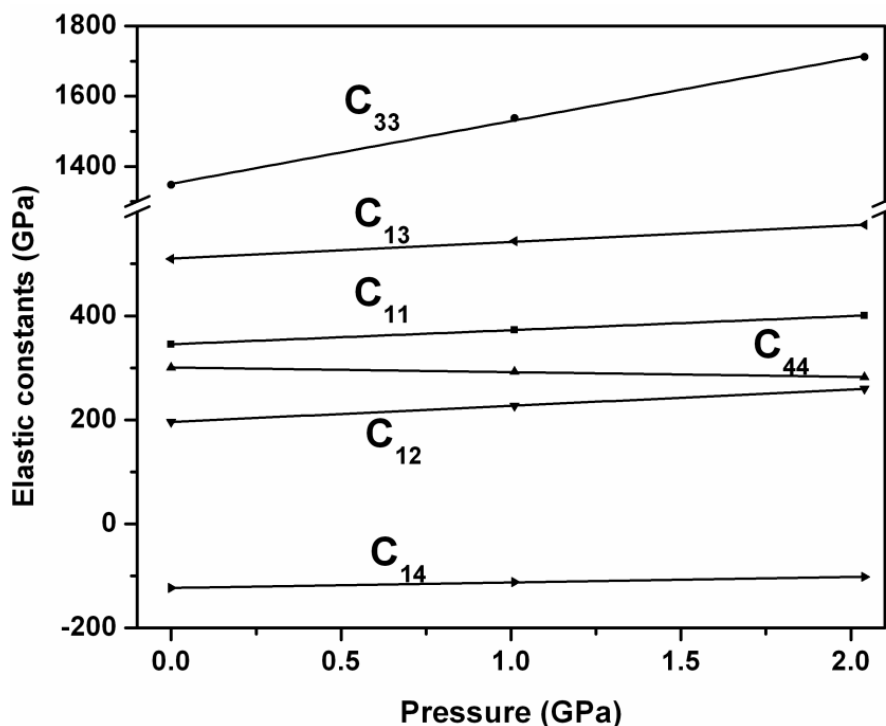


Figure 6.10 Computed pressure dependent elastic constants of $\text{KMn}[\text{Ag}(\text{CN})_2]_3$. C_{44} shows negative pressure derivatives indicating pressure induced structural instability.

Pressure dependence of elastic constants of $\text{KMn}[\text{Ag}(\text{CN})_2]_3$ is shown in Figure 6.10. It is evident that all the elastic constants increase with pressure except C_{44} which decrease with increasing pressure. Negative pressure derivative of the shear elastic constant C_{44} indicates instability of the lattice, via Born stability criterion.⁵³ Moreover, elastic constant for $\text{KMn}[\text{Ag}(\text{CN})_2]_3$ meets the criterion for negative linear compressibility.⁵⁴ NLC, NTE and pressure induced phase transformations are associated with structural instability determined by negative pressure derivative of elastic constant.^{54,57} Several flexible solids are also known to show pressure induced softening of elastic constants.^{58,59} Moreover, elastic constants of $\text{KMn}[\text{Ag}(\text{CN})_2]_3$ does not meet any of the condition of isotropy for trigonal crystals.²⁷ This shows that NLC of $\text{KMn}[\text{Ag}(\text{CN})_2]_3$ is driven by lattice instability and anisotropy of the crystal.

Next we consider the thermal expansion of $\text{KMn}[\text{Ag}(\text{CN})_2]_3$. In view of Munns⁶⁰ analysis of role of the elastic constants in NTE, it is evident that our computed PTE and NTE coefficients are determined by significantly anisotropic Gruneisen functions ($\gamma_a = 0.663$ and $\gamma_c = -0.288$) and negative elastic compliance s_{13} . Moreover, calculated elastic constants shows that $\text{KMn}[\text{Ag}(\text{CN})_2]_3$ is highly anisotropic.²⁷ These things show that NTE and PTE of $\text{KMn}[\text{Ag}(\text{CN})_2]_3$ is due to the combined Gruneisen and elastic anisotropy of the crystal.⁶⁰

To gain insight into the origin of anharmonic lattice vibrations and hence linear compressibility and thermal expansion of $\text{KMn}[\text{Ag}(\text{CN})_2]_3$, we computed the pressure variation of the mean partial phonon frequencies of the various atoms, defined by the equation:^{14,61}

$$\omega_i = \left(\frac{1}{3N_q N_i} \right) \sum_{q,j} \omega(j,q) e(j,q,i) \quad (6.8)$$

where N_q is the number of q -points, N_i , the number of atoms of type i in the unit cell, $\omega(j,q)$ the angular frequency of phonon mode j at wavevector q , and $e(j,q,i)$ the magnitude of the component of the eigen vector corresponding to atom type i . The eigen values and eigen vectors are computed on a $9 \times 9 \times 9$ grid of k -points using Phonopy with VASP computed zone-center eigen values and eigen vectors. The results are shown in Figure 6.11. We also depict the partial frequencies of $\text{Ag}_3[\text{Co}(\text{CN})_6]$ in Figure 6.11 for comparison. The partial frequencies were calculated from all modes of the given species. We see that the partial frequencies of all atoms increase with increasing pressure. However, the rate of increase is lowest for Ag, both in $\text{KMn}[\text{Ag}(\text{CN})_2]_3$ and $\text{Ag}_3[\text{Co}(\text{CN})_6]$. This indicates that large amplitude displacements of Ag atoms can occur with minimum enthalpy cost.

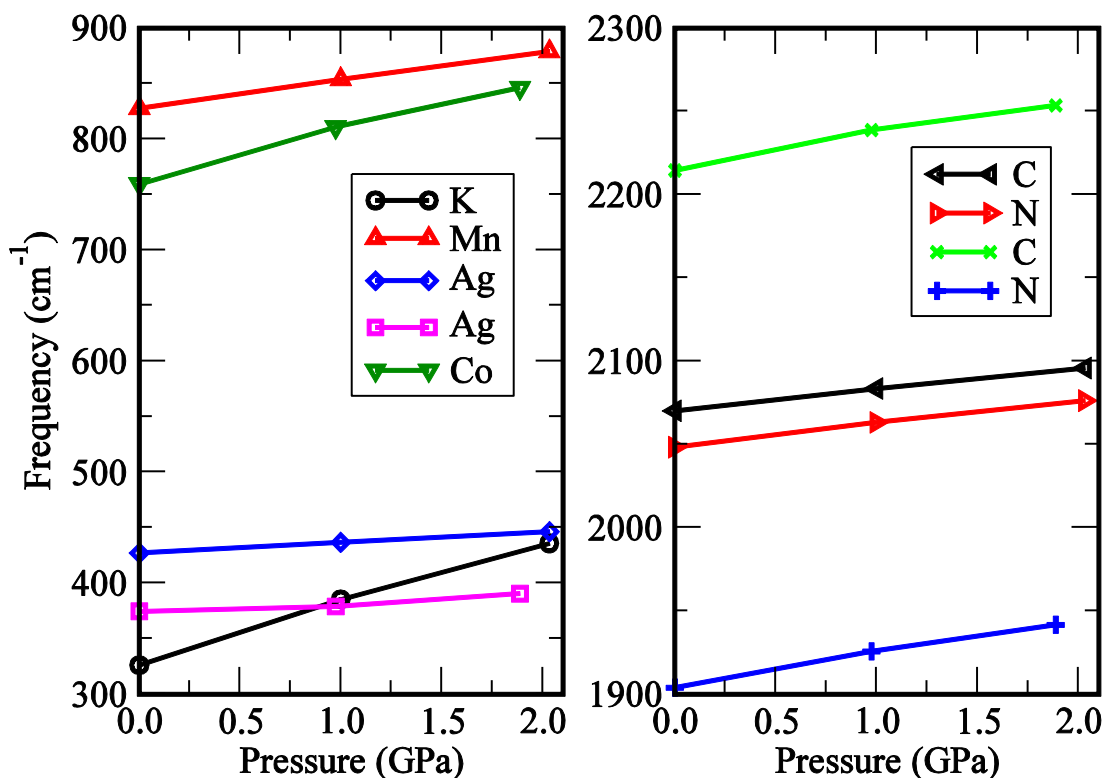


Figure 6.11 Pressure variation of mean partial phonon frequencies of the various atoms in $\text{KMn}[\text{Ag}(\text{CN})_2]_3$ and $\text{Ag}_3[\text{Co}(\text{CN})_6]$. K, Mn, Ag, C and N partial frequencies from $\text{KMn}[\text{Ag}(\text{CN})_2]_3$ are shown by $\circ, \Delta, \diamond, \triangleleft, \triangleright$ respectively. Partial frequencies of Co, Ag, C and N from $\text{Ag}_3[\text{Co}(\text{CN})_6]$ are shown by symbols $\nabla, \square, \times, +$ respectively. Ag frequencies shows lower slope relative to other atoms. Between $\text{Ag}_3[\text{Co}(\text{CN})_6]$ and $\text{KMn}[\text{Ag}(\text{CN})_2]_3$, slope of Ag frequency in the latter is increased. Average partial frequency of $\text{KMn}[\text{Ag}(\text{CN})_2]_3$ is higher than that of $\text{Ag}_3[\text{Co}(\text{CN})_6]$ (C and N frequencies are averaged).

Figure 6.11 shows that the partial frequencies of $\text{KMn}[\text{Ag}(\text{CN})_2]_3$ are higher than those of $\text{Ag}_3[\text{Co}(\text{CN})_6]$, which indicates lattice stiffening in the former. Moreover, partial frequency of K, which is significantly lower than that of Ag at zero pressure, increases rapidly and becomes comparable to that of Ag with increasing pressure. This indicates that inclusion of K stiffen the lattice and changes the dynamics of $\text{KMn}[\text{Ag}(\text{CN})_2]_3$ as inferred in Cairns *et al.*²¹ Consequently, NTE/PTE and NLC/PLC of $\text{KMn}[\text{Ag}(\text{CN})_2]_3$ are lower than the respective values of $\text{Ag}_3[\text{Co}(\text{CN})_6]$. Our calculation further shows that the lattice stiffening combined

with modified dynamics due to K inclusion causes the phase transition of $\text{KMn}[\text{Ag}(\text{CN})_2]_3$ to occur above 2 GPa rather than at 0.2 GPa as in $\text{Ag}_3[\text{Co}(\text{CN})_6]$.

In order to understand the pressure induced phase transformation, we analyzed the atomic displacements of all phonon modes of $\text{KMn}[\text{Ag}(\text{CN})_2]_3$. Figure 6.12 shows the atomic displacements of the A_2 mode at 38 cm^{-1} and the E mode at 49 cm^{-1} .

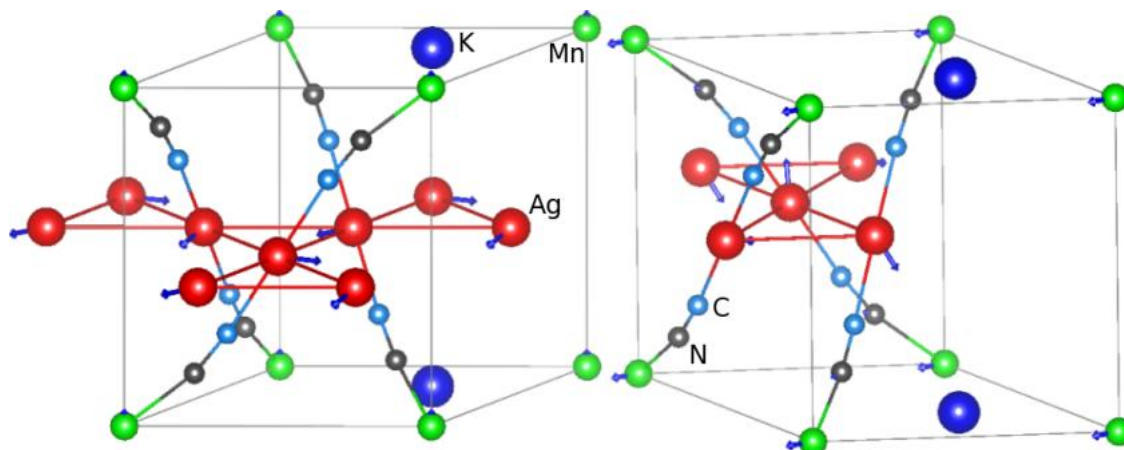


Figure 6.12 Computed atomic displacements of the low frequency optic modes, (a) the A_2 mode at 38 cm^{-1} , (b) the E mode at 49 cm^{-1} .

These two low energy optic modes, which show prominent displacement of Ag atoms, are predicted to have negative Gruneisen parameters. Moreover, negative derivative of C_{44} is associated with softening of transverse acoustic modes.⁶² Thus, pressure induced phase transformation is caused by transverse acoustic modes and coupled atomic displacement of two soft optic modes.

6.4. Summary and conclusion

Linear compressibility and thermal expansion of $\text{KMn}[\text{Ag}(\text{CN})_2]_3$ are investigated using pressure and temperature dependent Raman spectroscopy and DFT calculations. Computed linear compressibilities obtained from pressure dependent lattice parameters and from elastic constants corroborate the reported neutron

diffraction results. Elastic constants of $\text{KMn}[\text{Ag}(\text{CN})_2]_3$ shows that the crystal is highly anisotropic, and fulfills the criterion for NLC. Negative pressure derivative of C_{44} further indicates instability of the lattice. Pressure variation of mean partial phonon frequencies of $\text{KMn}[\text{Ag}(\text{CN})_2]_3$ shows that large amplitude anharmonic displacements of Ag atoms can occur with minimum enthalpy cost. NTE/ NLC, PTE/ PLC and pressure induced transformation (dynamic instability) in $\text{KMn}[\text{Ag}(\text{CN})_2]_3$ are associated with elastic anomalies and Gruneisen anisotropies. Comparison of mean partial phonon frequencies between $\text{KMn}[\text{Ag}(\text{CN})_2]_3$ and $\text{Ag}_3[\text{Co}(\text{CN})_6]$ shows that Mn and Ag atoms from the former have higher frequencies than Co and Ag from the latter. Average CN partial frequencies are almost same between the two. K partial frequency is lower than that of Ag at zero pressure and increases rapidly with pressure becoming comparable to that of Ag around 2 GPa. This shows that K inclusion stiffens the lattice and changes the dynamics, causing the pressure induced phase transformation of $\text{KMn}[\text{Ag}(\text{CN})_2]_3$ to occur at a higher pressure than found in $\text{Ag}_3[\text{Co}(\text{CN})_6]$. The pressure induced phase transformation of $\text{KMn}[\text{Ag}(\text{CN})_2]_3$ observed in our measurements, is due to softening of transverse acoustic mode, which is evident from the negative pressure derivative of C_{44} shear elastic constant, and the A_2 and E low energy soft optic modes.

6.5. References

- ¹D. McCann, L. Cartz, R. E. Schmunk and Y. D. Harker *J. Appl. Phys.*, **43**, 1432, (1972).
- ²R. Grosse, P. Krause, M. Meissner and A. Tausend *J. Phys. C* **11**, 45 (1978).
- ³J. W. E Mariathasan, L. W. Finger and R. M. Hazen, *Acta. Crystallogr. B* **41**, 179 (1985).
- ⁴S. Praver, T. F. Smith and T. R. Finlayson, *Aust. J. Phys.* **38**, 63 (1985).
- ⁵R. H. Baughman, S. Stafstrom, C. Cui and S. O. Dantas, *Science*, **279**, 1522 (1998).
- ⁶I. Loa, K. Syassen, R. K. Kremer, U. Schwarz and M. Hanfland *Phys. Rev. B*, **60**, R6945- R6948 (1999).
- ⁷T. R. Ravindran and A. K. Arora, T. A. Mary, *Phys. Rev. Lett.* **84**, 3879 (2000).
- ⁸T. R. Ravindran and A. K. Arora, *Phys. Rev. B* **67**, 064301 (2003).
- ⁹K. W. Chapman, P. J. Chupas and C. J. Kepert, *J. Am. Chem. Soc.* **127**, 15630 (2005).
- ¹⁰K. W. Chapman, P. J. Chupas and C. J. Kepert, *J. Am. Chem. Soc.* **128**, 7009 (2006).
- ¹¹T. R. Ravindran, A. K. Arora, Sharat Chandra, M. C. Valsakumar and N. V. Chandrashekar, *Phys. Rev. B*, **76**, 054302 (2007).
- ¹²T. R. Ravindran, A. K. Arora and T. N. Sairam, *J. Raman Spectrosc.* **38**, 283 (2007).
- ¹³P. Ding, E. J. Liang, Y. Jia, Z. Y. Du. *J. Phys.: Condens. Matter* **20**, 275224 (2008).
- ¹⁴A. L. Goodwin. et al, *Science* **319**, 794 (2008).
- ¹⁵A. L. Goodwin, D. A. Keen and M. G. Tucker, *Proc. Natl. Acad. Sci.* **105**, 18708 (2008).
- ¹⁶A. L. Goodwin, *Z. Kristallogr. Suppl.* **30**, 1 (2009).

- ¹⁷ D. A. Keen, M. T. Dove, J. S. O. Evans, A. L. Goodwin, L. Peters and M. G. Tucker, *J. Phys.:Condens. Matter* **22**, 404202 (2010).
- ¹⁸ R. Rao, S. N. Achary, A. K. Tyagi and T. Sakuntala, *Phys. Rev. B* **84**, 054107 (2011).
- ¹⁹ K. Kamali, T. R. Ravindran, C. Ravi, Y. A. Sorb, N. Subramanian and A. K. Arora, *Phys. Rev. B* **86**, 144301 (2012).
- ²⁰ R. Mittal, M. Zbiri, H. Schober, S. N. Achary, A. K. Tyagi and S. L. Chaplot, *J. Phys.: Condens. Matter* **24**, 505404 (2012).
- ²¹ A. B. Cairns, A. L. Thompson, M. G. Tucker, J. Haines and A. L. Goodwin, *J. Am. Chem. Soc.* **134**, 4454 (2012).
- ²² W. Li, et al, *J. Am. Chem. Soc.* **134**, 11940 (2012).
- ²³ A. B. Cairns, J. Catafesta, C. Levelut, J. Rouquette, A. Lee, L. Peters, A. L. Thompson, V. Dmitriev, J. Haines and A. L. Goodwin, *Nature Materials* **12**, 212 (2013).
- ²⁴ U. Geisers and J. A. Schlueter, *Acta. Cryst. C* **59**, i21 (2003).
- ²⁵ M. J. Cliffe and A. L. Goodwin, *J. Appl. Cryst.* **45**, 1321 (2012).
- ²⁶ P. Hermet, J. Catafesta, J. -L. Bantagnies, C. Levelut, D. Maurin, A. B. Cairns, A. L. Goodwin and J. Haines, *J. Phys. Chem. C.* **117**, 12848 (2013).
- ²⁷ G. Grimvall, *Thermophysical properties of materials*; Elsevier science, Amsterdam, Netherlands, 1999.
- ²⁸ G. Kresse and J. Hafner, *Phys Rev. B* **47**, 558 (1993).
- ²⁹ G. Kresse and J. Hafner, *Phys. Rev. B* **49**, 14251 (1991).
- ³⁰ G. Kresse and J. Furthmuller *Phys. Rev. B* **54**, 11169 (1996).
- ³¹ P. E. Blochl, *Phys. Rev. B* **50**, 17953 (1994).
- ³² G. Kresse and J. Joubert, *Phys. Rev. B* **59**, 1758 (1999).
- ³³ H. J. Monkhorst and J. D. Pack, *Phys. Rev. B* **13**, 5188 (1976).

- ³⁴ X. Gonze and C. Lee, *Phys. Rev. B* **55**, 10355 (1997).
- ³⁵ S. Baroni, S. Gironcoli and A. Corso, *Rev. Mod. Phys.* **73**, 515 (2001).
- ³⁶ X. Wu, D. Vanderbilt and D. R. Hamann, *Phys. Rev. B* **72**, 035105 (2005).
- ³⁷ D. Karhanek, T. Bucko and J. A. Hafner, *J. Phys.: Condens. Matter* **22**, 265006 (2010).
- ³⁸ Y. L. Page and P. Saxe, *Phys. Rev. B* **65**, 104104 (2002).
- ³⁹ W. G. Fateley and F. R. Dollish, *Infrared and Raman Selection Rules for Molecular and Lattice Vibrations*, Wiley-Interscience, New York, 1972.
- ⁴⁰ C. B. Azzoni et al, *Solid State Commun.* **112**, 375 (1999).
- ⁴¹ I. E. Collings, et al, *J. Am. Chem. Soc.* **135**, 7610 (2013).
- ⁴² M. Calleja, A. L. Goodwin and M. T. Dove, *J. Phys.: Condens. Matter*, **20**, 255226 (2008).
- ⁴³ J. Klimeš, D. R. Bowler and A. Michaelides, *Phys. Rev. B*, **83**, 195131 (2011).
- ⁴⁴ K. Lee, E. D. Murray, L. Kong, B. Lundqvist and D. C. Langreth, *Phys. Rev. B*, **82**, 081101 (2010).
- ⁴⁵ E. D. Murray, K. Lee and D. C. Langreth, *J. Chem. Theory Comput.* **5**, 2754 (2009).
- ⁴⁶ A. Jain, G. Hautier, C. J. Moore, S. J. Ong, C. C. Fischer, T. Mueller and K. A. Persson *Comput. Mater. Sci.* **50**, 2295 (2011).
- ⁴⁷ Vinet et al, *J. Phys.: Condens. Matter*, **1**, 1941 (1981).
- ⁴⁸ A. M. Hofmeister and H -k Mao, *Proc. Natl. Acad. Sci.* **99**, 559 (2002).
- ⁴⁹ O. C. Pluchery, D. Sauer and J. Kreisel, *J. Phys. Condens. Matter*, **22**, 165901 (2010).
- ⁵⁰ V. Gava, A. L. Martinotto and C. A. Perottoni, *Phys. Rev. Lett.* **109**, 195503 (2012).
- ⁵¹ A. Togo, F. Oba and I. Tanaka, *Phys. Rev. B* **78**, 134106 (2008).
- ⁵² J. L. Korcok, M. J. Katz and D. B. Leznoff, *J. Am. Chem. Soc.* **131**, 4866 (2009).

- ⁵³E. Gregoryanz, R. J. Hemley, H.-k Mao and P. Gillet, *Phys. Rev. Lett.* **84**, 3117 (2000).
- ⁵⁴A. Marmier, P. S. Ntoahae, P. E. Ngoepe, D. G. Pettifor and S. C. Parker, *Phys. Rev. B* **81**, 172102 (2010).
- ⁵⁵H. Kimizuka and S. Ogata and J. Li, *J. Appl. Phys.* **103**, 053506 (2008).
- ⁵⁶N. Choudhury and S. L. Chaplot, *Phys. Rev. B* **73**, 094304 (2006).
- ⁵⁷F. Decrens, J. Zhang, B. Li and R. C. Liebermann, *Phys. Rev. B* **63**, 224105 (2001).
- ⁵⁸C. Pantea et al, *Phys. Rev. B* **73**, 214118 (2006).
- ⁵⁹A. U. Ortiz, A. Boutin, A. H. Fuchs and F. -X. Coudert, *Phys. Rev. Lett.* **109**, 195502 (2012).
- ⁶⁰R. W. Munn, *J. Phys. C* **5**, 535 (1972).
- ⁶¹Goodwin, A. L. private communication.
- ⁶²M. Maczka, J. M. Hanuz and S. Kojima, *Phys. Rev. B* **77**, 104116 (2008).

Chapter 7

Summary and Conclusions

7.1 SUMMARY

Low thermal expansion compounds with open framework are remarkable from a fundamental research point of view and they are also important for applications. Based on thermal expansion coefficients, these materials can be classified into two major categories: (a) Low thermal expansion (low positive, zero and negative expansion coefficient) compounds like ReO_3 family, ZrW_2O_8 , NASICON family, TaO_2F , $\text{Ca}_{0.5}\text{Sr}_{0.5}\text{P}_6\text{O}_{24}$ etc. (b) colossal thermal expansion compounds like $\text{Ag}_3[\text{Co}(\text{CN})_6]$, $\text{KMn}[\text{Ag}_3(\text{CN})_6]$ etc. This thesis discusses the results of high pressure Raman spectroscopic studies on: (a) Tunable low thermal expansion of alkali substituted NZP family of materials; (b) zero thermal expansion material TaO_2F (c) colossal anisotropic thermal material $\text{KMn}[\text{Ag}_3(\text{CN})_6]$. In addition, high pressure X-ray diffraction and first principles calculations have been performed on some of these compounds. Pressure is used as a primary thermodynamic parameter to take the system across phase transition(s). Polycrystalline ceramic samples and single crystals (in one case) were used to study behaviour of phonons and phase transitions.

A detailed high pressure Raman spectroscopic and X-ray diffraction study of $\text{NaZr}_2(\text{PO}_4)_3$ ceramic synthesised by sol gel method was carried out to study the structural phase transitions both in increasing and decreasing pressure cycles in the pressure range 0-25 GPa. Additionally high temperature Raman spectroscopic studies from 80-840 K were carried out, and these results, in combination with pressure

measurements were analysed to identify the anharmonic phonons contributing to low thermal expansion. To complement the Raman and XRD studies, DFT calculations at several pressures (or volumes) from ambient to 5 GPa were performed to compute bulk modulus by fitting the computed Energy-Volume data to Vinet equation of state. Thermal expansion coefficient was calculated from Gruneisen parameters of all phonon modes obtained from computations and this compares well with the reported experimental value.

Raman spectroscopic studies of $AZr_2(PO_4)_3$, $A = K, Rb$ and Cs at different pressures (0-25 GPa) and temperatures (80-860 K) were carried out to compare and analyse the contribution of the various phonon modes to anisotropic thermal expansion with increasing size of alkali cations and to investigate the stability of these compounds with pressure. From temperature dependent measurements, contribution of prominent phonon frequency shifts and line widths to lattice anharmonicity were compared for different cation sizes. Bulk modulus was computed by fitting DFT calculated energy-volume data to third order Birch Murnaghan equation.

Polycrystalline TaO_2F synthesised by a wet chemical method at ambient conditions exhibits zero thermal expansion (ZTE) property and anharmonic phonons responsible for such ZTE property were investigated by Raman spectroscopy as functions of pressure and temperature. Interestingly, at ambient conditions, cubic Perovskite structured ($Pm-3m$) TaO_2F exhibits disorder induced first order Raman spectra. The spectra were analysed to obtain more clarity on onset of its structural phase transformation to rhombohedral structure in the intermediate pressure range of 0.7 to 4 GPa and stability at high pressures.

Single crystals of $\text{KMn}[\text{Ag}(\text{CN})_2]_3$ were synthesised by a layering technique. Mode assignments were obtained using polarised Raman spectroscopy on suitably oriented single crystals, and phonon modes at high pressure were also obtained experimentally. Density Functional Theory (DFT) calculations were used to compute anisotropic linear compressibility and thermal expansion properties of $\text{KMn}[\text{Ag}(\text{CN})_2]_3$ via pressure dependence of lattice parameters, elastic constants and phonon spectrum. Large persistent negative linear compressibility of $\text{KMn}[\text{Ag}(\text{CN})_2]_3$ compared to $\text{Ag}_3[\text{Co}(\text{CN})_6]$ and extended phase transition pressure were explained using pressure variation of elastic constants and average partial phonon frequencies.

7.2 Conclusions

The significant new results presented in this thesis are:

1. Negative thermal expansion along the a -axis in sodium zirconium phosphate is found to be due to two low energy phonon modes corresponding to (i) a combination of PO_4 tetrahedral librations and Zr translations and (ii) coupled rotation of ZrO_6 and PO_4 tetrahedra; negative contribution from these modes leads to an overall low positive thermal expansion.¹
2. NZP undergoes two phase transitions around 5 and 6.7 GPa and the Phase III maintains its structural integrity up to 32 GPa. Phase II could be refined to a rhombohedral ($R3$) structure whereas phase III is indexed to an orthorhombic ($Pbcn$) structure. In $\text{NaZr}_2(\text{PO}_4)_3$, two soft E_g modes in the ambient phase are found to be responsible for polyhedral tilt transition at 5 GPa.²
3. Prototypic NZP is found to be stable up to 32 GPa but compounds with larger cations amorphize at lower pressures.³

4. Apart from low frequency translational and librational modes, several other bending modes of phosphate ions are found to be strongly anharmonic in $AZr_2(PO_4)_3$, $A=K, Rb$ and Cs .³
5. Anharmonicity of various Raman modes of $AZr_2(PO_4)_3$, $A=Na, K, Rb, Cs$ are compared and possible explanations for the difference in their thermal expansion coefficient are discussed.³
6. In TaO_2F , a reversible cubic to rhombohedral phase transformation onsets around 0.8 GPa and gets completed at 4.4 GPa with all four predicted normal modes corresponding to a $R-3c$ phase and retaining the structure up to 19 GPa. Phonon anharmonicity of modes are analyzed and related with thermal expansion coefficient.⁴
7. Intensities of Raman bands remain unchanged with increase in temperature, indicating static disorder in TaO_2F .⁴
8. Assignment of Raman modes on single crystals of $KMn[Ag(CN)_2]_3$ were reported for the first time.⁵
9. Inclusion of K in $KMn[Ag(CN)_2]_3$ stiffens the lattice and changes the dynamics, causing pressure induced phase transformation of $KMn[Ag(CN)_2]_3$ to occur at a higher pressure than found in $Ag_3[Co(CN)_6]$.⁵
10. Pressure induced phase transformation of $KMn[Ag(CN)_2]_3$ is driven by negative pressure derivative of C_{44} shear elastic constant that corresponds to the transverse acoustic mode, and the A_2 and E low energy soft optic modes.⁵

7.3 Directions for future studies

- High pressure elastic constants calculation on alkali substituted NZP compounds would be helpful to confirm the phonon modes responsible for phase transition.

- High pressure synchrotron X-ray diffraction on TaO_2F could be repeated carefully by considering intermediate pressure range of 0.8 to 4 GPa that might agree with the result of mixed phase as observed in Raman spectroscopy.
- High pressure X ray or neutron diffraction of $\text{KMn}[\text{Ag}(\text{CN})_2]_3$ could help identify the new phase at 2.8 GPa that was observed in the present Raman experiments.

7.4. References

- ¹*Anharmonic phonons of $\text{NaZr}_2(\text{PO}_4)_3$ studied by Raman spectroscopy, first principles calculations and x-ray diffraction*
K. Kamali, T. R. Ravindran, C. Ravi, Y. Sorb, N. Subramanian and A. K. Arora,
Phys. Rev. B, **86**, 144301 (2012).
- ²*Pressure induced phase transformations in $\text{NaZr}_2(\text{PO}_4)_3$ studied by X-Ray diffraction and Raman spectroscopy*
K. Kamali, T. R. Ravindran, N. V. Chandra Shekar, K. K. Pandey and S. M. Sharma
J. Solid State Chem. **221**, 285 (2015).
- ³*Comparative study of anharmonic effects in $\text{AZr}_2(\text{PO}_4)_3$, A = Na, K, Rb using Raman spectroscopy and first principles calculation*
K. Kamali, T. R. Ravindran and C. Ravi (Under Review)
- ⁴*High pressure Raman spectroscopic study of TaO_2F*
K. Kamali, T. R. Ravindran and T. N. Sairam
Vibrational Spectroscopy, **71**, 12. (2014).
- ⁵*Linear compressibility and thermal expansion of $\text{KMn}[\text{Ag}(\text{CN})_2]_3$ studied by Raman spectroscopy and first-principles calculations*
K. Kamali, C. Ravi, T. R. Ravindran, R. M. Sarguna, T. N. Sairam and G. Kaur,
J. Phys. Chem. C, **117**, 25704. (2013).